SATURABLE ABSORPTION AND TWO-PHOTON ABSORPTION IN GRAPHENE

YANG HONGZHI

(M. Sc. Shandong University, CHINA)

A THESIS SUBMITTED

FOR THE DEGREE OF PHILOSOPHY OF SCIENCE

DEPARTMENT OF PHYSICS

NATIONAL UNIVERSITY OF SINGAPORE

2012

Acknowledgements

I would not have been able to complete this thesis without the support of numerous individuals and institutions. So great is the number in fact that I fear I may fail to recognize all who have contributed to this effort, but in gratitude I attempt to do so here. Professor Ji Wei was my academic advisor and has devoted many time and efforts to educate me patiently with great enthusiasm. Under his professional guidance, I gained a deep understanding in the fields of nonlinear optics.

I am grateful to National University of Singapore (NUS) research scholarship program for its role in helping me complete this dissertation. I appreciate that attitudes hold by NUS and Singapore government that "Never let any talent student loose due to the lack of economic support!"

The services of Femtosecond Laser Spectroscopy Laboratory were essential to the completion of this work. I found that NUS experience unique not only for its academics and research, but also for its ability to attract the very best students in the world. Femtosecond Laser Spectroscopy Laboratory seems to be particularly gifted in this regard. I am thankful especially to those students with whom I most closely worked for their friendship and selfless contribution to my work.

Dr. Feng Xiaobo is a research staff in our lab. Thanks for her support and fruitful discussion in the process of finishing this thesis. Ms. Wang Qian is my colleague and we work cooperatively on the project. Thanks for her constructive discussion and valuable suggestions. Thanks to Dr. Qu Yingli, who is my senior sister, for her

enthusiastic help and constructive suggestions. Dr. Xing Guichuan, who is my senior brother, thanks for his patient guidance in the process of learning the experimental techniques and knowledge. Thanks to Professor Gu Bing for the fruitful discussion and help. Thanks to Professor Xu Qinghua, who is a talented and helpful professor in Chemistry department, for his valuable discussions and suggestions. Thanks to Professor Wee Thye Shen, Andrew, Professor Chen Wei and Dr. Huang Han for their help in the process of synthesize of the samples and fruitful discussions. Thanks to Professor Shen Zexiang and Dr. Wang Yingying for their help in Raman spectroscopy measurements. I also would like to thank other colleagues in the lab, Dr. Venkatram Nalla, Mr. Mohan Singh Dhoni and Mr. Venkatesh Mamidala for their constructive instruction and help in the research and lives. I would also like to thanks Dr. H. I. Elim, Dr. He Jun and Dr. Mi Jun for their fruitful contributes to the femtosecond lab.

At last, I would thank my wife, Ms. Zhao Jiamei for her everlasting love and support. I also would like to thank my family. It is their support that gave me confidence and strength to conquer every difficulty.

Table of Contents

Summary

Graphene, as a two-dimensional carbon material, exhibits unique linear and nonlinear optical absorption properties that have attracted a great deal of research interest. Graphene has been demonstrated to be an excellent saturable absorber due to its ultrafast response time, large modulation depth, and low saturation intensity. The saturation intensity of graphene has been measured in the infrared range. However, there is a large discrepancy in the reports due to the different experimental conditions such as the graphene samples synthesized with different methods and the operating wavelength.

To gain a full understanding of saturable absorption in graphene, we employ both Z-scan and frequency-degenerate transient absorption (or pump-probe) measurements as described in Chapters 3. In chapter 4, we systematically study the saturable absorption of graphene by carrying out Z-scan experiments on the monolayer, bilayer and 6-layer epitaxial graphene at 780 nm with 1 kHz and 400-fs laser pulses. The epitaxial graphene has been demonstrated to be of high quality and uniformity. The saturation intensity of epitaxial graphene at 780 nm is measured to be 6(±2) GW/cm^2. It is found that as the number of layer increased up to 6, the saturable absorption signal increased linearly, which indicates that the nonlinear optical signal can be enhanced by increasing the stacking of graphene layers. Furthermore, the spectral dependence of saturable absorption of graphene is studied by extending from 780 nm to the spectral range of 900 nm to 1100 nm with femtosecond laser pulses on epitaxial

graphene. It is found that as the operating wavelength increases from 900 nm to 1100 nm, the saturation intensity reduces from ~5 GW/cm^2 to 1.5 GW/cm^2. At last, our experimental results are compared with the reports of saturation intensity of graphene synthesized with different methods and the saturable absorption of vertical aligned CNTs thin film.

In chapter 5, we explore the two-photon absorption properties of monolayer and bilayer graphene. Two-photon absorption is another important nonlinear optical absorption property of graphene. It has been demonstrated that ballistic electric currents can be injected and controlled in epitaxial graphene via quantum interference between photocurrents generated by one-photon and two-photon interband transitions. In order to explore the two-photon absorption properties of the monolayer and bilayer epitaxial graphene, we carry out pump-probe and Z-scan experiments on the monolayer and bilayer epitaxial graphene with femtosecond laser pulses at 780 nm and 1100 nm. The two-photon absorption of bilayer graphene is measured to be 10 cm/MW at 780 nm and 20 cm/MW at 1100 nm. Subsequently, the two-photon absorption coefficient of graphene is theoretically studied using the second-order quantum perturbation theory. It is found that the two-photon absorption coefficient of monolayer graphene is monotonously dependent on the forth-order of the optical wavelength. For bernal stacked bilayer graphene, the spectrum shows a strong resonant peak at 0.4 eV and decreases monotonously with the third-order of optical wavelength on the blue side of the resonant peak in the spectrum. It is also found that the two-photon absorption of AB stacked bilayer graphene is greatly enhanced

comparing with monolayer graphene.

The study of saturable absorption and two-photon absorption of graphene will facilitate the application of graphene in generating ultrashort laser pulses and injection of ballistic photocurrents in graphene.

List of Tables

List of Figures

carrier-optical phonon scattering, after a time scale of τ_1 ~100 fs, a quasi-equilibrium state with Fermi-Dirac distribution is reached. (c) Due to carrier-acoustic phonon scattering, subsequent thermalization of the carriers happens a time scale of few picoseconds. The original state of system restored.

Figure 2.1. Photograph of UHV and *in-situ* STM facilities for growth and characterization of the graphene samples.

Figure 2.2. (a) The atomic structure of SiC single crystal. (b) The atomic structure of monolayer epitaxial graphene on the C-face of SiC. (c) The sketch of atomic structure of AB stacked bilayer graphene on SiC. (d) The top view of AB stacked bilayer graphene. (e) The side view of AB stacked bilayer graphene and the interlayer interaction.

Figure 2.3. (a) Photograph of the epitaxial graphene samples on SiC substrate. (b) Sketch of the epitaxial graphene samples on SiC substrate. (c) Sketch of the position where the optical characterization carried out.

Figure 2.4. The schematic set-up of Scanning Tunneling Microscopy (STM).

Figure 2.5. (a) The STM image of monolayer graphene on the C-face of SiC, which shows the hexagonal lattice structure, (b) The STM of bilayer graphene on the C-face of SiC. On the right side of the bright line, the clear triangular pattern indicates Bernal-stacking, as discussed in the text. On the left side, the absence of clear triangular pattern implies non-AB-stacking. The bilayer graphene sample consists of AB-stacking domains and non-AB-stacking domains on an area of 50 μm×50 μm.

Figure 2.6. The energy diagram illustration of Raman scattering and the experimental set-up of Raman spectroscopy.

Figure 2.7. (a) Micro-Raman spectra of the mono-, bi- and 6-layer graphene on the C-face of SiC. The inset shows one of the three samples. (b) Micro-Raman spectra of 6-layer graphene on the C-face of SiC. The inset shows the micro-Raman mapping of the 6-layer graphene sample.

Figure 2.8. (a) The 2D peak of the Raman spectroscopy of monolayer epitaxial graphene on C-face of SiC, fitted with single Lorentz peak. (b) The 2D peak of the Raman spectroscopy of bilayer epitaxial graphene on C-face of SiC, fitted with four Lorentz peaks. (c) The Raman spectroscopy of 6-layer graphene and the substrate. The attenuation of the SiC substrate signal is used to calculate the number of graphene layers as discussed in the text.

Figure 2.9. The Raman spectra of the graphene samples. For each sample, the Raman spectra of six different points (or position) were recorded for comparison in order to

List of Publications

International Journals:

1. Luo, D.; Sun, X. W.; Dai, H. T.; Liu, Y. J.; **Yang, H. Z.**; Ji, W., "Two-directional lasing from a dye-doped two-dimensional hexagonal photonic crystal made of holographic polymer-dispersed liquid crystals," Appl. Phys. Lett. **95,** 151115 (2009).
2. Luo, D.; Sun, X. W.; Dai, H. T.; Demir, H. V.; **Yang, H. Z.**; Ji, W., "Electrically tunable lasing from a dye-doped two-dimensional hexagonal photonic crystal made of holographic polymer-dispersed liquid crystals," Appl. Phys. Lett. **97,** 081101 (2010).
3. Gu, B.; Ji, W.; **Yang, H. Z.**; Wang, H. T., "Theoretical and experimental studies of three-photon-induced excited-state absorption," Appl. Phys. Lett. **96,** 081104 (2010).
4. Luo, D.; Sun, X. W.; Dai, H. T.; Demir, H. V.; **Yang, H. Z.**; Ji, W., "Temperature effect on the lasing from a dye-doped two-dimensional hexagonal photonic crystal made of holographic polymer-dispersed liquid crystals," J. Appl. Phys. **108,** 013106 (2010).
5. **Yang, H. Z.**; Feng, X. B.; Wang, Q; Huang, H.; Chen, W.; Andrew T. S. Wee; Ji, W., "Giant Two-Photon Absorption in Bilayer Graphene," Nano Lett., **11,** 2622 (2011).
6. Lin N. B.; Liu X. Y.; Diao Y. Y.; Xu H. Y. ;Chen C. Y.; Ouyang X. H.; **Yang,**

H. Z. ; Ji W., "Switching on Fluorescent Emission by Molecular Recognition and Aggregation Dissociation," Adv. Funct. Mater., **22,** 361-368 (2012).

7. Luo, D.; Dai, H. T.; Demir, H. V.; Sun, X. W.; **Yang, H. Z.**; Ji, W., "Spatial angle dependent lasing from a dye-doped two-dimensional hexagonal photonic crystal made of holographic polymer-dispersed liquid crystals," Opt. Express **20,** 9058-9063 (2012).

Conference Presentations:

1. **Yang H. Z.**; Wang Q.; Ji W. , Laser-pulse-duration and spectral dependence of saturable absorption in graphene, Proceedings of SPIE, **8205,** 82050J (2011).
2. **Yang H. Z.**; Wang Q.; Ji W., Saturable absorption of graphene, 7MPSGC (2011), Singapore.

Chapter 1 Introduction

Information technology (IT) devices, such as computers, mobile phones and optical fibers for communications, play an increasingly important role in today's global economics, business, education, entertainment and so on. It is not an overstatement that IT devices have been part of our living nowadays. As such, demands for both communication speed and device efficiency in terms of energy consumption are ever increasing. Furthermore, IT devices are required to be lighter and thinner. To meet these demands, scientists and engineers are constantly searching for novel materials or new material structures, which can offer faster speed in communication, or greater efficiency in device's energy consumption.

Over the last decade, nanotechnology has emerged. With nanotechnology, materials can be made to very small objects, down to nanometers in the physical size, or very thin, down to an atomic layer. One of the examples is the invention of techniques in the making of an atomic-thin, nano-scale material: graphene, which opens a new field in solid-state physics and materials science. Graphene exhibits many unique materials properties, which cannot be found in bulk materials and have applications in communication technology, energy technology and others. To fully realize graphene potentials, research on graphene has been carrying out intensively in many research laboratories around the world. The research reported in this thesis

constitutes one of the above-said endeavors. In the thesis, we report our investigation into nonlinear optical absorption, namely, (i) saturable absorption and (ii) two-photon absorption in graphene.

In the first chapter of the thesis, we provide the reader with background knowledge of nonlinear optics and carbon materials in nanostructures, which lays the foundation for the research reported here. Following that, we specify our research objectives. This chapter is organized as follows: Section 1.1 introduces the basics of nonlinear optical absorption; Section 1.2 concentrates on nonlinear optical absorption in nanocarbon materials; and Section 1.3 outlines the objectives for the research to be reported in this thesis, and defines the scope of this thesis.

1.1 Nonlinear optical absorption

Nonlinear optics is the study on the interaction of matter with intense light and its impact onto the optical responses of matter. The impact, which is termed as nonlinear optical phenomena, manifests itself in the modification in the optical properties of a material in the presence of intense light. Typically, only laser light is sufficiently intense to induce such a modification. The history of nonlinear optics can be traced back to the discovery of second-harmonic generation by Franken *et al.* (1961) [1.1], shortly after the demonstration of the first working laser by Maiman in 1960. Nonlinear optical phenomena are “nonlinear” in the sense that they occur when the optical response of a material to a strong optical field depends in a nonlinear manner on the strength of the optical field, which is measured as light intensity or irradiance

[1.2].

Since 1961, nonlinear optical effects have been systematically investigated and exploited in order to fulfill the realization of commercial optical devices and various technological and industrial applications. The goal is to search for and develop nonlinear optical materials presenting large nonlinearities and simultaneously satisfying various technological and economical requirements. Such a development in nonlinear optical materials, in general, requires an in-depth knowledge of material's nonlinear polarization mechanisms, and of their relation to the material structure.

To gain a deep understanding of nonlinear optical effects, we start from Maxwell's equations, which is one of the pillars for modern physics. Maxwell's equations for the light-matter interaction are given by [1.2, 1.3]

$$\nabla \cdot \boldsymbol{D} = \rho \tag{1.1}$$

$$\nabla \cdot \boldsymbol{B} = 0 \tag{1.2}$$

$$\nabla \times \boldsymbol{E} = -\frac{\partial \boldsymbol{B}}{\partial t} \tag{1.3}$$

$$\nabla \times \boldsymbol{H} = \frac{\partial \boldsymbol{D}}{\partial t} + \boldsymbol{J} \tag{1.4}$$

For dielectric materials, the density of free charge ρ = 0, and the field induced current $\boldsymbol{J}$ = 0. We also consider that these materials are nonmagnetic, so that, $\boldsymbol{B} = \mu_0 \boldsymbol{H}$. However, we allow the material to be nonlinear in the sense that the fields $\boldsymbol{D}$ and $\boldsymbol{E}$ are related by $\boldsymbol{D} = \varepsilon_0 \boldsymbol{E} + \boldsymbol{P}$, where in general the polarization vector $\boldsymbol{P}$ depends nonlinearly upon the local value of the electric field strength $\boldsymbol{E}$. Then, Maxwell's equations can be derived into the form,

$$\nabla^2 \mathrm{E} - \frac{1}{c^2}\frac{\partial^2}{\partial t^2}\mathrm{E} = \frac{1}{\varepsilon_0 c^2}\frac{\partial^2 \mathrm{P}}{\partial t^2} \tag{1.5}$$

In the nonlinear medium, the polarization ***P*** can be expanded in the form [1.2, 1.3]:

$$\boldsymbol{P} = \varepsilon_0(\chi^{(1)}\boldsymbol{E} + \chi^{(2)}\boldsymbol{E}^2 + \chi^{(3)}\boldsymbol{E}^3 + ...) \tag{1.6}$$

Here, we ignore the nature of vectors, ***P*** is denoted as the modulus of the material polarization in order to give a simple algebra equation for the sake of simple explanation, $\chi^{(1)}$ denotes the linear susceptibility, and the quantities $\chi^{(2)}$, $\chi^{(3)}$, … are called the nonlinear optical susceptibilities of the medium. For centrosymmetric crystals, the second-order nonlinear optical interaction vanishes and the third-order nonlinear optical interaction becomes the lowest order nonlinear term in Equation (1.6). If we omit all higher order nonlinear susceptibilities, the polarization for centrosymmetric crystals can be expressed as $\boldsymbol{P} = \varepsilon_0(\chi^{(1)}\boldsymbol{E}+\chi^{(3)}\boldsymbol{E}^3)$. If we assume the light propagating in the **z**-direction, the optical electric field can be expressed as $\boldsymbol{E} = E_0\, e^{i(k_z z-\omega t)}$. Then, if we substitute the above expression for polarization and optical electric field to Equation (1.5), we can obtain,

$$k_z^2 - \frac{\omega^2}{c^2} = \frac{\omega^2}{c^2}\cdot\chi^{(1)} + \frac{9\omega^2}{c^2}\cdot\chi^{(3)}\cdot E^2 \tag{1.7}$$

where the wave vector $k_z = \omega\cdot\tilde{n}/c$, while the complex refractive index $\tilde{n} = n + \mathbf{i}\kappa$. The imaginary part of the complex refractive index κ is related to the attenuation of the propagating beam as $\alpha = 2\,\omega\,\kappa/c$. We also rewrite the expression for $\chi^{(1)}$ and $\chi^{(3)}$ in the complex form as $\chi^{(1)} = \mathrm{Re}\chi^{(1)} + \mathbf{i}\mathrm{Im}\chi^{(1)}$ and $\chi^{(3)} = \mathrm{Re}\chi^{(3)} + \mathbf{i}\mathrm{Im}\chi^{(3)}$, respectively. Finally, we arrive at the expression for the absorption coefficient of the third-order nonlinear optical system under intense laser irradiance as [1.3],

$$\alpha = \frac{\omega}{c\cdot n}(\mathrm{Im}\,\chi^{(1)} + 9\cdot\mathrm{Im}\,\chi^{(3)}E^2) \tag{1.8}$$

Since our research objective is focused on the nonlinear optical absorption of graphene, the following discussion is confined to the imaginary part of nonlinear optical susceptibility only. The reader is advised to read textbooks [1.2, 1.3] on nonlinear optics if he or she is interested in nonlinear optical effects originating from the real part of nonlinear optical susceptibilies.

Nonlinear optical processes may also be divided to parametric and nonparametric processes. In the parametric process, the initial and final quantum-mechanical states of the system are identical. The typical parametric processes are second- or third-harmonic generation, sum and difference-frequency generation, optical parametric oscillation and so on. In the contrary, the nonparametric processes involve the transfer of electron population from one real level to another and energy can be transferred to or from the material. The typical nonparametric processes are saturable absorption, two-photon absorption, excited state absorption, stimulated Raman scattering and so on. In the following, we will focus our discussion onto three nonparametric nonlinear optical processes, namely (1) saturable absorption, (2) multiphoton absorption, and (3) excited state absorption.

1.1.1 Saturable absorption (SA)

Saturable absorption is a nonlinear optical phenomenon, where the optical absorption of a material decreases with increasing light intensity. Such a material is also referred to as a saturable absorber. At sufficiently-high incident light intensity, electrons in the ground state of a saturable absorber are excited to an upper energy

state at such a rate that there is insufficient time for them to decay back to the ground state. As such, the ground state becomes depleted, and the saturable absorber cannot absorb as large a fraction of the incident light any more, as it does under low-intensity conditions.

(a) Quantitative description

(i) Saturable absorption of the two-level systems

A dynamic two-level model for the dominant resonant transition has been established to explain the saturable absorption of homogeneously broadened two-level systems. As shown in the schematic diagram of a two-level system in Figure 1.1, the macroscopic polarization induced in the ensemble of two-level systems by an incident field of frequency ω is [1.2]

$$P(t) = -\mathrm{sgn}(\omega)\,\mathrm{sgn}(\Delta)\frac{Ne^2\left|\mathbf{r}_{ab}\cdot\mathbf{e}\right|^2}{\hbar\sqrt{\Delta^2+\beta^2}}E(t) \tag{1.9}$$

where, $\Delta = \Omega_{ab} - \omega$, is the off-resonance detuning, $e\mathbf{r}_{ab}\cdot\mathbf{e}$ is the dipole moment of the two-level transition, sgn(x) denotes the sign of x, β is the frequency of the periodic oscillations of the energy-level occupation probabilities (called 'Rabi oscillations'), and N is the density of two-level atoms.

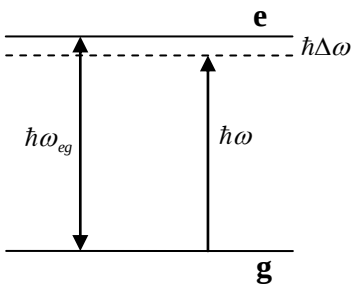

Figure 1.1. Schematic diagram of a two-level system.

In the above discussion, we have assumed that the field is applied adiabatically and also, for the moment, that relaxation is negligible. When compared Equation (1.9) with $P_\omega(t) = \varepsilon_0 \bar{\chi}(\omega; E_\omega) E_\omega(t)$, we obtain the expression [1.2]:

$$\bar{\chi}(\omega; E) = -\mathrm{sgn}(\omega)\,\mathrm{sgn}(\Delta)\frac{Ne^2 \left|\mathbf{r}_{ab} \cdot \mathbf{e}\right|^2}{\varepsilon_0 \sqrt{(\hbar\Delta)^2 + [e|r_{ab} \cdot e|E(t)]^2}} \tag{1.10}$$

Equation (1.10) allows us to make a simple and revealing interpretation of the optical nonlinearity exhibited by the two-level system under steady-state conditions. However, it may be unable to quantify many experimental measurements since the system is too simplified and ignores two important influences: dephasing term and relaxation that are due to interactions with environments. If the depahsing and relaxation times are taken into consideration, the expression for the absorption coefficient can be derived as $\alpha = \alpha_0 (1+I/I_s)^{-1}$, where α_0 is the linear absorption coefficient independent of the light intensity, I and the saturation intensity, I_s is given by [1.2]

$$I_s(\Delta) = \{\frac{2e^2 T_1 T_2}{\varepsilon_0 n_0(\omega) c\hbar^2 [1 + (\Delta T_2)^2]} |\mathbf{r}_{ab} \cdot \mathbf{e}|^2\}^{-1} \quad (1.11)$$

where T_1 is the longitudinal relaxation time and T_2 is the dephasing time for the dipole oscillator. The saturation of the homogeneous transition between energy states E_a and E_b is quantified by the absorption coefficient that depends on the light intensity in the form of $(1+I/I_s)^{-1}$.

The above intensity dependence is derived for homogeneous broadening systems. In an inhomogeneously broadened system, some internal property of the system causes atoms or molecules of the system to have different resonant frequencies. As a result, the absorption saturates less sensitively as compared the homogeneous case, with the intensity dependence form of $(1+I/I_s)^{-1/2}$. In experiments, one directly measured quantity is either light power transmittance or light energy transmittance. Due to the above-discussed saturable absorption, the measured transmittance shows a nonlinear dependence on the light intensity, as illustrated in Figure 1.2. It can be described as lower transmittance at lower light irradiances but becomes high transmittance in the higher-intensity regime.

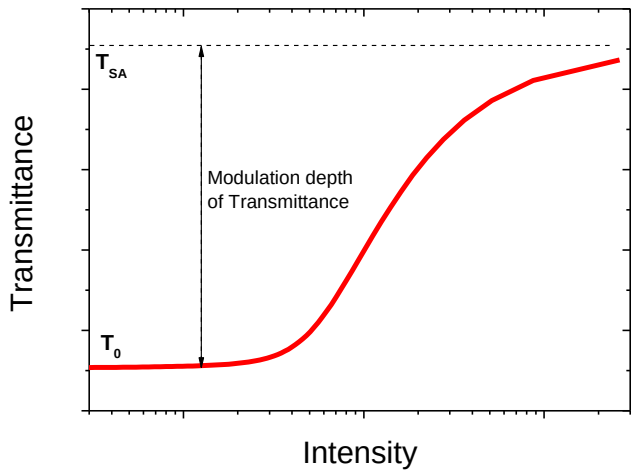

Figure 1.2. Plot of transmittance as a function of incident light intensity for a saturable absorber.

(ii) Saturable absorption of semiconductor materials

The dynamic two-level model described above is suitable for resonant excitation of two-level systems or under ultrashort (subpicosecond) optical excitations that the carriers have not yet scattered out of the states into which they are injected [1.4]. However, when we concern with the nonlinearities, which occur when intense optical radiation pumps carriers from the valence band to the conduction band, the occupation probability of a state in any particular band is usually thermalised by rapid (usually sub-picosecond) intravalley scattering processes. It retains the form of the Fermi-Dirac function but E_f is now different in different bands and is referred to as the quasi-Fermi level. We denote the quasi-Fermi levels in the conduction and valence bands by E_{fc} and E_{fv} respectively. The relationship of electron (hole) density $N^{(e)}$ ($N^{(h)}$) and the quasi-Fermi level can be expressed as [1.2],

$$N^{(e)} = \int_0^{\infty} \mathrm{d}\,\mathrm{E} N_c(\mathrm{E}) / \{\exp[(\mathrm{E} - \mathrm{E}_{\mathrm{Fc}}) / kT] + 1\} \tag{1.12}$$

$$N^{(h)} = \int_{-\infty}^{-E_g} \mathrm{d}\,\mathrm{E} N_v(\mathrm{E}) / \{\exp[(E_{\mathrm{Fv}} - \mathrm{E}) / kT] + 1\} = N^{(e)} \tag{1.13}$$

The modifications of these equations, which are necessary in doped semiconductors, are easily incorporated.

The photo-excited carrier density can be calculated from the elementary rate equation [1.2, 1.3]:

$$dN^{(e)} / dt = \alpha I / \hbar\omega - (N^{(e)} - N_0^{(e)}) / \tau_R \tag{1.14}$$

where τ_R is the electron-hole recombination time, $N_0^{(e)}$ is the value of $N^{(e)}$ in thermal equilibrium. At different excitation light intensity, different photo-excited carrier density gives rise to different quasi-Fermi energies. As a result, the absorption coefficient of the semiconductor depends on the light intensity. From Equations (1.12-1.14), although there is no analytical solution, it can be numerically predicted that the absorption coefficient decreases with the increase in the light intensity, resulting in saturable absorption.

(iii) Saturable absorption of metallic nanostructure materials

Besides semiconductors, metallic nanostructure materials also show saturable absorption under resonant optical excitation. Gold and silver nanoparticles exhibit excellent saturable absorption properties when the exciting beam is resonant with the surface plasma resonance (SPR) [1.5, 1.6]. Plasmons can be described in the classical picture as an oscillation of free electron density with respect to the fixed positive ions

in a metal. Surface plasmons are those plasmons that are confined to surfaces and that interact strongly with light resulting in a polariton as shown in Figure 1.3. SPR condition for spherical particles is satisfied when the dielectric function of metal particles $\varepsilon_m(\omega)$ satisfies, $\varepsilon_m(\omega) + Y_i \varepsilon_S(\omega) = 0.$ Here, $\varepsilon_m(\omega)$, $\varepsilon_s(\omega)$ are the dielectric function of the metal particle and the environment. The parameter Y_i is related to the shape or depolarization factor L_i along the axes *i* of nanoparticles through the equation $Y_i = 1/L_i - 1$ [1.7]. The shape factor $L = 1/3$ represents a sphere, $L = 1$ represents a flat disk, and $L = 0$ represents an infinite columnar structure along the axis of symmetry of the spheroid. Therefore, the spheroidal particles with prolate geometry have a value of *Y* greater than 2, increasing as their aspect ratio *R*, the ratio of long axis to the short axis, increases. The resonance wavelength can thus be determined from the above condition. When the metallic nanoparticles are under intense laser irradiance, the absorption due to SPR will be saturated. The model of Fermi-smearing explains the mechanism of saturable absorption of SPR [1.8]. As shown in Figure 1.4, the intense excitation changes the carrier distribution in the conduction and valence band. The ultrafast intraband thermalization causes the hot carriers to reach a quasi-equilibrium state. The redistribution of the carriers blurs the Fermi level and modifies the dielectric constant of the metallic nanoparticles.

The SPR spectrum as well as the nonlinear optical response can be tuned by adjusting the shape or environment of the metallic nanostructure particles. The SPR is widely used in the fields of Surface Enhanced Raman Spectroscopy (SERS) [1.9, 1.10] and biochemists to study the mechanisms and kinetics of ligands binding to receptors.

It has also been found that metallic nanoparticles exhibits ultrafast and large magnitude of nonlinear optical response and have the potential for the application of ultrafast all-optical switching.

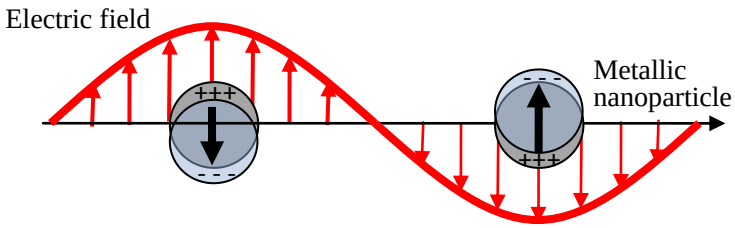

Figure 1.3. Surface Plasmon Resonance of noble metal (Au, Ag, Cu …) nanoparticals.

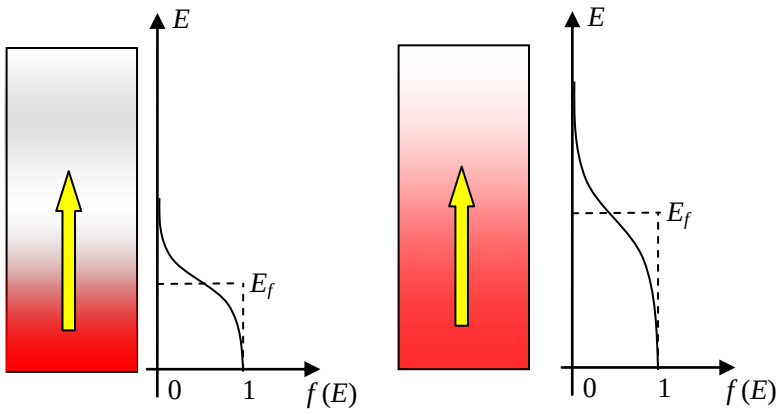

Figure 1.4. Schematic of Fermi level smearing effect due to strong optical excitation.

(b) Light propagation in saturable absorbers

When light propagates through the above homogeneous broadening systems, the

attenuation of light can be described by [1.11],

$$\frac{dI}{dz} = -\alpha(I)I = -\frac{\alpha_0 I}{1 + I / I_s} \tag{1.15}$$

And for inhomogeneous broadening systems,

$$\frac{dI}{dz} = -\alpha(I)I = -\frac{\alpha_0 I}{\sqrt{1 + I / I_s}} \tag{1.16}$$

In general, there is no analytical solution for the transmitted light intensity. With currently powerful computers, the solution can be obtained by numerical techniques. More details on numerical computation methods will be discussed in detail in Chapter 3.

Furthermore, the saturable absorption can be reduced to a third-order nonlinear optical process if the excitation light intensity is not so intense. In Equation (1.15), $\alpha(I)$ can be approximated to $\alpha_0(1\text{-}I/I_s)$ and α_0/I_s should be related to the imaginary part of third-order nonlinear susceptibility, $\mathrm{Im}\chi^{(3)}$, in Equation (1.8).

(c) Applications

Materials, which show saturable absorption properties, can be used as saturable absorber in mode-locking to generate ultrashort laser pulses. Mode-locking is a technique in optics by which a laser can be made to produce pulses of light of extremely short duration on the order of picoseconds (10^{-12} s) or femtoseconds (10^{-15} s). The basis of the technique is to modulate the phase between the longitudinal modes so that interference enhancement could be realized in the laser cavity. The laser is then said to be mode-locked. Interference enhancement of the longitudinal modes in

the laser cavity generates ultrashort pulses with high peak intensities. The usage of saturable absorber in the laser cavity to realize mode-locking is called passive mode-locking. The pulse duration and peak intensity of the laser pulses generated in the passive mode-locked laser dependent on the number of longitudinal modes that are 'locked', which are sensitively dependent on the behavior of the saturable absorber. The modulation depth, spectral responsibility, the recovery time, and saturation intensity (or fluence) are important parameters that determine the performance of saturable absorber in generating ultrashort laser pulses. The modulation depth is the transmittance difference of saturable absorber under weak and intensity laser irradiance, as shown in Figure 1.2. The spectral responsibility of a saturable absorber corresponds to the wavelength range, where saturable absorption happens, which is often related to the linear absorption resonance [1.12, 1.13]. The recovery time, which determines the operating frequency of the saturable absorber, is the time when the saturable absorber restores its original states after photo-excitation. The saturation intensity (or fluence), which is an important parameter in defining the responsibility of a saturable absorber, is usually defined as the intensity (or fluence), at which the absorption coefficient drops to half of its original value.

The initial idea of passive mode-locking by saturable absorber was demonstrated in semiconductor diode lasers in the early 1980's [1.14-1.16]. Pulses as short as 650 fs with the center wavelength of 813 nm were achieved in GaAs buried optical guide semiconductor lasers in 1981 [1.16]. Since 1992, semiconductor saturable absorbers have become important components in the compact mode-locking solid-state lasers

[1.17]. The semiconductor saturable absorber mirror (SESAM) is a saturable absorber that operates in reflection configuration. The typical structure of SESAM is shown in Figure 1.5(a). During the past decade, the device design, fabrication and long-term device reliability have been significantly improved. There are SESAM designs that can cover wavelengths from 800 nm to 1600 nm, pulse width from femtoseconds to nanoseconds, and power levels from milliwatts to more than 100 watts. The typical relaxation dynamics of photon-excited electron in semiconductors and the transient distribution of electrons are illustrated in Figure 1.5(b). For semiconductor saturable absorbers, when it is under strong excitation, the absorption is saturated because possible initial states of the pump transition are depleted while the final states are partially occupied. Within 60~300 fs of excitation, the carriers in each band thermalize, and this leads to a partial recovery of the absorption. On a longer time scale, typically between a few picoseconds and a few nanoseconds, the carriers are removed by recombination and trapping. Mode-locking benefits from the presence of two different time scales. The longer time constant results in a reduced saturation intensity for a part of the absorption, which facilitates self-starting mode-locking, whereas the faster time constant is more effective in shaping subpicosecond pulses. Therefore, SESAM allows us to easily obtain self-starting mode-locking [1.18]. Typically, SESAM is operated with an incident pulse fluence of about three to five times that of the saturation fluence. In such a condition, the absorber provides nearly the maximum modulation depth without damage. Higher saturation level also reduces the tendency for Q-switching instabilities because of thermal effects and/or

two-photon absorption.

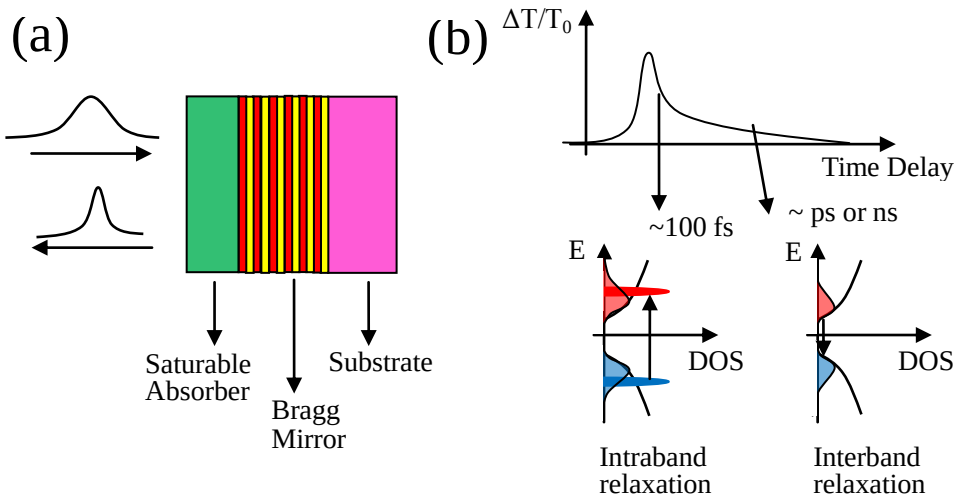

Figure 1.5. (a) Schematic diagram of the structure of semiconductor saturable absorber mirror (SESAM). (b) Ultrafast photoexcited carrier dynamics in SESAM [1.18].

1.1.2 Multi-photon absorption (MPA)

It should be emphasized that the occurrence of saturable absorption is not exclusive. In general, other nonlinear optical processes can also take place in saturable absorbers. Two-photon absorption (2PA) is such a nonlinear process and it could be present in SESAMs, as demonstrated by time-resolved differential reflectivity measurements [1.19, 1.20]. It has been demonstrated that 2PA can increase the region for stable continuous wave mode-locking (CWML) and it can enable a laser to reach a CWML state that was not previously attainable. In this section, our discussion will be focused on 2PA.

(a) Quantitative description

Multi-photon absorption (TPA) is another important nonlinear process. In this process, the material simultaneously absorb *n* (*n*>=2) photons of identical or different frequencies in order to excite an electron from one state (usually the ground state) to higher electronic states.

The typical MPA processes are the two-photon absorption (2PA) and three-photon absorption (3PA), which belong to third and fifth-order nonlinear optical process, respectively. The degenerate 2PA and 3PA processes are sketched in Figure 1.6. The energy difference between the involved lower and upper states of the material is equal to the sum of the energies of 2 or 3 photons.

Two-photon absorption was originally predicted by Maria Goeppert-Mayer in 1931 [1.21]. In 1961, attributed to the invention of the laser, two-photon absorption was firstly verified in experiment [1.22] and then it was observed in a vapor (cesium) in 1962 [1.23].

MPA is several orders of magnitude weaker than linear absorption. It differs from linear absorption in that the strength of absorption depends on the higher order of the light intensity. The intensity dependent absorption coefficient of *n*-photon absorption materials can be expressed as $\alpha_0+\alpha_n I^{n-1}$, where, α_0, α_n are the linear and *n*-photon absorption coefficients. The 2PA coefficient is related to the imaginary part of the third-order nonlinear susceptibility by $\mathrm{Im}\chi^{(3)}(\mathrm{esu}) = c^2 n_0^2 \beta / 240\pi^2 \omega$, where, c (m/s) is the optical velocity in vacuum, n_0 is the refractive index of the medium, β (m/W) is the 2PA coefficient, ω (rad s^{-1}) is the angular frequency of the light field.

The 2PA coefficient β is a macroscopic parameter characterizing the 2PA

properties of material. Often, there is interest in the individual molecular 2PA property that is described by the 2PA cross-section σ_2 ($\sigma_2 = \beta\hbar\omega/N$, N is the molecular density).

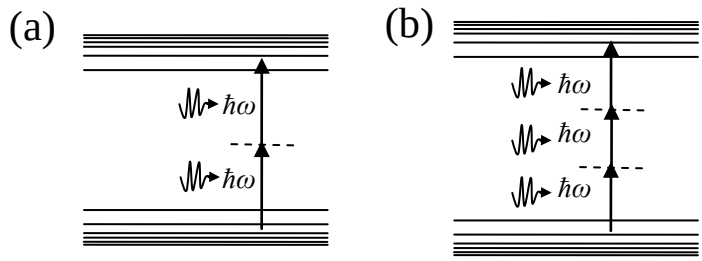

Figure 1.6. Schematic diagram of degenerate 2PA and 3PA.

The selection rules for 2PA are different from one-photon absorption, which is dependent on the first-order susceptibility. In quantum mechanical terms, this difference results from the need to conserve angular momentum. Since photons have spin of ± 1, one-photon absorption requires an electron changing its angular momentum difference by ± 1, while, two-photon absorption requires a change of +2, 0,or -2.

The 2PA coefficient can be theoretically calculated by the second-order quantum perturbation theory [1.24-1.26]. Second-order quantum perturbation theory is a microscopic approach, in which, the two-photon induced electronic transition probabilities are calculated. Besides, a macroscopic approach was also studied [1.27, 1.28], in which, the 2PA coefficients are obtained from the imaginary part of the third-order nonlinear susceptibilities.

Based on the second-order quantum perturbation theory, the two- and three-photon generation rate of electron-hole pair in a system can be expressed as: [1.25]

$$W^{(2)} = \frac{2\pi}{\hbar}\sum_{v_1,v_0}\left|\sum_{v_2}\frac{V_{v_1,v_2}V_{v_2,v_0}}{E_{v_2}-E_{v_0}-\hbar\omega-i\hbar\gamma_{v_2}}\right|^2\delta(E_{v_1}-E_{v_0}-2\hbar\omega) \tag{1.17}$$

$$W^{(3)} = \frac{2\pi}{\hbar}\sum_{v_1,v_0}\left|\sum_{v_3}\sum_{v_2}\frac{V_{v_1,v_3}V_{v_3,v_2}}{E_{v_3}-E_{v_2}-2\hbar\omega}\cdot\frac{V_{v_2,v_0}}{E_{v_2}-E_{v_0}-\hbar\omega}\right|^2\delta(E_{v_1}-E_{v_0}-3\hbar\omega) \tag{1.18}$$

where v_0, v_1, and v_2 denote sets of quantum numbers for initial, final, and intermediate states of an electron system. γ_v is the inverse lifetime of the state v. V is the electron-photon interaction $V_{m,n} = \left\langle \psi_m \left| \frac{e}{mc}\boldsymbol{A}\cdot\boldsymbol{P} \right| \psi_n \right\rangle$.

The above mentioned basic multi-photon absorption theory can be applied to any system. However, it is essential to investigate the MPA properties and their relation to material structures in light of the unique energy levels and wave functions of the systems.

Two-photon absorption can be experimentally measured by several techniques, such as two-photon excited fluorescence, nonlinear transmission and Z-scan experiment. Pulsed lasers are often used because two-photon absorption is a third-order nonlinear optical process, and therefore is more pronounced at high intensities.

(b) Light propagation in two-photon absorbers

The attenuate of the beam in 2PA materials is expressed as [1.29, 1.30],

$$dI/dz = -(\alpha_0 + \beta I)I \tag{1.19}$$

where α_0 is the linear absorption coefficient, β is two-photon absorption coefficient. In this case, analytical solution can be obtained as shown in the following.

For a sample with length of L, the beam intensity at the exit of the sample can be derived from Equation (1.19) as,

$$I^{out} = I^{in} /(1+\beta I I_0) \tag{1.20}$$

The normalized energy transmittance for 2PA materials can be obtained as well by spatial and temporal integration. For the pulsed Gaussian beam, it can be expressed as [1.29, 1.30],

$$T = \frac{1}{\sqrt{\pi} q_0} \int_{-\infty}^{\infty} \ln[1+q_0 \exp(-x^2)] dx \tag{1.21}$$

In the above equation, $q_0 = \beta I_0 L_{eff}$; $I_0 = I_{00}/(1+z^2/z_0^2)$ is the excitation intensity at position z; $z_0 = \pi\omega_0^2/\lambda$ is the Rayleigh range. ω_0 is the minimum beam waist at the focal point (z = 0); λ is the laser free-space wavelength; $L_{eff} = [1-\exp(-\alpha_0 L)]/\alpha_0$ is the effective length, and L is the sample length.

Similarly, the attenuation of the beam in the 3PA materials can be expressed as

$$dI / dz = -(\alpha_0 + \alpha_3 I^2) I \tag{1.22}$$

For the pulsed Gaussian beam, the normalized energy transmittance for 3PA materials can be expressed as [1.30],

$$T = \frac{1}{\sqrt{\pi} p_0} \int_{-\infty}^{\infty} \ln\{[1+p_0^2 \exp(-2x^2)]^{1/2} + p_0 \exp(-x^2)\} dx \tag{1.23}$$

In the above equation, $p_0 = (2\alpha_3 I_0^2 L_{eff}')^{1/2}$, $L_{eff}' = [1-\exp(-2\alpha_0 L)]/2\alpha_0$ is the effective length.

(c) Applications

Multi-photon absorption is essential in a wide application range such as multi-photon excitation microscopy, multi-photon micro-fabrication and lithography, photodynamic therapy, optical limiting, and optical data storage. Multi-photon excitation microscopy is a fluorescence imaging technique that allows

three-dimensional sectioning into thicker tissues, which is up to about one millimeter. The multi-photon excitation microscopy uses red-shifted excitation light, which can also excite fluorescent dyes. However, for each excitation, two photons of the infrared light are absorbed. Infrared light minimizes scattering in the tissue. Besides, the background signal is strongly suppressed due to multi-photon absorption. Both effects lead to an increased penetration depth in these microscopes. However, the resolution is still limited by diffraction. Multi-photon excitation can be a superior alternative to confocal microscopy due to its deeper tissue penetration, efficient light detection and reduced photo-toxicity [1.31, 1.32]. Two-photon microscopy was firstly realized by Winfried Denk at Cornell University in 1990s. He combined the idea of 2PA with the use of laser scanner [1.33]. In multi-photon excitation microscopy, an infrared laser beam is focused through an objective lens. The Ti-Sapphire laser with femtosecond laser pulses and high repetition rates are normally used in multi-photon excitation microscopy. It allows the high photon density and flux required for multi-photon absorption and is tunable across a wide range of wavelengths.

Multi-photon absorption materials can also be used in optical limiting to protect human eyes or sensitive optical detectors. The optical limiting material has high linear transmittance, but as the irradiance increases, the multi-photon absorption increases and the transmittance decreases to reduce the amount of light intensity that is received by human eyes or light sensors. It has been demonstrated that MPA materials exhibits excellent optical limiting properties [1.34].

1.1.3 Excited-state absorption (ESA) and free carrier absorption (FCA)

There is one more nonlinear optical process, which is often encountered. It is known as excited state absorption (ESA) in the case of organic molecules or polymer, or free-carrier absorption (FCA) in the case of semiconductors. Sometimes, ESA is also referred to as reverse saturable absorption (RSA). The more detailed description on ESA and FCA is given below.

(a) Qualitative description

When the excited state becomes significantly populated via one-photon absorption between the ground state and the excited state in the case of molecules or polymers, there is another possibility of these excited electrons being further photo-excited to another higher excited state. For this case, a three-level model has been established to interpret the ESA processes, as sketched in Figure 1.7(a). In the energy diagram of ESA materials, there are a number of higher-lying states (denoted as State S_2) and for which the energy differences are in near-resonance with the incident photon energy. Therefore, before the electron at lower-lying excited states (denoted as State S_1) completely relaxes to the ground state, it may experience absorption that promotes it to State S_2. This process is therefore called excited state absorption (ESA).

When the absorption cross-section of State S_1 is smaller than that of the ground state, the transmission of the system is increased when the system is highly excited. This process enhances the saturable absorption (SA) of the ground state (S_0).

When the absorption cross-section of State S_1 is larger than that of State S_0, then the system is less transmissive when excited. This gives the opposite effect to saturable absorption and is thus called reverse saturable absorption (RSA).

For a polyatomic molecule, the above three-level model is insufficient and a five-level model is required to interpret the ESA processes. As shown in Figure 1.7(b), the ground electronic state is called a singlet state. These states have a pair of electrons with anti-parallel spins. Absorption from the ground state causes electron transit only to another singlet electronic state. However, it is possible to produce a spin flip by external processes such as collisions with paramagnetic ions, or internal processes such as strong spin-orbit coupling. Under such conditions, the first excited electronic state may make a radiationless transition to a lower-laying triplet state (i.e. a state with a pair of electrons having parallel spins). The same as the singlet states, the radiative transition from one triplet state is only allowed to another triplet state. There are two possibilities for electron in the lowest triplet state. It may relax by another spin-flip transition to the ground state. This occurs by a process called phosphorescence with an associated rate constant k_{ph}. The other possibility is that the electron is promoted to a higher-lying triplet state by absorbing another photon. Then, the electron relaxes back to the lowest triplet state.

In semiconductors, the absorption of a photon with energy greater than the band gap promotes an electron from the valence band to the conduction band, where it is a free carrier and can contribute to current flow when an electrical field is applied. At the same time, a hole is created in the valence band and it can also form a current if an electrical field is present. The photo-created electron or hole rapidly thermalizes and relax to the bottom of the conduction band or the top of the valence band, respectively. From there, the electron-hole pair recombines subsequently with a characteristic

recombination time. However, at sufficiently high intensities, the photo-created electron (or hole) can absorb another photon to make a transition to a higher (or lower) state while it is still in the conduction (or valence) band. This process is called free carrier absorption. It has similar qualitative characteristics to reverse saturable absorption.

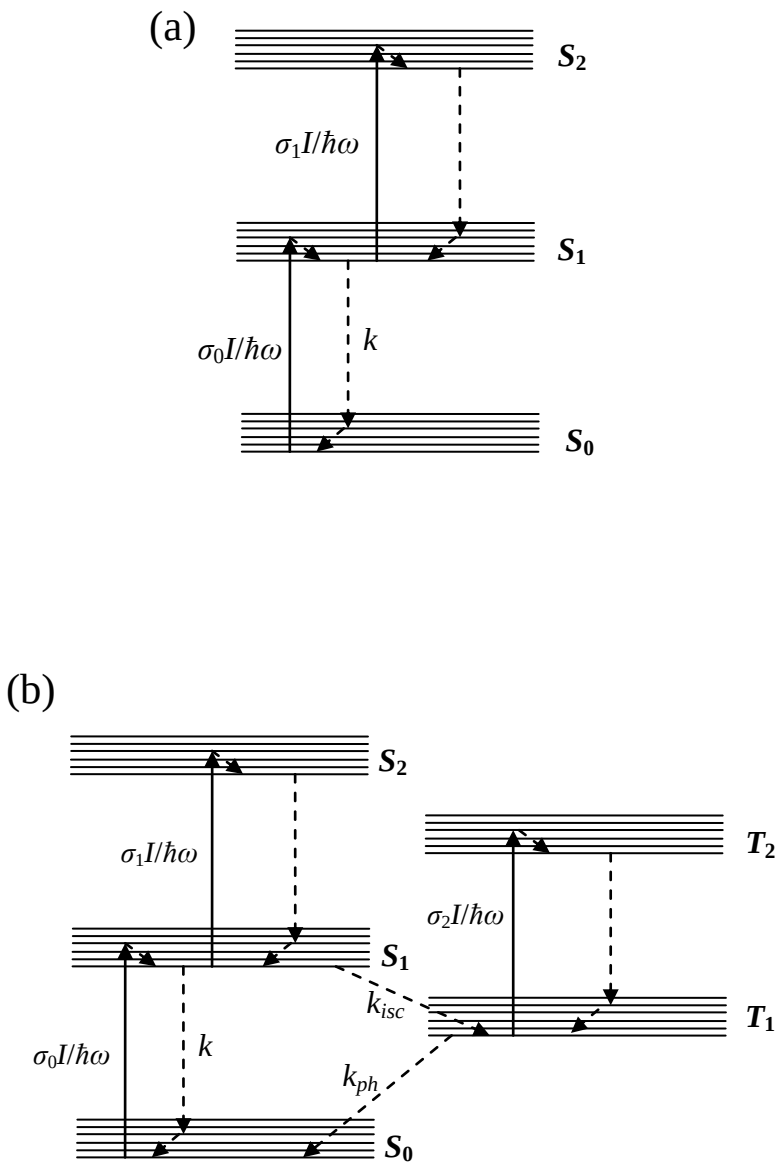

Figure 1.7. Schematic diagram of (a) three- and (b) five-level system.

(b) Light propagation in excited-state absorbers

The mathematical treatment to the above-mentioned ESA or FCA has been described elsewhere [1.2, 1.3]. As example, the mathematical equations for the three-level model are described briefly as follows. As discussed above, for the three-level model, the rate equations of the population densities at important states, S_0 and S_1 (the ground and first excited states, respectively) may be written as follows. Introducing the dimensionless quantities $S_0 = N_{S0}/N$, $S_1 = N_{S1}/N$, where N_{S0}, N_{S1} are the population densities of the S_0 and S_1 states, respectively, N is the total number density of molecules.

$$\frac{\partial S_0}{\partial t} = -\frac{\sigma_0 I}{\hbar\omega} S_0 + kS_1 \tag{1.24}$$

$$\frac{\partial S_1}{\partial t} = \frac{\sigma_0 I}{\hbar\omega} S_0 - \frac{\sigma_1 I}{\hbar\omega} S_1 - kS_1 \tag{1.25}$$

The attenuation of the incident light is described by

$$\frac{dI}{dz} = -\sigma_0 S_0 NI - \sigma_1 S_1 NI \tag{1.26}$$

In Equations (1.24-1.26), I is the light intensity, σ_0 and σ_1 are the absorption cross-sections for the ground and excited states, respectively. Also, by conservation of number density, $S_0+S_1 =1$. k is the net rate constant of transition. In general, there is no analytical solution to Equations (1.24-1.26), and numerical solution can be obtained.

(c) Applications

There has been considerable activity in the research on RSA materials for optical limiting. Many RSA materials that have been developed and studied include Cr^{3+}-doped alexandrite, indanthrones, phthalocyanines and naphthalocynanines,

heavy atom substituted phthalocyanines, iron-tricobalt cluster complexes, platinum poly-ynes, metallotetrabenzoporphyrins, King's complex (cyclopentadieneyliron carbonyl tetramer), fullerenes, and N-methylthioaridone [1.3].

1.2 Nonlinear optical absorption in nanocarbon materials

Carbon materials, which are completely composed of carbon, have various allotropes. In the nature, graphite and diamond are the bulk allotrope of carbon. From the last decades, a serial of novel nanostructures of carbon allotropes have been discovered. They include Fullerene, Carbon nanotubes, and graphene. The atomic structure of these carbon allotropes are sketched in Figure 1.8. Most of the carbon family materials are excellent conductors with high electron mobility, due to the hybridized sp^2 orbital as shown in Figure 1.9. The sideway overlapping of *2p* orbitals between neighboring carbon atoms form a π-bonding system where a "cloud" of electrons can move about.

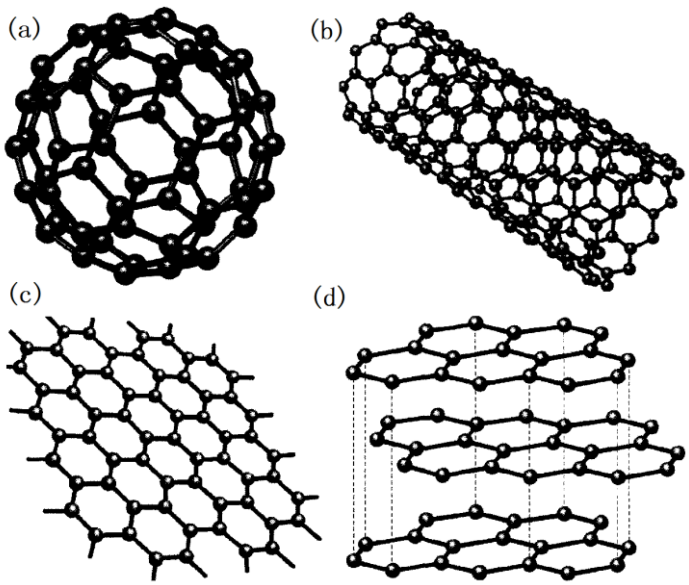

Figure 1.8. Schematic of Carbon family materials (a) C_{60} (b) Carbon nanotube (c) Graphene (d) Graphite.

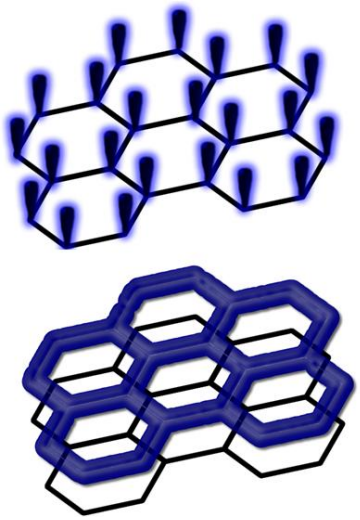

Figure 1.9. Schematic of the overlapping of π orbitals in sp^2 hybridized Carbon family materials. The overlapping of π orbital creates one big orbital, which extends across the whole material.

1.2.1 Excited-state absorption (ESA) in fullerene

A fullerene is the molecule composed entirely of carbon, in the form of a hollow sphere, ellipsoid, or tube. Spherical fullerenes (C_{60}, C_{70} *et al.*) are the most popular

form of fullerene. The existence of C_{60} was predicted by Eiji Osawa of Toyohashi University of Technology in 1970 [1.35]. The first carbon nanostructure buckminsterfullene (C_{60}) was prepared in 1985 by Richard Smalley *et al.* at Rice University [1.35]. The technique of isolating and purifying macroscopic quantities of C_{60} has generated unprecedented interest in the chemical and physical properties of this molecule [1.37, 1.38]. C_{60}, as shown in Figure 1.8 (a), is like a buckyball with diameter of 0.683 nm. Fullerenes are sparingly soluble in many solvents, which include aromatics, such as toluene and carbon disulfide. Solutions of pure C_{60} have a deep purple color. The energy gap between HOMO and LUMO states is around ~2 eV. The nonlinear optical properties of C_{60} have been studied intensively [1.39-1.43]. Large third order nonlinear susceptibly and ultrafast response time of C_{60} has been demonstrated by quantum mechanical theory and four-wave-mixing measurement [1.44].

Reverse saturable absorption is an important nonlinear optical absorption property of C_{60}. As shown in the energy diagram of C_{60} in Figure 1.10, the absorption of the ground state is much smaller than that of the excited states S_1 and T_1 in the visible and near-infrared wavelength region (>= 400 nm). The absorption peaks for the excited state S_1 are at 513, 759, and 885 nm and for the excited state T_1 are at 457, 509, and 747 nm [1.45]. Therefore, condition for reverse saturable absorption in C_{60} is easily satisfied for a wide wavelength range.

Reverse saturable absorption of C_{60} was studied at 532 nm with nanosecond and picosecond pulses [1.45]. The excited state absorption cross section (S_1) was

measured to be 1.57×10^{-17} cm^2, which is much higher than that of the ground state absorption cross section ($\sigma_{S0} = 2.87\times10^{-18}$ cm^2). The reverse saturable absorption of C_{60} and its derivatives indicates that they are excellent candidates for the application of optical limiting.

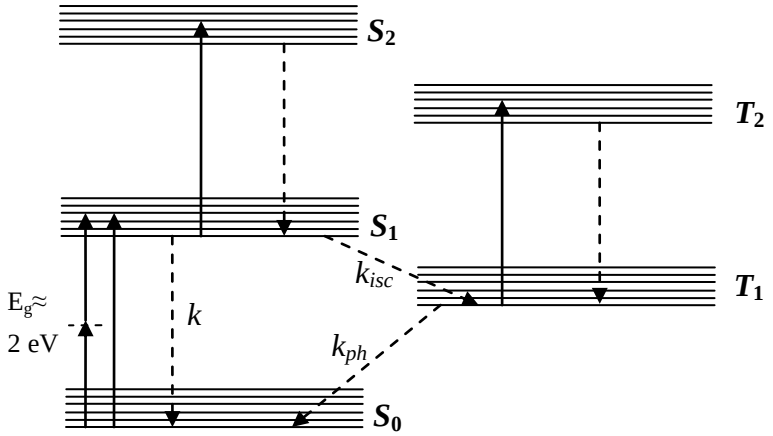

Figure 1.10. Schematic diagram of energy levels for C_{60}.

1.2.2 Two-photon absorption (2PA) in fullerene

Two-photon absorption is also an important nonlinear optical phenomenon in fullerene. As shown in Figure 1.10, when the exciting photon energy is below the energy bandgap of HOMO and LUMO (~2 eV for C_{60}), ground state electrons in fullerene simultaneously absorb two photons to be excited to the excited states.

Two-photon absorption spectrum of C_{60} has been measured in a wide spectrum range 0.7-1.5 μm with femtosecond pulses (150 fs, 1 kHz) by measuring the nonlinear transmission of C_{60} thin films [1.46]. In the measurement, the excited state absorption in C_{60} can be omitted under femtosecond excitation. It was found that the two-photon absorption spectrum was characterized by a maximum at $2\hbar\omega$ = 2.58 eV. The

two-photon absorption coefficient β of the C_{60} thin film showed a broad peak, with β ~ 25 cm/GW, around 0.95 μm and drops below 3 cm/GW at λ > 1.2 μm.

1.2.3 Saturable absorption (SA) in carbon nanotubes

Carbon nanotubes (CNTs) is another allotropes of carbon with a cylindrical nanostructure as shown in Figure 1.8 (b). Nanotubes were observed in 1991 in the carbon soot of graphite electrodes during an arc discharge [1.47]. However, the first macroscopic production of carbon nanotubes was made in 1992 by two researchers using arc discharge method at NEC's Fundamental Research Laboratory [1.48].

Carbon nanotubes can be formed by rolling the graphene sheet at specific discrete ("chiral") angles, and the combination of the rolling angle and radius decides the nanotube properties; for example, whether the individual nanotube shell is a metal or semiconductor. According to the number of walls that form the nanotube, carbon nanotubes are categorized as single-walled nanotubes (SWNTs) and multi-walled nanotubes (MWNTs). MWNTs is metallic as graphite. SWNTs can be metallic or semiconductor [1.49], which is determined by the chiral angle and diameter. Theoretical works indicates that SWNTs has characteristic electronic structure due to a low dimensionality, such as spike like density of states due to one-dimensional van Hove singularity, as shown in Figure 1.11 (b). The π band of SWNTs was calculated and the sharp resonant optical transitions between spikes of density of states were predicted, which is so called Kataura plot [1.50], as shown in Figure 1.11 (a). Kataura plot supplies a convenient way of characterizing SWNTs samples by measuring

optical absorption spectra. Besides, many electronic applications of carbon nanotubes rely on techniques of selectively producing either semiconducting or metallic CNTs, preferably of certain chirality. Many research works have been carried out for purifying the SWNTs using techniques, such as density-gradient ultracentrifugation [1.51, 1.52].

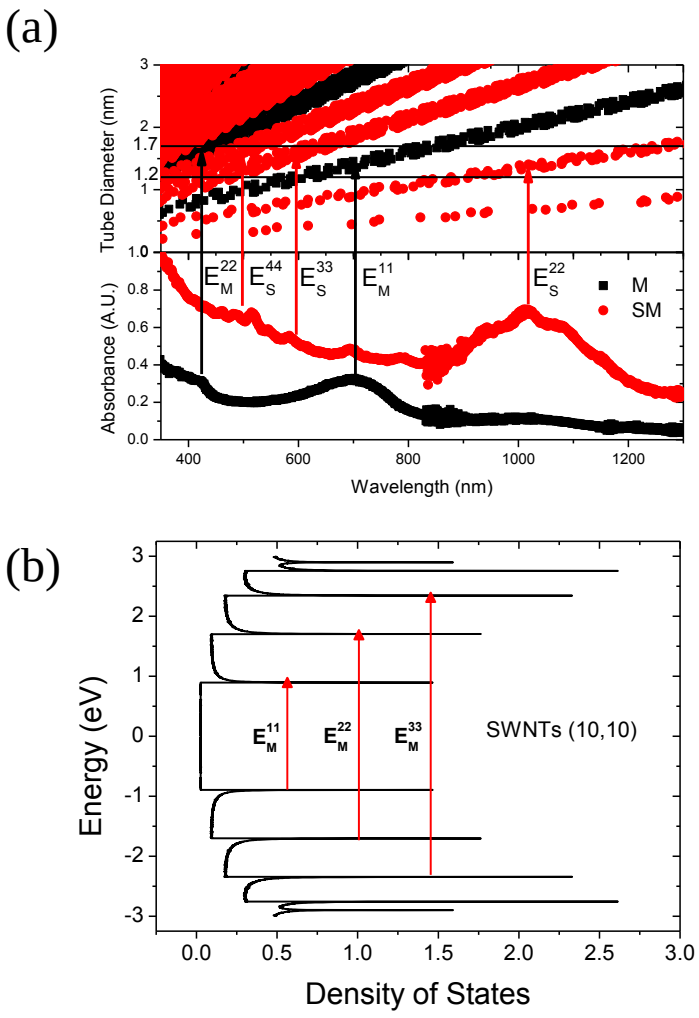

Figure 1.11. (a) The Kataura plot of SWNTs and comparison with absorbance spectrum of metallic and semiconductor SWNTs [1.53]. (b) The dispersion of density of states of SWNTs with chirality of (10,10).

The ultrafast photo-excited carrier dynamics in CNTs has been studied intensely since it was discovered. The time-resolved pump-probe measurements under resonant

excitation in an assembly of metallic and semiconducting single-walled carbon nanotubes (thin film) were conducted in 2003 [1.54]. The transient photo-bleaching effect was observed for degenerate measurements on the first interband transition of the semiconducting tubes (E_s^{11}), with a typical recovery time of 1 ps. In a subsequent report, the two-component dynamics was observed by carrying out pump-probe spectroscopy of micelle-suspended single-walled carbon nanotubes in at various wavelengths. A slow component (5-20 ps) was resonantly enhanced whenever the pump photon energy coincides with an absorption peak and it was attributed to interband radiative carrier recombination [1.55].

The saturable absorption of vertical aligned MWNTs thin films (1.3 μm) was studied using Z-scan technique under nonresonant excitation in the spectral range of 720 – 780 nm [1.56]. A large third order nonlinear susceptibility ($\left|\chi^{(3)}\right|$~2.2×10^{-11} esu ≈ 3.1×10^{-19} $m^2 \cdot V^{-2}$) was observed due to the high concentration of MWNTs packed in a 1.3-μm-thick layer. Semiconducting SWNTs are also reported to be good saturable absorbers [1.13, 1.57, 1.58]. Chen *et al.* measured saturable absorption in SWNTs at 1550 nm by means of pump-probe spectroscopy, and reported $\chi^{(3)} \sim 10^{-10}$ esu (≈ 1.4×10^{-18} $m^2 \cdot V^{-2}$) [1.57]. Later, Tatsuura et al. got $\chi^{(3)}$~10^{-7} esu (≈1.4×10^{-15} $m^2 \cdot V^{-2}$) in resonant conditions, using a pump pulse with energy equal to that of the E_s^{11} transition in the SWNTs absorption spectrum [1.58]. A quantitative Im$\chi^{(3)}$ spectra of SWNTs was evaluated in the whole energy region of the gap transition in the semiconducting SWNTs using Z-scan technique [1.13]. |Im$\chi^{(3)}$| was found to be remarkably enhanced under resonant excitation to the gap transition, reaching 4.2×

10^{-6} esu ($\approx 5.9\times10^{-14}$ $m^2 \cdot V^{-2}$) in L-SWNTs (laser ablation produced SWNTs) and 1.5×10^{-7} esu ($\approx 2.1\times10^{-15}$ $m^2 \cdot V^{-2}$) in H-SWNTs (HiPco method produced SWNTs). The reported values are higher than other nanomaterials and semiconductors [1.59, 1.60]. For example, $\chi^{(3)} \sim 10^{-12}$ esu ($\approx 1.4\times10^{-20}$ $m^2 \cdot V^{-2}$) was reported for $AgInSe_2$ nanorods [1.59], and $\sim10^{-12}$ esu in PbS [1.60], which were investigated, like SWNTs, as alternatives for conventional SESAMs. A comparison of the reports of saturable absorption of CNTs and other saturable absorption materials is listed in Table 1.1. SWNT-based saturable absorbers incorporating nanotubes (SAINTs) for passive mode-locking could operate in a wide range of wavelengths from 1 to 1.99 μm in fiber and bulk solid state laser systems. SAINTs has been used to mode-lock Er/Yb:glass bulk lasers at 1.55 μm [1.61, 1.62], Cr:forsterite laser at 1.25 μm [1.63] and Yb-doped bulk laser at the wavelength near 1 μm [1.64-1.66], Ti:Sapphire laser at 0.8 μm [1.67].

Table 1.1. Saturable absorption of CNTs.

Sample	**Optical Measurements**	***β* (cm/W)**	**Im$\chi^{(3)}$ (esu)**	**τ (Recovery time)**	**FOM Im$\chi^{(3)}$/(α_0*τ)**	**References**
SWNT/poly vinyl alcohol composite (HiPco tube)	1550 nm, 50 MHz, 150 fs, Pump-probe technique	N.A.	~10^{-10}	~0.8 ps	N.A.	2002 [1.57]
SWNT film (HiPco tube)	1300 nm,1 kHz, 200 fs, Z-scan	N.A.	~8.5×10^{-8}	1 ps	2.4 esu cm s^{-1}	2003 [1.58]
SWNT film (HiPco tube)	1130-2072 nm, 1 kHz, 110 fs, Z-scan	N.A.	~1.5×10^{-7} at 1300 nm	0.35 ps	6.3 esu cm s^{-1} at 1400 nm	2005 [1.13]
MWNT film (CVD)	780 nm, 1 kHz, 100 fs, Z-scan	2.9×10^{-8}	1.6×10^{-11}	2 ps	N.A.	2004 [1.56]
$AgInSe_2$ Nanorods	780 nm, 1 kHz, 200 fs, Z-scan	2.9×10^{-10}	2.2×10^{-12}	20 ps	0.04 eus cm s^{-1}	2007 [1.59]

1.2.4 Saturable absorption (SA) in graphene

Graphene, as a new member allotrope of carbon, is one-atom-thick planar sheets of sp^2 bonded carbon atoms that are densely packed in a honeycomb crystal lattice, as shown in Figure 1.8 (c). The word *graphene* was a combination of graphite and suffix –ene by Hanns-Peter Boehm, who described single-layer carbon foils in 1962. However, it was not until 2004 that individual graphene plane was isolated by using mechanical cleavage method [1.68]. Since then, the physical properties of this novel two-dimensional material have been studied intensely.

Graphene has unique and valuable electronic properties. The two-dimensional structure of graphene enables electrons to move with a linear relation between energy

and momentum, and thus behave as massless Dirac fermions [1.69] with an effective 'speed of light' of around 10^6 m s^{-1}.

Graphene also shows remarkable optical properties. For example, it can be optically visualized, despite being only a single atom thick. For a single layer graphene, its optical transmittance is 97.7%, which can be expressed in terms of the fine-structure constant [1.70]. Besides, Dirac electrons in graphene show linear dispersion which makes broadband applications possible.

Because of the unique electronic and optical properties of graphene, it has potential applications in many fields. Graphene can fulfill multiple functions in photovoltaic devices as the transparent conductor windows, photoactive material, channel for charge transport, and catalyst [1.71]. Besides, graphene is also an ideal alternative in the application of touch screens, bistable displays, and light-emitting devices [1.72]. In addition, graphene is also a good candidate in the application of photo detectors due to its much broader spectral detection compared with its traditional semiconductor counterpart [1.73].

The above mentioned optical properties of graphene correspond to the optical properties under weak light irradiance. However, when graphene is under intense laser irradiance, nonlinear optical absorption of graphene should take place.

Saturable absorption is an important nonlinear optical properties of graphene. When graphene is under laser irradiance, the electrons in lower energy states absorb the energy of photons and 'jump' to higher energy states. However, when the laser intensity is so high that most of the higher electron energy states are occupied, and

hence, further absorption is blocked, which is known as "Pauli blocking" effect. This results in saturable absorption of graphene [1.74].

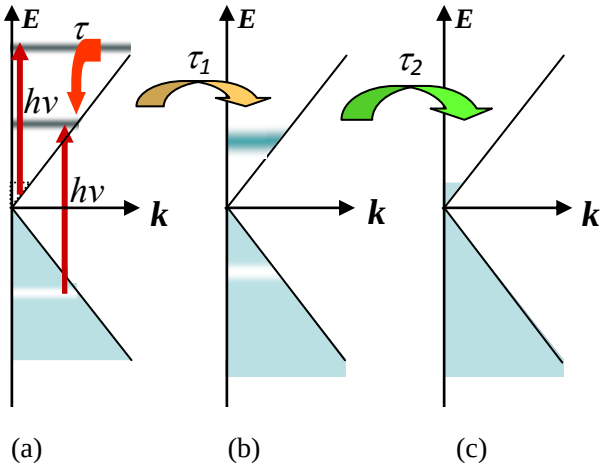

Figure 1.12. The photo-excited carrier dynamics in graphene. (a) Interband and intraband transitions of graphene under laser irradiance. (b) Due to carrier-carrier and carrier-optical phonon scattering, after a time scale of τ_1 ~100 fs, a quasi-equilibrium state with Fermi-Dirac distribution is reached. (c) Due to carrier-acoustic phonon scattering, subsequent thermalization of the carriers happens a time scale of few picoseconds. The original state of system restored.

The photo-excited carrier dynamics in graphene has been studied intensely. The first report about saturable absorption of graphene was in 2008 by the group of Cornell University. The degenerate (800 nm) pump-probe experiments were carried out to gain insights of nonlinear optical response and ultrafast carrier dynamics in epitaxial graphene [1.75]. Saturation of interband absorption of epitaxial graphene due to the band filling effect under intense laser irradiance was observed. As shown in the schematic diagram of photo-excited carrier dynamics in Figure 1.12, it was found that immediately after photo-excitation, the non-equilibrium carrier distribution broadens and also equilibrates with the intrinsic carrier population through carrier-carrier

scattering. This process is expected to be much faster than the excitation pulse duration in the experiment, thereby it was not directly revealed. With the initial carrier-carrier scattering, the photogenerated carriers are expected to equilibrate among themselves and reach a Fermi-Dirac-like distribution with a temperature much higher than the lattice temperature. The time scale for this process (τ_1) is around ~0.1 ps. The slower time constant (τ_2) of the transmittivity decay could be attributed to the subsequent thermalization of the carriers with the lattice through carrier-phonon intraband scattering.

A later study on the ultrafast carrier dynamics in a free-standing 20-30 nm thick highly oriented pyrolytic graphite using pump-probe technique with a time resolution of 10 fs at 800 nm pump was reported in 2009 [1.76]. A rapid intraband carrier equilibration within 30 fs was observed. After the rapid intraband carrier equilibration, the system develops separated electron and hole chemical potentials and reach a quasi-equilibrium state. After that, the hot quasi-equilibrium carriers loose a major fraction of their excess energy within 200 fs, mainly by emission of optical phonons. Ultrafast optical pump, terahertz [1.77-1.79] or mid-infrared [1.80, 1.81] probe spectroscopy of the carrier dynamics in epitaxial graphene was conducted to study the carrier dynamics near the Fermi-Dirac point at different ambient temperatures (10 K – 300 K). It was found that the mechanisms responsible for electron-hole recombination in graphene could include Plasmon emission, phonon emission, and Auger scattering. Besides, the ultrafast carrier kinetics in exfoliated and CVD graphene were also studied intensely [1.82-1.84]. The results are consistent with the reports of epitaxial

graphene, except a little discrepancy in carrier relaxation time scale due to the substrate effect. Recently, transient absorption microscopy was employed to measure carrier dynamics in a large spatial scale in epitaxial multilayer graphene [1.77]. This technique realized direct imaging of carrier dynamics in graphene with a diffraction-limited spatial resolution (~0.3 μm).

Due to the ultrafast saturable absorption of graphene, it has been demonstrated to be a promising material as a saturable absorber in mode-locking to generate ultrashort laser pulses. The first report about the application of graphene as a saturable absorber in mode-locking was in 2009 [1.74]. The monolayer and multilayer CVD graphene was covered on the optical fiber core and insert into the fiber laser cavity. Due to the high modulation depth and low saturation intensity of graphene, laser output with repetition rate of 1.79 MHz, pulse width of 1.17 ps, central wavelength at 1565 nm was achieved. It indicates that graphene is a promising material in generating ultrashort laser pulses at the optical communication wavelength. Subsequently, many research groups make efforts to generate ultrashort pulses in a wide spectrum range [1.86-1.92]. The research results are concluded in Table 1.2.

Table 1.2. Ultrashort pulse generation using graphene as saturable absorber.

Sample	**Output**				**References**
	Style	**Repetition Rate**	**Pulse width**	**wavelength**	
CVD Graphene	Fiber Laser	1.79 MHz	0.75 ps	1565 nm	2009 [1.74]
Exfoliated Graphene	Fiber Laser	27.4 MHz	0.17 ps	1550 nm	2010 [1.92]
Exfoliated Graphene	Fiber Laser	19.9 MHz	0.46 ps	1559 nm	2010 [1.86]
Exfoliated Graphene	Fiber Laser	6.22 MHz	0.88 ps	1566 nm	2011 [1.87]
Exfoliated Graphene	Solid-State-Laser (SSL)	N.A.	16 ps	1064 nm	2011 [1.91]

Because of saturable absorption of graphene and its application in mode-locking, many research works have been conducted on its underlying mechanism and to determine the saturation intensity. An extension of dynamic conductivity of graphene beyond linear response was reported in 2009 [1.93]. It was found that the ac conductivity of graphene should be determined by Rabi oscillations. Under strong applied electric fields, the induced current eventually saturates at a value determined by the frequency and the inverse electron lifetime. Another theoretical treatment of the saturation mechanism was conducted in 2010 [1.94]. The thresholds for saturation in transmission and absorption coefficients were measured for mid-IR and visible (or near-IR) spectral regions. Recently, the linear and nonlinear optical response of graphene were studied within a quantum-mechanical, full-band steady-state density-matrix model [1.95]. The saturable absorption of graphene has also been

studied experimentally using different experimental techniques such as optical transmittance (also called direct measurement), Z-scan and pump-probe measurements [1.86-1.96]. The saturable absorption of epitaxial graphene was studied using Z-scan technique [1.96]. The saturation intensity of graphene at 800 nm was measured to be around 4 GW/cm^2 with femtosecond laser pulses (200 fs, 1 kHz). The saturable absorption of exfoliated graphene was measured by depositing the graphene layers on a fiber core [1.87]. The nonlinear absorption was measured using femtosecond laser pulses at 1550 nm with a repetition rate of 50 MHz and pulse duration of 500 fs. The saturation intensities of the 8, 13, 30 layers of graphene samples were 90 MW/cm^2, 350 MW/cm^2, and 380 MW/cm^2, respectively. In another study, a graphene-polymer composite was fabricated using wet-chemistry technique, in which, the natural graphite was exfoliated in water without functionalization under mild sonication [1.86]. The saturation intensity of the graphene-polymer thin film was measured to be 266 MW/cm^2 at 1558 nm with a repetition rate of 38.83 MHz and pulse duration of 580 fs. A summary of the reported saturation intensities of graphene can be found in Table 4.1.

Besides the studies of saturable absorption of graphene, which corresponds to the imaginary part of the nonlinear optical susceptibility, the magnitude of third-order nonlinear optical susceptibility ($\chi^{(3)}$) of graphene has also been investigated using the four-wave-mixing (FWM) technique. It was found that the third-order nonlinear optical susceptibility of graphene is remarkably large (~1.5×10^{-7} esu ≈ 2.1×10^{-15} m^2·V^{-2}) and only weakly dependent on the wavelength in the near-infrared frequency

range [1.97]. A corresponding quantum theory of frequency mixing in graphene was also developed [1.98].

1.3 Objectives and scope of this thesis

Although saturable absorption of graphene and its application as saturable absorber in mode-locking have been studied intensely, there are a large discrepancy between the reports about saturation intensity of graphene due to the different experimental conditions [1.86-1.96]. A systematical study of the saturable absorption of graphene is desired, which should give a deep understanding of saturable absorption of graphene and facilitate graphene-based mode-locking technology.

In this thesis, we systematically studied the saturable absorption of graphene by carrying out open aperture Z-scan experiments on the monolayer, bilayer and 6-layer epitaxial graphene at 780 nm. Subsequently, we studied the spectral dependence of saturable absorption of graphene by carrying out open aperture Z-scan experiment on the bilayer graphene in a wide spectral range (900 nm-1100 nm). Finally, we compared out experimental results with the reports from other groups and the saturable of CNTs.

Besides the intense interests of the one-photon absorption properties of graphene [1.70, 1.99-1.106], two-photon absorption of graphene starts to attract research interests recently due to its potential application in a wide range of optoelectronics fields. The two-photon absorption of graphene was firstly reported in the experiment of coherent control of ballistic photocurrents in multilayer epitaxial graphene [1.107]. Coherent control of quantum interference between the one-photon and two-photon

excited electrons was demonstrated. Ballistic electric currents was generated via quantum interference between phase-controlled cross-polarized fundamental and second harmonic pulses. The injected current direction could be fully controlled by the polarization of the pump beams and do not rely on sample orientation. This all-optical injection of current provides not only a noncontact way of injecting directional current in graphene but also new insight into one- and two-photon absorption processes in epitaxial graphene.

As mentioned previously, two-photon absorption of graphene has been observed and its application in the generation of ballistic electric currents in graphene has been developed experimentally. However, a theoretical and experimental systematic study of the two-photon absorption is desired for a better understanding of the nonlinear optical absorption of graphene under intense irradiance.

In this thesis, the magnitude and spectral dependence of two-photon absorption of monolayer and bilayer graphene were measured by pump-probe and Z-scan techniques. Two-photon absorption property of monolayer and bilayer graphene were also studied theoretically by the quantum perturbation theory in a wide spectral range. The experimental results were compared with the theoretical simulations.

The systematical study of two-photon absorption should give an additional understanding of the nonlinear optical absorption properties of graphene. The measurement of two-photon absorption in graphene could facilitate the injection of ballistic electrical current by quantum interference between one-photon and two-photon absorption pathways. Besides, the application of quantum perturbation

theory in the calculation of the two-photon absorption coefficient of graphene has significant scientific implications to optical technology.

The thesis is organized as follows: Chapter 2 presents the syntheses and characterization of graphene samples used in our research. Chapter 3 describes the experimental techniques and operational principles that are employed to determine the nonlinear optical absorption of graphene. Chapter 4 documents saturable absorption of graphene and its spectral dependence by carrying out Z-scan experiments on epitaxial graphene samples. Chapter 5 details the measurements of two-photon absorption in graphene using pump-probe and Z-scan techniques, and the theoretical calculation of two-photon absorption coefficient using the second-order quantum perturbation theory. The final chapter, Chapter 6, summarizes the important findings reported in this thesis and suggests future research directions.

References

[1.1] P. A. Franken, A. E. Hill, C. W. Peters *et al.*, "Generation of optical harmonics," Phys. Rev. Lett., **7,** 118-119 (1961).

[1.2] P. N. Butcher, D.Cotter, "The elements of nonlinear optics, " Cambridge University Press (1990).

[1.3] R. L. Sutherland, D. G. Mclean, S. Kirkpatrick, "Handbook of nonlinear optics,"Marcel Dekker: New York (2003).

[1.4] D. A. B. Miller, C. T. Seaton, M. E. Prise *et al.*, "Band-gap—resonant nonlinear refraction in III-V semiconductors," Phys. Rev. Lett., **47,** 197-200 (1981).

[1.5] C. Noguez, "Surface plasmons on metal nanoparticles: The influence of shape and physical environment," J. Phys. Chem. C, **111,** 3806-3819 (2007).

[1.6] X. H. Huang, S. Neretina, and M. A. El-Sayed, "Gold nanorods: From synthesis and properties to biological and biomedical applications," Adv. Mater., **21,** 4880-4910 (2009).

[1.7] K. S. Lee, and M. A. El-Sayed, "Gold and silver nanoparticles in sensing and imaging: Sensitivity of plasmon response to size, shape, and metal composition," J. Phys. Chem. B, **110,** 19220-19225 (2006).

[1.8] M. Perner, P. Bost, U. Lemmer *et al.*, "Optically induced damping of the surface plasmon resonance in gold colloids," Phys. Rev. Lett., **78,** 2192-2195 (1997).

[1.9] E. J. Blackie, E. C. L. Ru, and P. G. Etchegoin, "Single-molecule

surface-enhanced Raman spectroscopy of nonresonant molecules," J. Am. Chem. Soc., **131,** 14466-14472 (2009).

[1.10] E. C. Le Ru, E. Blackie, M. Meyer *et al.*, "Surface enhanced Raman scattering enhancement factors: A comprehensive study," J. Phys. Chem. C, **111,** 13794-13803 (2007).

[1.11] G. A. Swartzlander, H. Yin *et al.*, "Continuous-wave self-deflection effect in sodium vapor, " J. Opt. Soc. Am. B, **6,** 1317-1325 (1989).

[1.12] H. I. Elim, J. Yang, J.-Y. Lee *et al.*, "Observation of saturable and reverse-saturable absorption at longitudinal surface plasmon resonance in gold nanorods," Appl. Phys. Lett., **88,** 083107-3 (2006).

[1.13] A. Maeda, S. Matsumoto, H. Kishida *et al.*, "Large optical nonlinearity of semiconducting single-walled Carbon nanotubes under resonant excitations," Phys. Rev. Lett., **94,** 047404 (2005).

[1.14] E. P. Ippen, D. J. Eilenberger, and R. W. Dixon, "Picosecond pulse generation by passive mode-locking of diode-lasers," Appl. Phys. Lett., **37,** 267-271 (1980).

[1.15] Y. Silberberg, P. W. Smith, D. J. Eilenberger *et al.*, "Passive mode-locking of a semiconductor diode-laser," Opt. Lett., **9,** 507-509 (1984).

[1.16] J. P. Vanderziel, "Active mode-locking of double heterostructure lasers in an external cavity," J. Appl. Phys., **52,** 4435-4446 (1981).

[1.17] U. Keller, D. A. B. Miller, G. D. Boyd *et al.*, "Solid-state low-loss intracavity saturable absorber for Nd-YLF lasers - An antiresonant semiconductor

Fabery-Perot saturable absorber," Opt. Lett., **17,** 505-507 (1992).

[1.18] U. Keller, "Recent developments in compact ultrafast lasers," Nature, **424,** 831-838 (2003).

[1.19] M. Joschko, P. Langlois, E. R. Thoen *et al.*, "Ultrafast hot-carrier dynamics in semiconductor saturable absorber mirrors," Appl. Phys. Lett., **76,** 1383-1385 (2000).

[1.20] E. R. Thoen, E. M. Koontz, M. Joschko *et al.*, "Two-photon absorption in semiconductor saturable absorber mirrors," Appl. Phys. Lett., **74,** 3927-3929 (1999).

[1.21] M. Göppert-Mayer, "Über elementarakte mit zwei quantensprüngen," Annalen der Physik, **401,** 273-294 (1931).

[1.22] W. Kaiser, and C. G. B. Garrett, "Two-photon excitation in CaF_2: Eu^{2+}," Phys. Rev. Lett., **7,** 229-231 (1961).

[1.23] I. D. Abella, "Optical double-photon absorption in Cesium vapor," Phys. Rev. Lett., **9,** 453-455 (1962).

[1.24] V. Nathan, A. H. Guenther, and S. S. Mitra, "Review of multiphoton absorption in crystalline solids," J. Opt. Soc. Am. B: Opt. Phys., **2,** 294-316 (1985).

[1.25] D. C. Hutchings, and E. W. V. Stryland, "Nondegenerate two-photon absorption in zinc blende semiconductors," J. Opt. Soc. Am. B, **9,** 2065-2074 (1992).

[1.26] X. B. Feng, Y. L. Ang, J. He *et al.*, "Three-photon absorption in

semiconductor quantum dots: experiment," Opt. Express, **16,** 6999-7005 (2008).

[1.27] V. I. Bredikhin, M. D. Galanin, and N. G. Vladimir, "Two-photon absorption and spectroscopy," Soviet Physics Uspekhi, **16,** 299 (1973).

[1.28] H. Mahr. in Quantum Electronics, H.Rabin and C.L.Tang, eds. (Academic, New York, 1975), Vol. 1, Part A, p.285.

[1.29] M. Sheik-Bahae, A. A. Said, *et al.*, "Sensitive measurement of optical nonlinearities using a single beam," Quantum Electronics, IEEE Journal of **26,** 760-769 (1990).

[1.30] J. He, Y. L. Qu, H. P. Li *et al.*, "Three-photon absorption in ZnO and ZnS crystals," Opt. Express, **13,** 9235-9247 (2005).

[1.31] W. Denk, J. Strickler, and W. Webb, "Two-photon laser scanning fluorescence microscopy," Science, **248,** 73-76 (1990).

[1.32] R. Carriles, D. N. Schafer, K. E. Sheetz *et al.*, "Invited Review Article: Imaging techniques for harmonic and multiphoton absorption fluorescence microscopy," Rev. Sci. Instrum., **80,** 081101 (2009).

[1.33] W. Denk, and K. Svoboda, "Photon upmanship: Why multiphoton imaging is more than a gimmick," Neuron, **18,** 351-357 (1997).

[1.34] G. S. He, G. C. Xu, P. N. Prasad *et al.*, "2-photon absorption and optical-limiting properties of novel organic-compounds," Opt. Lett., **20,** 435-437 (1995).

[1.35] E. Osawa, Kagaku **25,** 854 (1970).

[1.36] H. W. Kroto, J. R. Heath, S. C. Obrien *et al.*, "C_{60} - buckminsterfullerene," Nature, **318,** 162-163 (1985).

[1.37] W. Kratschmer, L. D. Lamb, K. Fostiropoulos *et al.*, "Solid C_{60} - A new form of Carbon," Nature, **347,** 354-358 (1990).

[1.38] R. E. Haufler, J. Conceicao, L. P. F. Chibante *et al.*, "Efficient production of C_{60} (buckminsterfullerene), $C_{60}H_{36}$, and the solvated buckide ion," J. Phys. Chem., **94,** 8634-8636 (1990).

[1.39] C. C. Wu, T. M. Liu, T. Y. Wei *et al.*, "Kramers-Kronig relation between nonlinear absorption and refraction of C_{60} and C_{70}," Opt. Express, **18,** 22637-22650 (2010).

[1.40] B. L. Yu, H. P. Xia, C. S. Zhu *et al.*, "Enhanced third-order nonlinear optical properties of C_{60}-silane compounds," Appl. Phys. Lett., **81,** 2701-2703 (2002).

[1.41] D. Vincent, and J. Cruickshank, "Optical limiting with C_{60} and other fullerenes," Appl. Opt., **36,** 7794-7798 (1997).

[1.42] X. H. Ouyang, H. P. Zeng, and W. Ji, "Synthesis, Strong Two-Photon Absorption, and Optical Limiting Properties of Novel C_{70}/C_{60} Derivatives Containing Various Carbazole Units," J. Phys. Chem. B, **113,** 14565-14573 (2009).

[1.43] M. P. Joshi, S. R. Mishra, H. S. Rawat *et al.*, "Investigation of optical limiting in C_{60} solution," Appl. Phys. Lett., **62,** 1763-1765 (1993).

[1.44] G. B. Talapatra, N. Manickam, M. Samoc *et al.*, "Nonlinear optical properties

of the fullerene (C_{60}) molecule: theoretical and experimental studies," J. Phys. Chem., **96,** 5206-5208 (1992).

[1.45] C. Li, L. Zhang, R. Wang *et al.*, "Dynamics of reverse saturable absorption and all-optical switching in C_{60}," J. Opt. Soc. Am. B, **11,** 1356-1360 (1994).

[1.46] G. Banfi, D. Fortusini, M. Bellini *et al.*, "Wave-dispersed two-photon absorption of C_{60}," Phys. Rev. B, **56,** R10075-R10078 (1997).

[1.47] S. Iijima, "Helical microtubules of graphitic carbon," Nature, **354,** 56-58 (1991).

[1.48] T. W. Ebbesen, and P. M. Ajayan, "Large-scale synthesis of carbon nanotubes," Nature, **358,** 220-222 (1992).

[1.49] D. M. Guldi, and N. Martin, "Carbon nanotubes and related structures:sytehsis,characterization functionalization, and applications," Wiley-VCH, (c2010).

[1.50] H. Kataura, Y. Kumazawa, Y. Maniwa *et al.*, "Optical properties of single-wall carbon nanotubes," Synth. Met., **103,** 2555-2558 (1999).

[1.51] M. Zheng, A. Jagota, M. S. Strano *et al.*, "Structure-based carbon nanotube sorting by sequence-dependent DNA assembly," Science, **302,** 1545-1548 (2003).

[1.52] M. S. Arnold, A. A. Green, J. F. Hulvat *et al.*, "Sorting carbon nanotubes by electronic structure using density differentiation," Nature Nanotech., **1,** 60-65 (2006).

[1.53] http://www.photon.t.u-tokyo.ac.jp/~maruyama/kataura/kataura.html.

[1.54] J. S. Lauret, C. Voisin, G. Cassabois *et al.*, "Ultrafast carrier dynamics in single-wall carbon nanotubes," Phys. Rev. Lett., **90,** 057404 (2003).

[1.55] G. N. Ostojic, S. Zaric, J. Kono *et al.*, "Interband recombination dynamics in resonantly excited single-walled carbon nanotubes," Phys. Rev. Lett., **92,** 117402 (2004).

[1.56] H. I. Elim, W. Ji, G. H. Ma *et al.*, "Ultrafast absorptive and refractive nonlinearities in multiwalled carbon nanotube films," Appl. Phys. Lett., **85,** 1799-1801 (2004).

[1.57] Y. C. Chen, N. R. Raravikar, L. S. Schadler *et al.*, "Ultrafast optical switching properties of single-wall carbon nanotube polymer composites at 1.55 μm," Appl. Phys. Lett., **81,** 975-977 (2002).

[1.58] S. Tatsuura, M. Furuki, Y. Sato *et al.*, "Semiconductor carbon nanotubes as ultrafast switching materials for optical telecommunications," Adv. Mater., **15,** 534-537 (2003).

[1.59] H. I. Elim, W. Ji, M. T. Ng *et al.*, "$AgInSe_2$ nanorods: A semiconducting material for saturable absorber," Appl. Phys. Lett., **90,** 033106 (2007).

[1.60] V. G. Savitski, A. M. Malyarevich, M. I. Demchuk *et al.*, "Intensity-dependent bleaching relaxation in lead salt quantum dots," J. Opt. Soc. Am. B, **22,** 1660-1666 (2005).

[1.61] T. Schibli, K. Minoshima, H. Kataura *et al.*, "Ultrashort pulse-generation by saturable absorber mirrors based on polymer-embedded carbon nanotubes," Opt. Express, **13,** 8025-8031 (2005).

[1.62] K. H. Fong, K. Kikuchi, C. S. Goh *et al.*, "Solid-state Er:Yb:glass laser mode-locked by using single-wall carbon nanotube thin film," Opt. Lett., **32,** 38-40 (2007).

[1.63] W. B. Cho, J. H. Yim, S. Y. Choi *et al.*, "Mode-locked self-starting Cr:forsterite laser using a single-walled carbon nanotube saturable absorber," Opt. Lett., **33,** 2449-2451 (2008).

[1.64] T. R. Schibli, K. Minoshima, H. Kataura *et al.*, "Ultrashort pulse-generation by saturable absorber mirrors based on polymer-embedded carbon nanotubes," Opt. Express, **13,** 8025-8031 (2005).

[1.65] K. H. Fong, K. Kikuchi, C. S. Goh *et al.*, "Solid-state Er : Yb : glass laser mode-locked by using single-wall carbon nanotube thin film," Opt. Lett., **32,** 38-40 (2007).

[1.66] J. H. Yim, W. B. Cho, S. Lee *et al.*, "Fabrication and characterization of ultrafast carbon nanotube saturable absorbers for solid-state laser mode locking near 1 mu m," Appl. Phys. Lett., **93,** 161106 (2008).

[1.67] D. V. Khudyakov, A. S. Lobach, and V. A. Nadtochenko, "Passive mode locking in a Ti:sapphire laser using a single-walled carbon nanotube saturable absorber at a wavelength of 810 nm," Opt. Lett., **35,** 2675-2677 (2010).

[1.68] K. S. Novoselov, A. K. Geim, S. V. Morozov *et al.*, "Electric field effect in atomically thin carbon films," Science, **306,** 666-669 (2004).

[1.69] Y. Zhang, Y.-W. Tan, H. L. Stormer *et al.*, "Experimental observation of the quantum Hall effect and Berry's phase in graphene," Nature, **438,** 201-204

(2005).

[1.70] R. R. Nair, P. Blake, A. N. Grigorenko *et al.*, "Fine structure constant defines visual transparency of graphene," Science, **320,** 1308 (2008).

[1.71] X. Wang, L. Zhi, N. Tsao *et al.*, "Transparent carbon films as electrodes in organic solar cells," Angewandte Chemie International Edition, **47,** 2990-2992 (2008).

[1.72] J. Wu, M. Agrawal, H. c. A. Becerril *et al.*, "Organic light-emitting diodes on solution-processed graphene transparent electrodes," ACS Nano, **4,** 43-48 (2009).

[1.73] F. Xia, T. Mueller, Y. M. Lin *et al.*, "Ultrafast graphene photodetector," Nature Nanotech., **4,** 839-843 (2009).

[1.74] Q. Bao, H. Zhang, Y. Wang *et al.*, "Atomic-layer graphene as a saturable absorber for ultrafast pulsed lasers," Adv. Funct. Mater., **19,** 3077-3083 (2009).

[1.75] J. M. Dawlaty, S. Shivaraman, M. Chandrashekhar *et al.*, "Measurement of ultrafast carrier dynamics in epitaxial graphene," Appl. Phys. Lett., **92,** (2008).

[1.76] M. Breusing, C. Ropers, and T. Elsaesser, "Ultrafast carrier dynamics in graphite," Phys. Rev. Lett., **102,** 086809 (2009).

[1.77] P. A. George, J. Strait, J. Dawlaty *et al.*, "Ultrafast optical-pump terahertz-probe spectroscopy of the carrier relaxation and recombination dynamics in epitaxial graphene," Nano Lett., **8,** 4248-4251 (2008).

[1.78] J. H. Strait, H. Wang, S. Shivaraman *et al.*, "Very slow cooling dynamics of photoexcited carriers in graphene observed by optical-pump terahertz-probe spectroscopy," Nano Lett., **11,** 4902-4906 (2011).

[1.79] H. Choi, F. Borondics, D. A. Siegel *et al.*, "Broadband electromagnetic response and ultrafast dynamics of few-layer epitaxial graphene," Appl. Phys. Lett., **94,** 172102 (2009).

[1.80] D. Sun, Z.-K. Wu, C. Divin *et al.*, "Ultrafast relaxation of excited dirac fermions in epitaxial graphene using optical differential transmission spectroscopy," Phys. Rev. Lett., **101,** 157402 (2008).

[1.81] D. Sun, C. Divin, C. Berger *et al.*, "Spectroscopic measurement of interlayer screening in multilayer epitaxial graphene," Phys. Rev. Lett., **104,** 136802 (2010).

[1.82] R. W. Newson, J. Dean, B. Schmidt *et al.*, "Ultrafast carrier kinetics in exfoliated graphene and thin graphite films," Opt. Express, **17,** 2326-2333 (2009).

[1.83] P. A. Obraztsov, M. G. Rybin, A. V. Tyurnina *et al.*, "Broadband light-induced absorbance change in multilayer graphene," Nano Lett., **11,** 1540-1545 (2011).

[1.84] J. Shang, T. Yu, J. Lin *et al.*, "Ultrafast electron−optical phonon scattering and quasiparticle lifetime in CVD-grown graphene," ACS Nano, **5,** 3278-3283 (2011).

[1.85] L. Huang, G. V. Hartland, L. Q. Chu *et al.*, "Ultrafast transient absorption

microscopy studies of carrier dynamics in epitaxial graphene," Nano Lett., **10,** 1308-1313 (2010).

[1.86] Z. Sun, T. Hasan, F. Torrisi *et al.*, "Graphene mode-locked ultrafast laser," ACS Nano, **4,** 803-810 (2010).

[1.87] A. Martinez, K. Fuse, and S. Yamashita, "Mechanical exfoliation of graphene for the passive mode-locking of fiber lasers," Appl. Phys. Lett., **99,** 121107 (2011).

[1.88] A. Martinez, K. Fuse, B. Xu *et al.*, "Optical deposition of graphene and carbon nanotubes in a fiber ferrule for passive modelocked lasing," Opt. Express, **18,** 23054-23061 (2010).

[1.89] H. Kim, J. Cho, S. Y. Jang *et al.*, "Deformation-immunized optical deposition of graphene for ultrafast pulsed lasers," Appl. Phys. Lett., **98,** 021104 (2011).

[1.90] Y. W. Song, S. Y. Jang, W. S. Han *et al.*, "Graphene mode-lockers for fiber lasers functioned with evanescent field interaction," Appl. Phys. Lett., **96,** 051122 (2010).

[1.91] J. L. Xu, X. L. Li, Y. Z. Wu *et al.*, "Graphene saturable absorber mirror for ultra-fast-pulse solid-state laser," Opt. Lett., **36,** 1948-1950 (2011).

[1.92] D. Popa, Z. Sun, F. Torrisi *et al.*, "Sub 200 fs pulse generation from a graphene mode-locked fiber laser," Appl. Phys. Lett., **97,** 203106 (2010).

[1.93] E. G. Mishchenko, "Dynamic conductivity in graphene beyond linear response," Phys. Rev. Lett., **103,** 246802 (2009).

[1.94] F. T. Vasko, "Saturation of interband absorption in graphene," Phys. Rev. B,

82, 245422 (2010).

[1.95] Z. Zhang, and P. L. Voss, "Full-band quantum-dynamical theory of saturation and four-wave mixing in graphene," Opt. Lett., **36,** 4569-4571 (2011).

[1.96] G. C. Xing, H. C. Guo, X. H. Zhang *et al.*, "The Physics of ultrafast saturable absorption in graphene," Opt. Express, **18,** 4564-4573 (2010).

[1.97] E. Hendry, P. J. Hale, J. Moger *et al.*, "Coherent nonlinear optical response of graphene," Phys. Rev. Lett., **105,** 097401 (2010).

[1.98] S. A. Mikhailov, "Theory of the nonlinear optical frequency mixing effect in graphene," Physica E: Low-dimensional Systems and Nanostructures, **44,** 924-927 (2012).

[1.99] F. T. Vasko, and V. Ryzhii, "Photoconductivity of intrinsic graphene," Phys. Rev. B, **77,** 195433 (2008).

[1.100] K. F. Mak, M. Y. Sfeir, Y. Wu *et al.*, "Measurement of the optical conductivity of graphene," Phys. Rev. Lett., **101,** 196405 (2008).

[1.101] D. S. L. Abergel, and V. I. Fal'ko, "Optical and magneto-optical far-infrared properties of bilayer graphene," Phys. Rev. B, **75,** 155430 (2007).

[1.102] Y. Wang, Z. Ni, L. Liu *et al.*, "Stacking-dependent optical conductivity of bilayer graphene," ACS Nano, **4,** 4074-4080 (2010).

[1.103] L. Hao, and L. Sheng, "Optical conductivity of multilayer graphene," Solid State Commun., **149,** 1962-1966 (2009).

[1.104] E. McCann, D. S. L. Abergel, and V. I. Fal'ko, "Electrons in bilayer graphene," Solid State Commun., **143,** 110-115 (2007).

[1.105] T. Stauber, N. M. R. Peres, and A. K. Geim, "Optical conductivity of graphene in the visible region of the spectrum," Phys. Rev. B, **78,** 085432 (2008).

[1.106] A. B. Kuzmenko, E. van Heumen, F. Carbone *et al.*, "Universal optical conductance of graphite," Phys. Rev. Lett., **100,** 117401 (2008).

[1.107] D. Sun, C. Divin, J. Rioux *et al.*, "Coherent control of ballistic photocurrents in multilayer epitaxial graphene using quantum interference," Nano Lett., **10,** 1293-1296 (2010).

Chapter 2

Characterization of epitaxial graphene samples

2.1 Synthesis of graphene samples

2.1.1 Introduction

Graphene is an allotrope of carbon, whose structure is one-atom-thick planar sheets of sp^2-bonded carbon atoms that are densely packed in a honeycomb crystal lattice. For a long time in history, it was believed that single carbon atom layer is thermodynamically unstable in the nature. In 2004, graphene layers was obtained via micromechanical cleaving (exfoliation) of bulk graphite followed by careful selection of monolayers by using optical, atomic force or scanning electron microscopes. In the following years, the methods of synthesizing graphene samples and the properties of the synthesized graphene samples have been studied intensely. The main methods include: micromechanical exfoliation of graphene from highly oriented pyrolytic graphite (HOPG) [2.1-2.7], reduction of graphene oxide [2.8, 2.9], exfoliation of graphite powder in solvents under ultrasonication [2.10-2.13], chemical vapor deposition of graphene on metal substrates (CVD) [2.14-2.19], and epitaxial growth of graphene on the SiC substrate [2.20-2.29].

The graphene samples prepared by micromechanical exfoliation of HOPG possess the highest quality. As the graphite crystals are repeatedly split to get increasingly thinner pieces of graphene flakes. The tap with attached optically transparent flakes was dissolved in acetone, and after a few further steps, the graphene flakes including

monolayers were sedimented on a silicon wafer. Individual atomic planes were then hunted in an optical microscope. In the process, the atomic structure and interlayer stacking sequence were preserved. Due to the high quality of graphene samples synthesized by this method, many important properties of graphene have been discovered. The room-temperature mobility of the exfoliated graphene was measured to be ~10,000 $cm^2 \cdot V^{-1} s^{-1}$ by applying gate voltage, which is the highest among graphene samples synthesized with different methods [2.1]. Room temperature quantum Hall effect was firstly observed in exfoliated graphene [2.2]. The opacity of freestanding exfoliated graphene was measured and found that it was defined solely by the fine structure constant $\alpha = e^2/\hbar c \approx 1/137$ [2.3]. The optical conductivity of graphene was studied by measuring the optical absorption of exfoliated graphene [2.4]. Gate tunable infrared phonon anomalies were observed in exfoliated bilayer graphene [2.5]. The stacking-dependent optical conductivity of exfoliated bilayer graphene was studied by measuring the transmittance spectroscopy using an optical microscopy system [2.6]. The third-order nonlinear susceptibility of graphene was measured by carrying out Four-Wave-Mixing (FWM) experiment on the expoliated graphene with a microscope system [2.7]. However, even though this technique results in relatively high quality films, it might not be suitable for large scale production. The normal size of exfoliated graphene was reported to be few tens of micrometers in lateral dimension [2.1].

Another method of synthesizing graphene productively is by reducing exfoliated graphene oxide. Graphite oxide exfoliation can be achieved by rapid heating and

yields highly dispersed carbon powder with a few percent of graphene flakes [2.8, 2.9]. Reduction of graphite oxide monolayer films e.g. by hydrazine, annealing in argon/hydrogen was reported to yield graphene films. However, the quality of graphene produced by graphite oxide reduction is lower compared to e.g. scotch-tape graphene due to incomplete removal of various functional groups by existing reduction methods.

In order to eliminate degradation of electronic mobility by the oxidation and reduction process, the technique of exfoliating powdered graphite to produce graphene in the liquid phase was developed [2.10-2.13]. This method relies on the exfoliation and stabilization of graphene using special solvents or surfactants under sonication. After tens or hundreds hours of sonication, the number of layers of graphene flakes can be down to less than 5. The size of graphene synthesized by this method was around few micrometers due to long time of sonication. It was reported that graphene concentration can be increased to around 1 mg $\cdot$mL^{-1} in the solvent N-methyl-pyrrolidone (NMP) after 460 hour of mild sonication [2.10].

Chemical vapor deposition (CVD) is an attractive approach to large-scale graphene production due to its capability of producing large area deposition and the lack of intense mechanical and chemical treatment [2.14]. In this method, a wafer with a thin transition metal film is used as catalyst, such as Ni (111), Ir (111), and Ru (0001). The substrate with metal catalyst is put in a heated furnace and is attached to a gas delivery system, which flows a gaseous carbon source downstream to the metalized wafer. Carbon atoms are then adsorbed onto the metal surface at high

temperatures, where they are precipitated out in the lowest free energy state (graphene) during cooling down to room temperature. Electrical devices based on CVD graphene with large area scale CVD graphene have been demonstrated [2.15]. However, rippling and doping of discrete regions of the graphene lattice is a consequence of the one-atom-thick 2D nature of this material [2.17]. The low temperature electronic mobility of CVD graphene was 3,700 $cm^2 \cdot V^{-1} s^{-1}$, which was the highest reported value so far [2.15], but is still considerably lower than the mobility reported for exfoliated graphene.

Recently, epitaxial growth of graphene by thermal decomposition of SiC surface at high temperatures has been demonstrated [2.20-2.23]. This technique can provide anywhere from a few monolayers of graphene to several (> 50) layers on the surface of a SiC wafer. Graphene layers grown by this technique have demonstrated low temperature carrier mobility in the tens of thousands $cm^2 \cdot V^{-1} s^{-1}$ range and do not significantly depend on temperature [2.24], which is comparable to the exfoliated graphene. Many important graphene properties have been identified in graphene produced by this method. The electronic band-structure (so called Dirac cone structure) has been first visualized in epitaxial graphene [2.25]. Weak anti-localization was observed in epitaxial graphene [2.26]. The first experiment of coherent control of ballistic photocurrents in multilayer epitaxial graphene using quantum interference between different absorption pathways was realized in 2010 [2.27]. The photo-excited carrier dynamics in epitaxial graphene has been studied intensely [2.28, 2.29]. As epitaxial graphene is in large scale with high electronic mobility, it is believed to be a

promising method of synthesizing graphene for real applications.

A comparison of the basic physical properties of graphene synthesized with different methods is shown in Table 2.1. By this comparison, it is conclusive that graphene made by epitaxial method exhibits high-quality physical properties on a large physical scale. This is why epitaxial graphene was chosen for the research presented in the thesis. In the following sections, an epitaxial method employed in the research and sample characterizations are detailed.

Table 2.1. Comparison of graphene with different synthesis methods.

Synthesis method	Dimension (Length)	Number of layer	Mobility ($cm^2 \cdot V^{-1} s^{-1}$)	Substrate	References
Exfoliation from HOPG	~Tens of μm	Monolayer, bilayer and multilayer	~10,000 (at 300K)	SiO_2/Si … (transferrable)	[2.1]
Epitaxial Method	~cm	Monolayer to few tens of layers	~10,000 (at 300K)	C face of SiC	[2.24]
CVD	~cm	Monolayer to <10 layers	~3,700 (at low temperature)	SiO_2/Si … (transferrable)	[2.15]
Reduced from GO	~Tens of μm	>= monolayer	~400 (at 300K)	Graphene flakes can be spin coated on arbitrary substrates	[2.9]
Exfoliation of graphite powder in solvents with ultrasonic treatment	~1 μm	>=monolayer	~400 (at 300K)	Graphene flakes can be spin coated on arbitrary substrates	[2.11]

2.1.2 Synthesis of epitaxial graphene on SiC single crystal

The epitaxial graphene samples on the C-face (000-1) of 4H-SiC wafers (CREE Research Inc.) was grown at temperature ~1100 ℃ in ultrahigh vacuum condition with pressure of 2×10^{-9} Torr or better. High temperature annealing of SiC led to the decomposition of SiC followed by the desorption of Si from the surface and an accumulation of carbon atoms to form a carbon-rich surface layer, on top of which, monolayer, bilayer or multilayer graphene was formed, depending on time and other conditions [2.30-2.32]. An *in-situ* scanning tunneling microscopy (STM) was combined in the ultrahigh vacuum (UHV) system to detect the surface atomic structures. The experimental facilities of the UHV and STM are shown in Figure 2.1.

The 4H-SiC single crystal which is cut along the c-axis has one face terminated with dangling carbon bonds (carbon face) and another face terminated with dangling silicon bonds (silicon face) [2.33]. The atomic structure of SiC single crystal is shown in Figure 2.2(a). Graphene can be grown on the Si face and C face of SiC substrate. The electron mobility of graphene grown on Si face of SiC was measured to be 1100 cm^2/V-s at 4K [2.34], which is relatively lower than the graphene on C face of SiC (exceeds 10,000 $cm^2 \cdot V^{-1} s^{-1}$). The *ab initio* study showed that the epitaxial graphene on the Si-face of SiC substrate could be heavily n-type doped, while epitaxial graphene on the C-face of SiC substrate was only slightly doped [2.35, 2.36]. The atomic structure of the epitaxial graphene grown on the C-face of SiC wafers are shown in Figure 2.2 (b). Figure 2.2 (c-e) shows the AB (Bernal) stacked bilayer graphene and the interlayer interactions. The stacking consequence of the graphene

samples will be discussed in detail in the following.

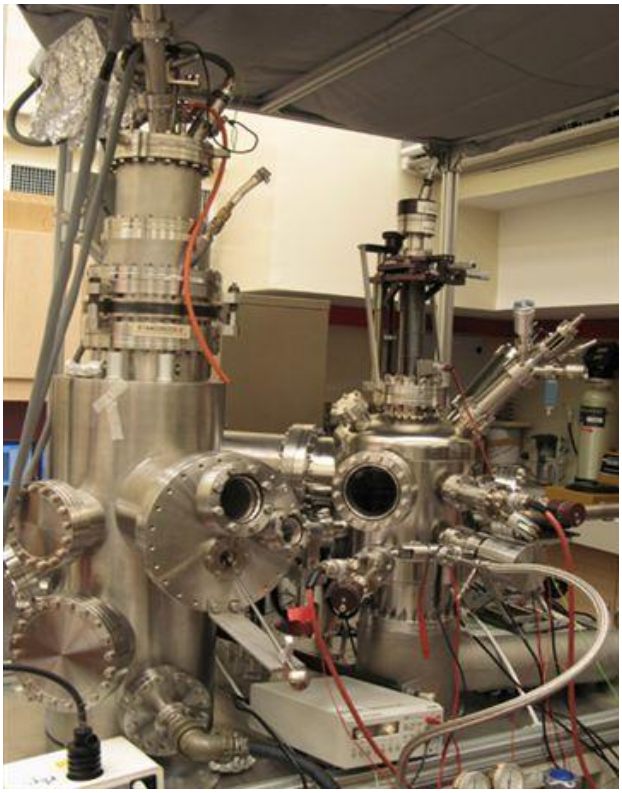

Figure 2.1. Photograph of UHV and *in-situ* STM facilities for growth and characterization of the graphene samples.

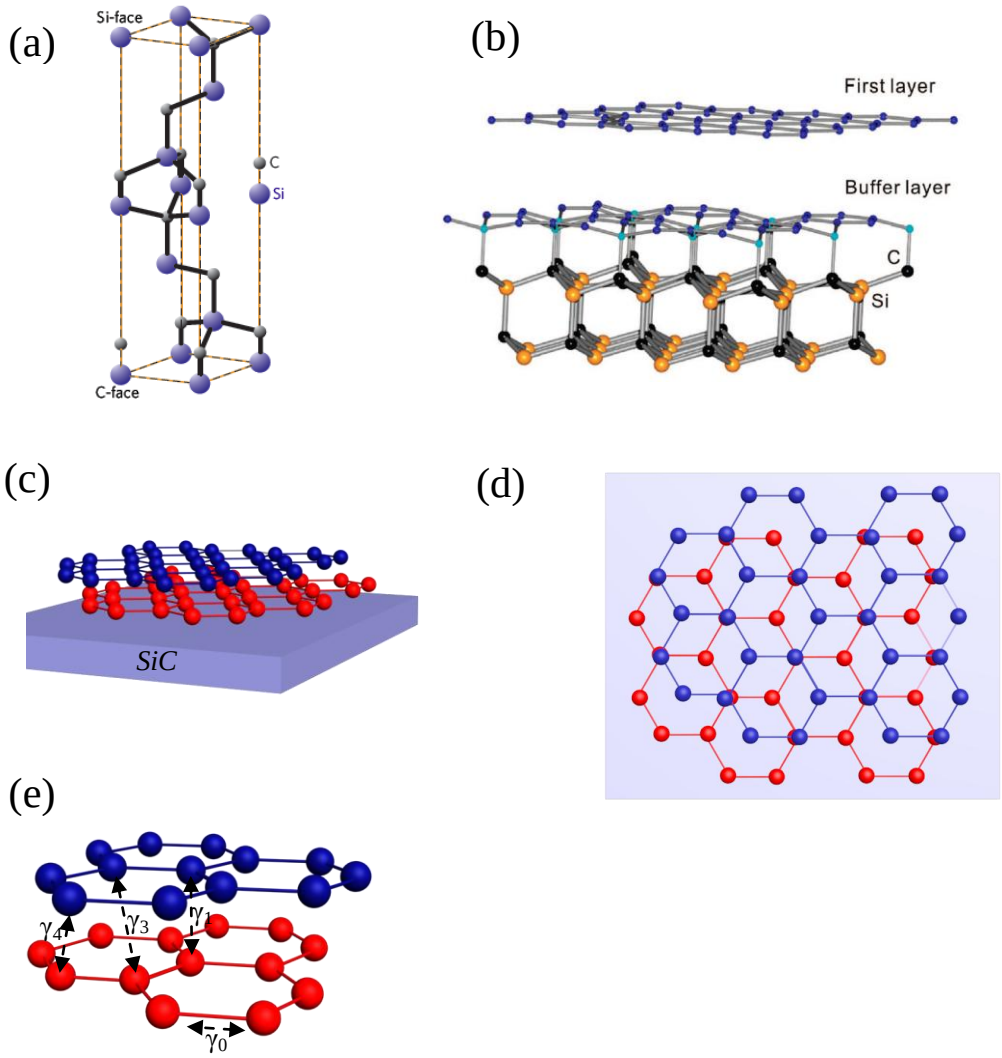

Figure 2.2. (a) The atomic structure of SiC single crystal [2.33]. (b) The atomic structure of monolayer epitaxial graphene on the C-face of SiC [2.36]. (c) The sketch of atomic structure of AB stacked bilayer graphene on SiC. (d) The top view of AB stacked bilayer graphene. (e) The side view of AB stacked bilayer graphene and the interlayer interaction [2.37].

2.2 Characterization of the epitaxial graphene samples with STM

2.2.1 Introduction

The graphene samples used in the research in this thesis include monolayer, bilayer and 6-layer epitaxial graphene samples on C face of 4H-SiC substrate. The photo and sketch of the physical structure of the samples are shown in Figure 2.3. Due to the growing condition (1100 ℃), only a carbon rich layer was formed on the opposite face of SiC (Si-face) [2.30]. The Raman spectra did not show any graphene features on this face, and the carbon rich layer was found to make no contribution to the nonlinear signal, as demonstrated by the pump-probe experiment in the following chapters.

(a)

(b)

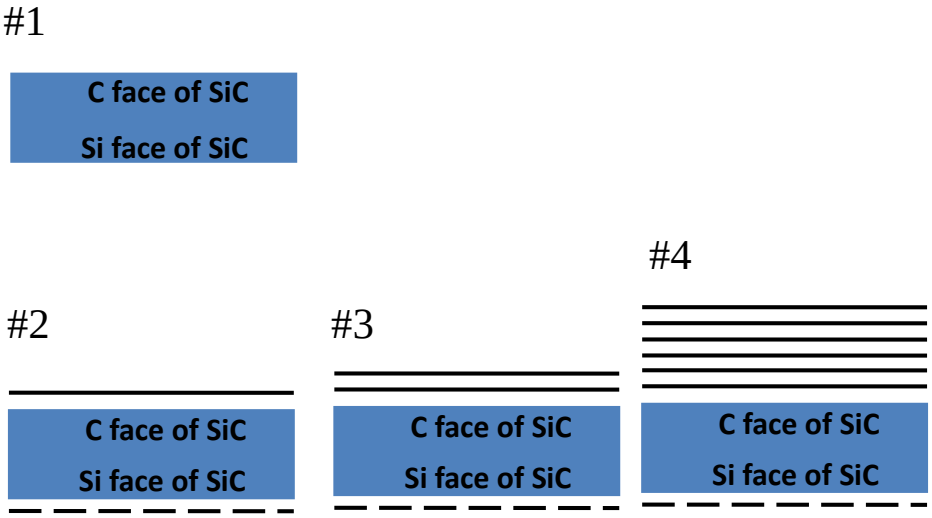

(c)

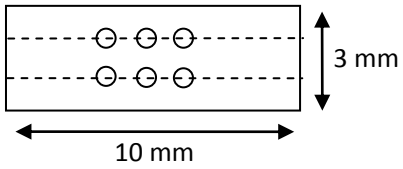

Figure 2.3. (a) Photograph of the epitaxial graphene samples on SiC substrate. (b) Sketch of the epitaxial graphene samples on SiC substrate. (c) Sketch of the position where the optical characterization carried out.

In this thesis, the physical properties of epitaxial graphene samples, such as number of layers, density of defect states, stacking consequence between layers and homogeneity, were characterized by experimental techniques: namely, (i) Scanning Tunneling Microscopy (STM), (ii) Raman Spectroscopy, and (iii) Optical Absorption Spectroscopy.

2.2.2 Scanning Tunneling Microscopy

Scanning Tunneling Microscopy (STM) is an instrument for imaging surfaces at the atomic level. For a STM, good resolution is considered to be 0.1 nm lateral resolution and 0.01 nm depth resolution. With this resolution, individual atoms within materials are routinely imaged and manipulated. The STM can be used not only in ultra-high vacuum but also in air, water, and various other liquid or gas ambient, and the temperatures ranging from near zero Kelvin to a few hundred degrees Celsius. As shown in Figure 2.4, the STM is based on the concept of quantum tunneling. When a conducting tip is brought very near to the surface to be examined, a bias (voltage difference) applied between the two can allow electrons to tunnel through the vacuum between them. The resulting tunneling current is a function of tip position, applied voltage, and the local density of states of the sample. Information is acquired by monitoring the current as the tip's position scans across the surface, and is usually displayed in a two dimensional form of imaging. STM can be a challenging technique, as it requires extremely clean and stable surfaces, sharp tips, excellent vibration control, and sophisticated electronics.

In this thesis, *in situ* low temperature scanning tunneling microscopy (LT-STM) was used to study the morphology, atomic structure, and the growth mechanism of epitaxial graphene samples on 4H-SiC (000-1). The bias voltage (V_T) was 0.5 V and the scanning area was around 10 nm × 10 nm. The LT-STM measurements are conducted by our cooperator in the Surface Science Lab (SSL) in National University of Singapore (NUS).

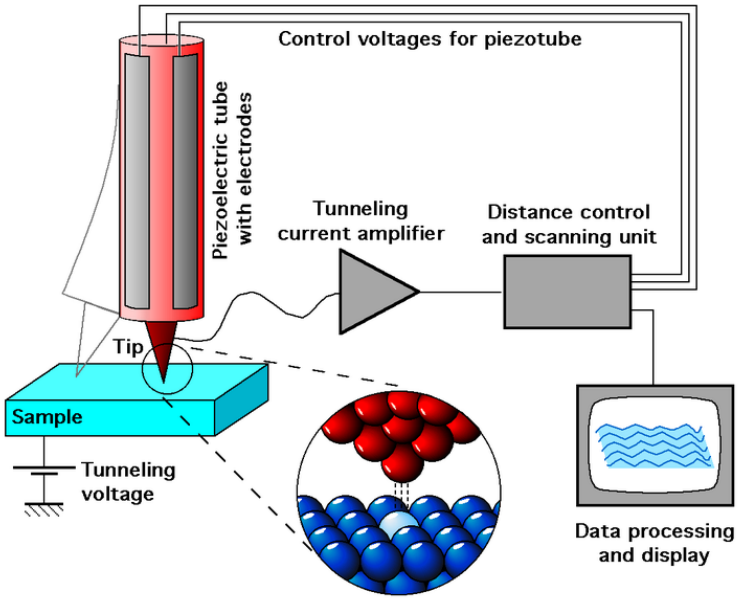

Figure 2.4. The schematic set-up of Scanning Tunneling Microscopy (STM).

2.2.3 The stacking sequence of graphene layers

The epitaxial graphene grown on the C face (000-1) of SiC could be as thin as from a few monolayers of graphene to several ten (>50) layers with electrical conductivities of few tens of thousands cm^2/V-s. The stacking sequence for the bilayer and multilayer graphene on the C face has attracted much attention [2.38-2.42]. It has been demonstrated that both misoriented bilayer and AB stacked bilayer was observed

by scanning tunneling microscopy (STM) on the epitaxial graphene on the C face of SiC [2.38], which is consistent with our STM studies as shown in Figure 2.5. In Figure 2.5 (b), the left side is STM image of the misoriented bilayer graphene, while the right side is the AB stacked bilayer graphene. More STM studies of epitaxial graphene have been shown in the references [2.30-2.32].

It should be pointed out that the AB stacking can also be identified by other techniques as discussed in the following. The stacking consequence of multilayer graphene on C face of SiC substrate can be studied by the angle-resolved photoemission spectroscopy technique (ARPES). ARPES is an ideal tool to directly measure the electronic band structure of graphene and determine the number of AB-stacked layers by measuring the number of Pi bands. Both rotations between adjacent layers and AB stacking was observed in the quasifreestanding multilayer graphene films on the carbon face of SiC (the ratio of rotated monolayers and AB stacked bilayer or multilayer is around 50%) [2.39]. The stacking sequence of multilayer graphene on the carbon face of SiC substrate can be determined by the high-resolution transmission electron microscopy (HRTEM). The HRTEM data prove that the three metastable configurations exist: ABAB, AAAA.ABCA [2.40]. The Micro-Raman spectrum of graphene on C face of SiC substrate also demonstrates the rotated and AB stacking features [2.41]. In a recent report, characteristic features of well-defined graphene bilayers were observed in magneto-transmission experiments [2.42].

Moreover, the interlayer stacking sequence can be revealed by 2D peak of Raman

spectroscopy. Ferrari et al. demonstrated that the shape of the 2D Raman peak may serve as the fingerprint to distinguish monolayer, bilayer and few-layer graphene. The 2D peak stems from a double resonance electron-phonon scattering process [2.43, 2.44]. For monolayer graphene the 2D peak can be fitted with a single Lorentzian, whereas the multiple bands in bilayer or few-layer graphene require fitting with four or more Lorentzians due to interlayer interaction [2.43, 2.44].

We also employed the Raman spectroscopic technique to double confirm the AB stacking. The details of Raman spectroscopy can be found in following section. In such spectra, we fit the 2D peak with four Lorentzian curves as shown in Figure 2.8 (b), which displays the characteristic feature of AB stacked bilayer graphene.

(a)

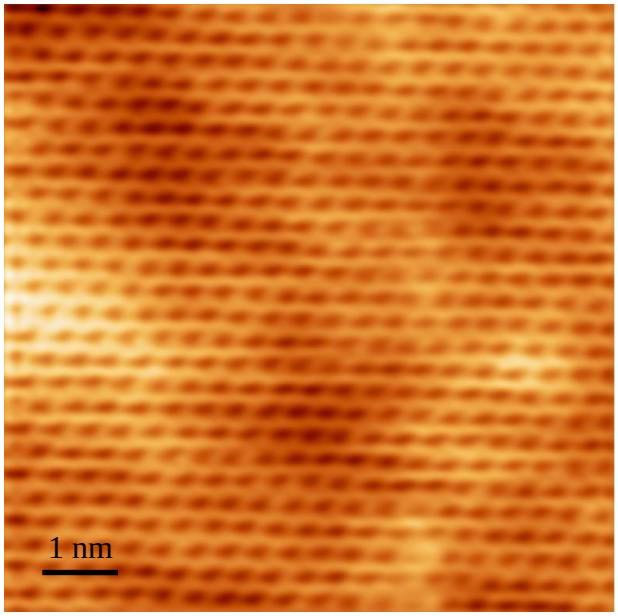

(b)

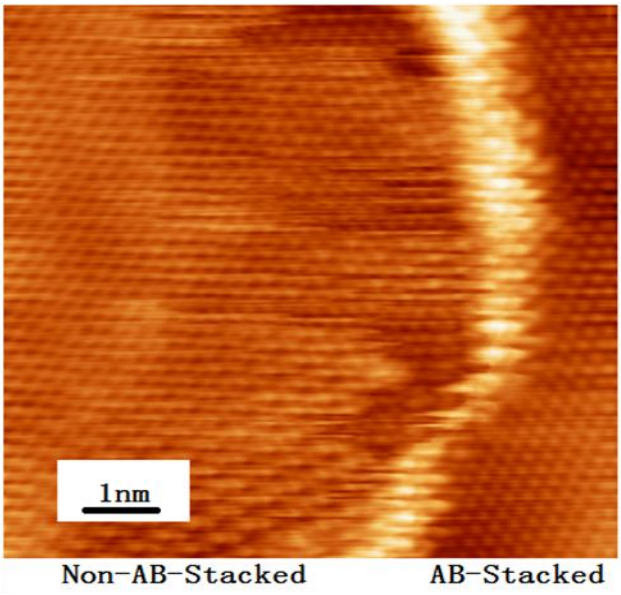

Figure 2.5. (a) The STM image of monolayer graphene on the C-face of SiC, which shows the hexagonal lattice structure, (b) The STM of bilayer graphene on the C-face of SiC. On the right side of the bright line, the clear triangular pattern indicates Bernal-stacking, as discussed in the text. On the left side, the absence of clear triangular pattern implies non-AB-stacking. The bilayer graphene sample consists of AB-stacking domains and non-AB-stacking domains on an area of 50 μm×50 μm.

2.3 Characterization of the graphene samples with optical methods

2.3.1 Introduction

The optical methods for characterizing graphene samples in this thesis include Raman spectroscopy and optical absorption spectroscopy. The characterization of graphene using optical methods detects the optical properties of the graphene samples in an illuminated area with the resolution that is limited by diffraction limitation. For the Micro-Raman spectroscopy measurements in this thesis, the laser spot size was around 500-nm in diameter. For the optical absorption spectroscopy measurements, the spot size of the light was around 1-mm in diameter. In this thesis, we measured absorption spectra of the graphene samples in Physics department of National University of Singapore (NUS).

Raman spectroscopy is a spectroscopic technique used to study vibrational, rotational, and other low-frequency modes in a system. It relies on inelastic scattering, or Raman scattering of monochromatic light, usually from a laser in the visible, near infrared, or near ultraviolet range. The laser light interacts with molecular vibrations, phonons or other excitations in the system, resulting in the energy of the laser photons being shifted, as shown in the energy diagram of Figure 2.6. The shift in energy gives information about the vibrational modes in the system. In the Raman spectroscopy experimental set-up, as shown in the lower part of Figure 2.6, the sample is illuminated with a laser beam. Light from the illuminated spot is collected with a lens and sent through a monochromator. Wavelengths close to the laser line due to elastic Rayleigh scattering are filtered out, while the rest of the collected light is dispersed

onto a detector.

In this thesis, the Raman spectra were measured with a WITEC CRM200 Raman system. The excitation source is a laser at 532 nm (2.33 eV) with power below 0.1 mW to avoid laser induced surface heating. The laser is focused by a 100× optical lens (NA = 0.95) and the spot size is around 500 nm in diameter. The Raman spectra are recorded under the above conditions to have the similar spatial resolution. The spectral resolution of the Raman system is ~1 cm^{-1}. The Raman spectra in this thesis were conducted under the help of our cooperator in Division of Physics and Applied Physics (PAP) in Nanyang Technological University (NTU). The typical Raman spectra of monolayer, bilayer and 6-layer samples on the C face of SiC are shown in Figure 2.7.

Absorption spectroscopy is a spectroscopic technique that measures the absorption of radiation by a sample, as a function of frequency or wavelength, due to its interaction with the sample. The sample absorbs photon energy with the resonant transition of electrons from ground state to the excited state. The intensity of the absorption is a function of density of states of the corresponding transition energy levels, and the function of absorption versus photon energy or wavelength gives the absorption spectrum. The absorption spectrum reflects the electronic structure of a material and is employed as an analytical chemistry tool to determine the presence of a particular substance in a sample and, in many cases, to quantify the amount of the substance present. In this thesis, the absorption spectra are measured by the Shimadzu

(UV-3600) UV-VIS-NIR Spectrophotometer. The measurable wavelength range is 185-3300 nm with spectral resolution of 0.1-nm. The light size is around 1-mm in diameter.

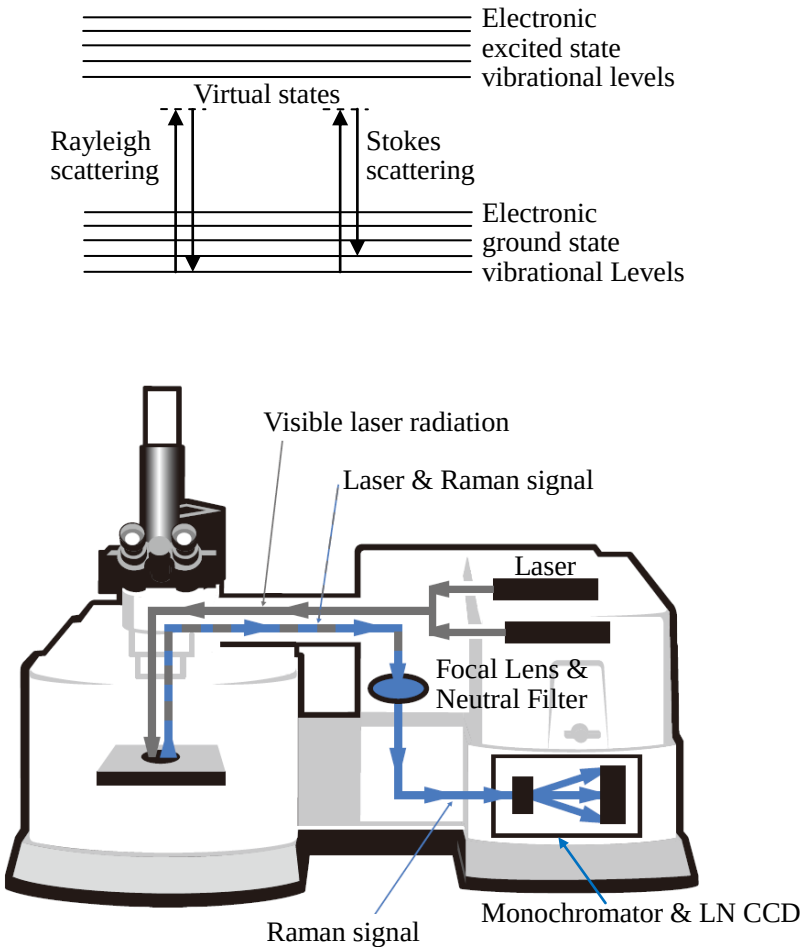

Figure 2.6. The energy diagram illustration of Raman scattering and the experimental set-up of Raman spectroscopy.

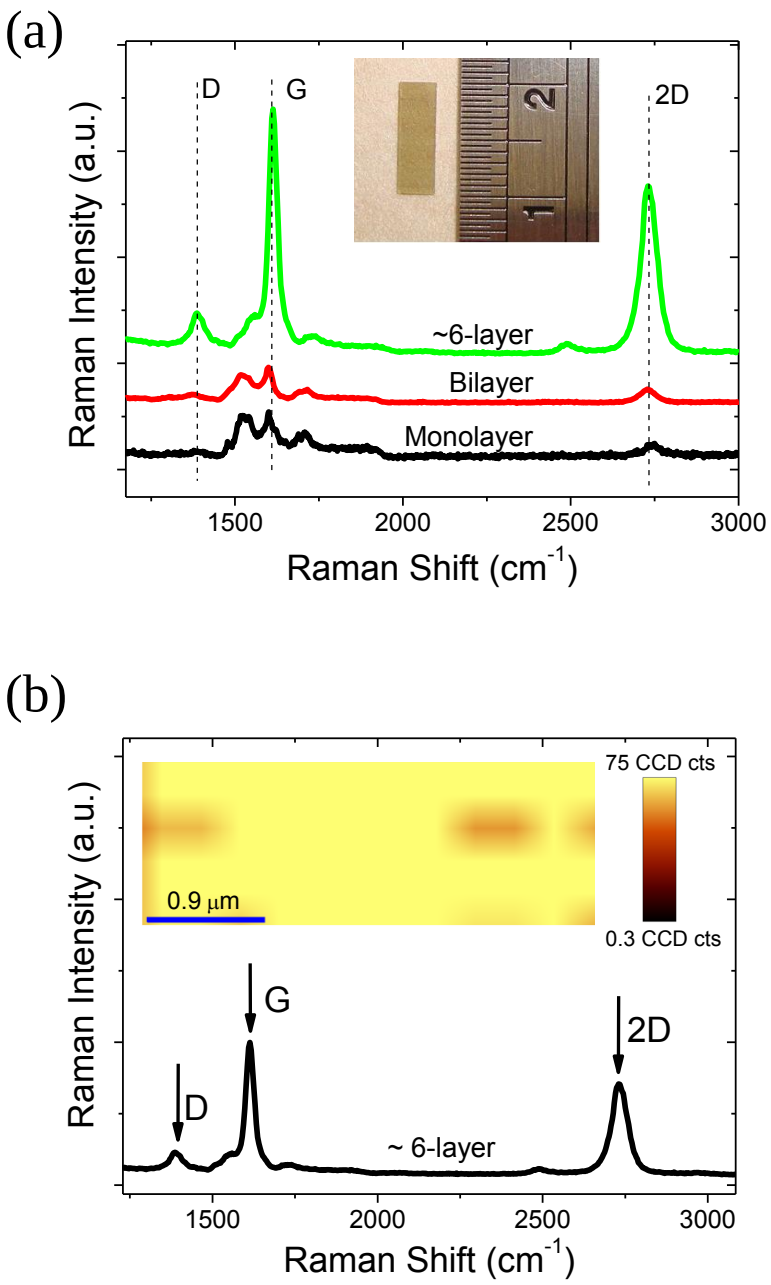

Figure 2.7. (a) Micro-Raman spectra of the mono-, bi- and 6-layer graphene on the C-face of SiC. The inset shows one of the three samples. (b) Micro-Raman spectra of 6-layer graphene on the C-face of SiC. The inset shows the micro-Raman mapping of the 6-layer graphene sample.

2.3.2 Density of defect states of the epitaxial graphene samples

Raman spectroscopy is known to be a powerful tool to determine the electronic properties of carbon-based materials, and there have been many reports about Raman measurements on epitaxial graphene to determine the density of defect states and the uniformity of graphene samples [2.45-2.48].

As shown in Figure 2.7, they are typical spectra of epitaxial graphene on SiC substrate. These spectra show a single-resonant G peak at 1600 cm^{-1}, a 2D peak at 2728 cm^{-1}, and a D peak near 1371 cm^{-1}, close to the reported values [2.46-2.48]. The 2D peak in graphene is due to the scattering by two phonons with opposite momentum in the highest optical branch near the *K* point in the momentum space [2.43]. The D peak is not allowed in perfect graphene layers since it requires an elastic scattering process, which is made possible by disorder, to satisfy momentum conservation [2.49]. The presence of the D peak, therefore, indicates the presence of disorder in the samples. In graphene, the intensity of the D peak in the Raman spectrum can be used as a measure of crystalline disorder since this peak is absent in perfect graphene layers. The ratio of the intensities, I_G and I_D, of the G and D peaks, respectively, in the Raman spectrum has been shown to be proportional to the crystal coherence length. In our measurement of the Raman spectroscopy of the epitaxial graphene samples, shown in Figure 2.7 & 2.9, the ratio of the intensities of I_G and I_D is 9 ± 1, which indicates the low density of defect states and high quality of the graphene samples. The measurements of the I_G:I_D of our samples and samples used by other research groups are shown in Table 2.2 together for comparison. From this

table, one may conclude that epitaxial samples are significantly better than graphene samples made by reduction from graphene oxide (RGO) or exfoliation of graphite powder in terms of presence of defects.

2.3.3 Number of layers of the epitaxial graphene samples

The method of determining the number of layer has been intensely studied since the first piece of graphene was exfoliated and transferred to the SiO_2/Si substrate. The techniques include, Optical Microscopy, Scanning Tunneling Microscopy, Raman Spectroscopy, and attenuation of the bulk SiC component in the Si 2p PES signal.

Exfoliated graphene which is transferred to the SiO_2/Si substrate (the thin film of SiO_2 is usually few hundred nanometer) shows a high contrast due to the interference effect, which makes the discrimination of number of layers possible with Optical Microscopy [2.50, 2.51]. However, for epitaxial graphene, the graphene layers are tightly contacted with the thick SiC substrate, the optical contrast is not high enough to determine the number of layers of graphene.

Scanning Tunneling Microscopy (STM) can discriminate monolayer and bilayer epitaxial graphene by imaging the atomic structures on SiC surface [2.30-2.32]. The STM image of monolayer graphene clearly reveals a honey-comb structure with a lattice constant of 0.24 ± 0.01 nm, in coincidence with the atomic structure of monolayer graphene. The bilayer graphene involves AB (Bernal) stacking, breaks the symmetry of the graphene hexagonal lattice resulting in two inequivalent sublattices; this leads to the appearance of the triangular lattice in STM image. However, for thicker graphene samples, it is not easy to determine the number of layers by STM.

In our measurement, the monolayer and bilayer graphene were determined from the Scanning Tunneling Microscopy (STM) measurements. For the monolayer graphene, the STM shows the hexagonal lattice structure, as shown in Figure 2.5(a). However, the bilayer epitaxial graphene involves AB (Bernal) stacking, shows the triangular lattice of the STM, as shown in Figure 2.5(b).

Besides the STM technique, Raman spectroscopy is another important method of measuring the number of layers of graphene with high efficiency. Ferrari et al. have demonstrated that the shape of the 2D Raman peak may serve as the fingerprint to distinguish monolayer, bilayer, and few-layer graphene [2.43, 2.44]. The 2D peak stems from a double resonance electron-phonon scattering process. For monolayer graphene the 2D peak can be fitted with a single Lorentzian, whereas the multiple bands in bilayer or few-layer graphene require fitting to four or more Lorentzians. In the bilayer or multilayer graphene, the electronic bands are splitted due to the interlayer interaction. According to the density functional theory (DFT), four wave vectors correspond to phonons with different frequencies, couples strongly with the incident light. Such that, four or more Lorentzians are required in the fitting of 2D Raman peak of bilayer or few-layer graphene [2.43]. The 2D peak of Raman spectrum of the bilayer epitaxial graphene sample is fitted perfectly with four Lorentzians, which is consistent with previous reports [2.46], as shown in Figure 2.8(b), while the 2D peak of Raman spectrum for the monolayer sample is fitted with single Lorentzian, as shown in Figure 2.8(a). For epitaxial graphene with more layers (>2), the number of layers can be determined by the attenuation of the Raman signals of the SiC

substrate [2.52]. As shown in Figure 2.8(c), the signal of SiC substrate is subtracted from the original Raman signal of epitaxial graphene to get the pure Raman signal of graphene. The relation of the remaining fraction of the substrate Raman signal S and the graphene thickness t can be expressed as $S = e^{-2\alpha t}$, where α = 2.3%, which is the attenuation of monolayer graphene. For the multilayer graphene which was used, the value of S is 0.76, demonstrating the number of layer of multilayer graphene is around 6.

(a)

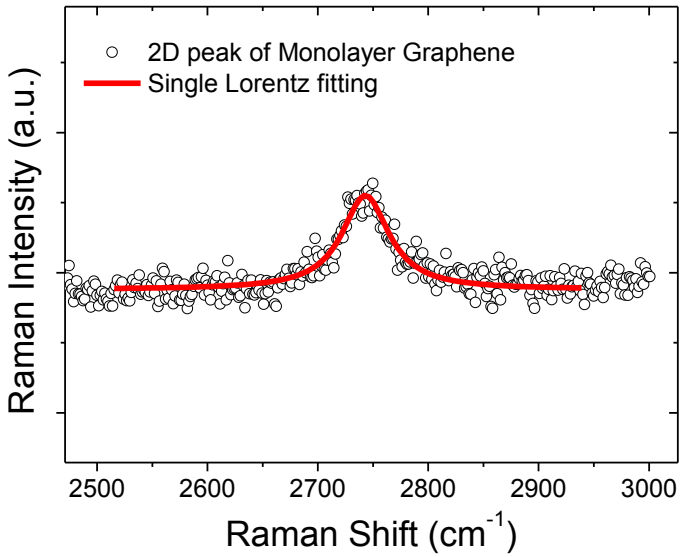
2D peak of Monolayer Graphene
Single Lorentz fitting
Raman Intensity (a.u.)
2500
2600
2700
2800
2900
3000
Raman Shift (cm-1)

(b)

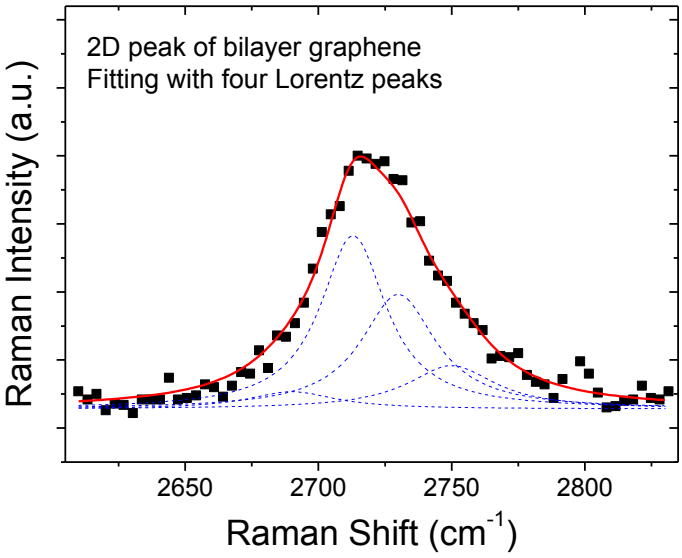
2D peak of bilayer graphene
Fitting with four Lorentz peaks
Raman Intensity (a.u.)
2650
2700
2750
2800
Raman Shift (cm-1)

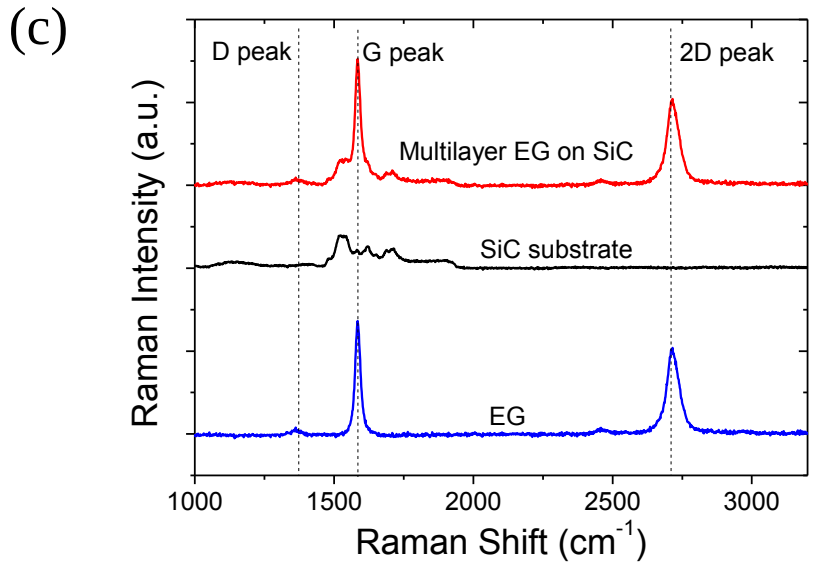

Figure 2.8. (a) The 2D peak of the Raman spectroscopy of monolayer epitaxial graphene on C-face of SiC, fitted with single Lorentz peak. (b) The 2D peak of the Raman spectroscopy of bilayer epitaxial graphene on C-face of SiC, fitted with four Lorentz peaks. (c) The Raman spectroscopy of 6-layer graphene and the substrate. The attenuation of the SiC substrate signal is used to calculate the number of graphene layers as discussed in the text.

2.3.4 The homogeneity of the epitaxial graphene samples

In order to measure the homogeneity of the epitaxial graphene samples, the Micro-Raman measurements (d = 400 nm) were carried out in different areas of the epitaxial graphene samples, as sketched in Figure 2.3(c), where the nonlinear optical measurements were carried out. The Micro-Raman spectrum at each position of the bilayer sample is shown in Figure 2.9. The quality and homogeneity of the samples were demonstrated by analyzing the defect states related D peak in the Micro-Raman spectrum. The measured values of I_G:I_D of each sample and different points in the bilayer graphene sample are listed in Table 2.2. The value of I_G:I_D is 9 ± 1, which indicates the high quality and uniformity of the graphene samples. In addition, the

Micro-Raman mapping of the G peak was carried out (with resolution of 400 nm) in an area of 1 μm^2 to study the homogeneous of the sample, as shown in the inset of Figure 2.7(b), which is the Micro-Raman mapping of the G peak of 6-layer graphene. In the measurement, the deviation of the intensity of G peak was within 15%, which demonstrates the high homogeneous of the graphene samples.

(a)

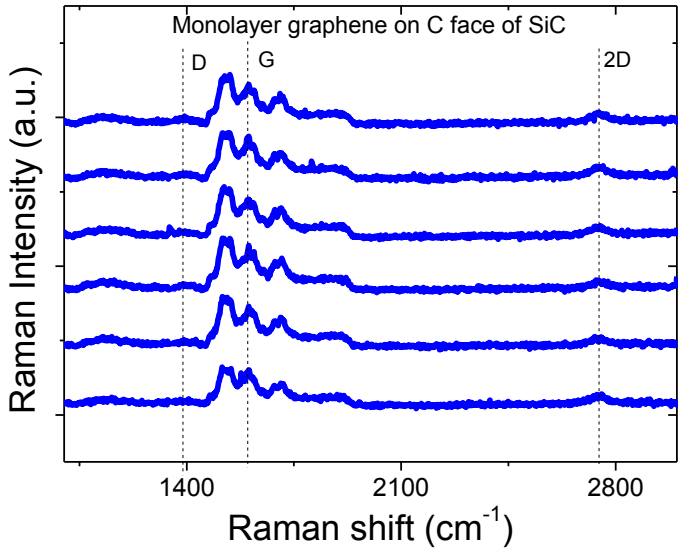

(b)

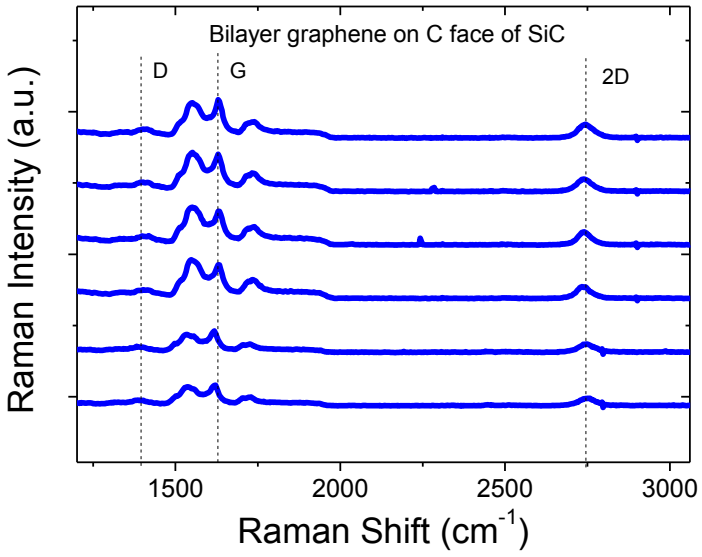

(c)

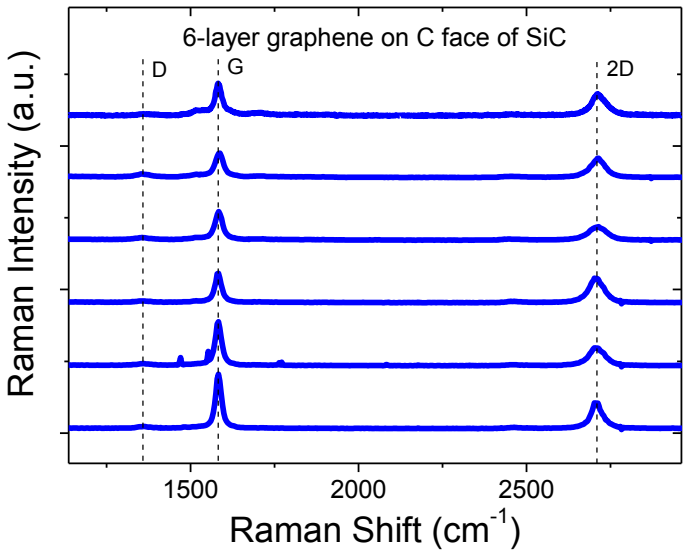

Figure 2.9. The Raman spectra of the graphene samples. For each sample, the Raman spectra of six different points (or position) were recorded for comparison in order to examine the homogeneousness of the samples. The Raman spectra (a), (b), (c) are of sample #2, #3, and #4, respectively.

Table 2.2. The density of defect states and homogeneity of graphene samples.

Sample		Number of layer	I_G/I_D	References
Monolayer EG		1	9	Present study
Bilayer EG	Point 1	2	9	
	Point 2	2	8	
	Point 3	2	8	
	Point 4	2	9	
	Point 5	2	7	
	Point 6	2	9	
6-layer EG		6	10	
EG	Sample A	6	13	[2.28]
	Sample B	12	17	
	Sample C	37	2	
CVD		8	3-8	[2.18]
RGO		Few layers	1.3	[2.9]
Exfoliation of graphite powder		Few layers	3	[2.10]

2.3.5 Optical absorption spectroscopy of the graphene samples

The optical absorption measurement of graphene was reported in the visible range [2.3]. It was demonstrated that the opacity of suspended graphene is defined solely by the fine structure constant, $\alpha = e^2/\hbar c \approx 1/137$ (where c is the speed of light), the parameter that describes coupling between light and relativistic electrons and that is

traditionally associated with quantum electrodynamics rather than materials science. The opacity of a monolayer graphene was measured to be 2.3% in the entire visible spectral range. The absorbed energy was calculated by using Fermi's golden rule and the theoretical study also confirmed the fact that the optical properties of graphene are defined by the fundamental constants, which is related to its 2D nature and zero energy gap and does not directly involve the chiral properties of Dirac fermions. The measurement of the optical absorption spectra of epitaxial graphene from Terahertz to visible range was performed and the Drude-like frequency dependence of the intraband conductivity of graphene in the THz frequency range was confirmed [2.53].

The optical absorption spectroscopy of the epitaxial graphene samples in this thesis were measured with UV-VIS-NIR spectrophotometer (Shimadzu UV-VIS-NIR Spectrophotometer UV-3600). The experimental measurements of the optical absorbance and transmittance spectroscopy of the graphene samples are shown in Figure 2.10(b) and (c).

The Febry-Perot interference is a phenomenon when light transmits through thin films. The Febry-Perot interference results in the oscillation in the optical transmission spectrum and the oscillation period is related to the thickness of the thin film [2.56]. In the measured optical transmission spectrum of epitaxial graphene samples, the spectrum is free from oscillation in a wide range, which indicates the effect of Febry-Perot interference is trivial. The reason could be due to the negligible reflectance of graphene, the ultrathin feature of graphene layer [2.3, 2.55] and thicker SiC substrate comparing with the reported SiO_2 layer [2.50].

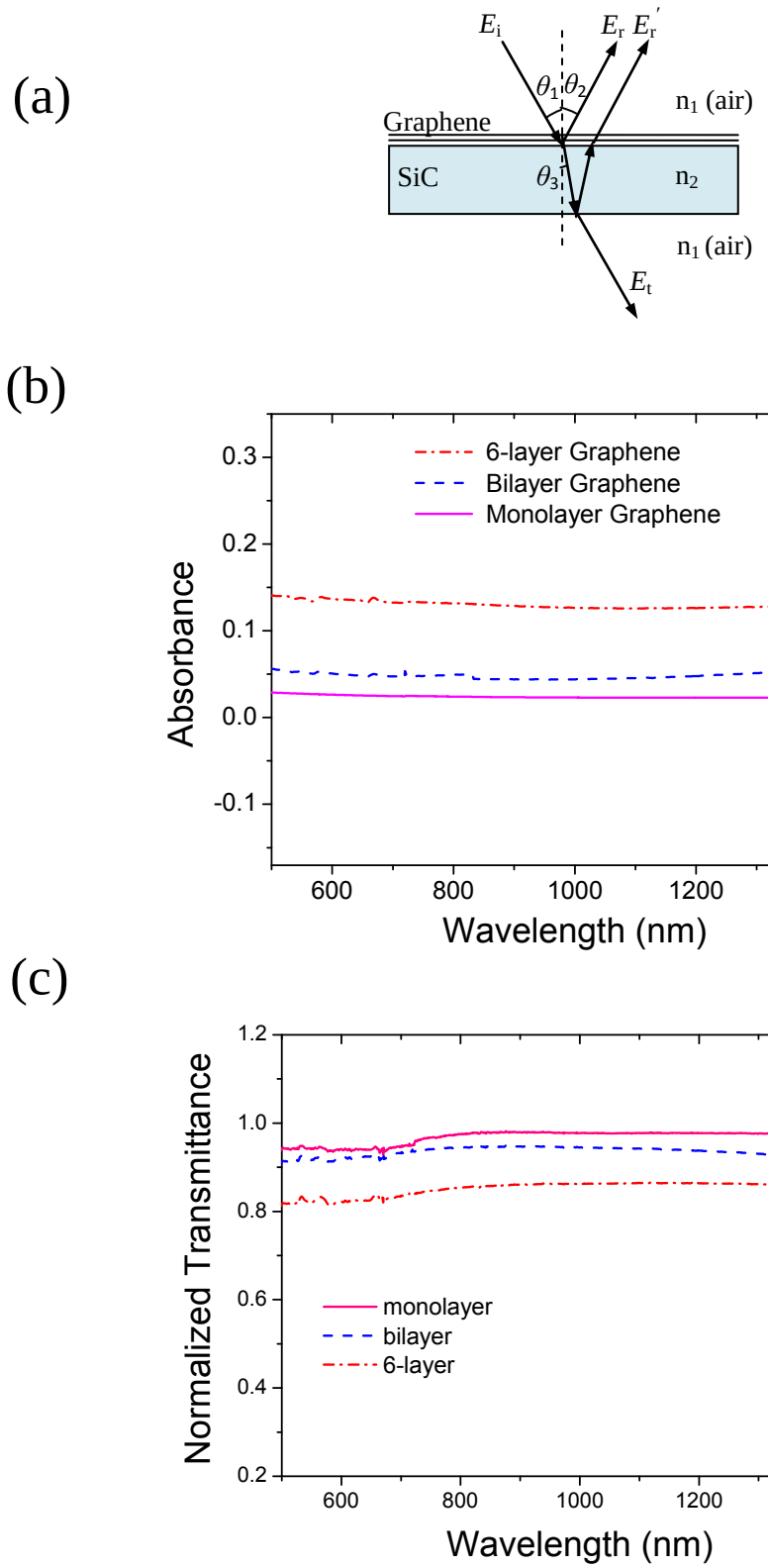

Figure 2.10. (a) Schematic diagram for light scattering on graphene separated interfaces, n_1/n_2 represent the refractive indices of the two media. (b) The absorbance and (c) normalized transmittance spectra of the graphene samples, normalized with transmittance signal of SiC substrate.

2.4 Conclusion

In conclusion, monolayer, bilayer and multilayer epitaxial graphene on C-face of 4H-SiC substrate were synthesized in the UHV furnace at high temperatures. The basic properties of graphene samples, such as the number of layers, density of defect states, the interlayer stacking consequence and homogeneity were characterized by STM, Micro-Raman spectroscopy and optical absorption spectroscopy. These characterizations support that the epitaxial graphene samples used in this thesis are of high quality, and great degree of homogeneousness with clear discrimination of number of layers.

References

[2.1] K. S. Novoselov, A. K. Geim, S. V. Morozov *et al.*, "Electric field effect in atomically thin carbon films," Science, **306,** 666-669 (2004).

[2.2] K. S. Novoselov, Z. Jiang, Y. Zhang *et al.*, "Room-temperature quantum Hall effect in graphene," Science, **315,** 1379 (2007).

[2.3] R. R. Nair, P. Blake, A. N. Grigorenko *et al.*, "Fine structure constant defines visual transparency of graphene," Science, **320,** 1308 (2008).

[2.4] K. F. Mak, M. Y. Sfeir, Y. Wu *et al.*, "Measurement of the optical conductivity of graphene," Phys. Rev. Lett., **101,** 196405 (2008).

[2.5] A. B. Kuzmenko, L. Benfatto, E. Cappelluti *et al.*, "Gate tunable infrared phonon anomalies in bilayer graphene," Phys. Rev. Lett., **103,** 116804 (2009).

[2.6] Y. Wang, Z. Ni, L. Liu *et al.*, "Stacking-dependent optical conductivity of bilayer graphene," ACS Nano, **4,** 4074-4080 (2010).

[2.7] E. Hendry, P. J. Hale, J. Moger *et al.*, "Coherent nonlinear optical response of graphene," Phys. Rev. Lett., **105,** 097401 (2010).

[2.8] V. Eswaraiah, S. S. Jyothirmayee Aravind, and S. Ramaprabhu, "Top down method for synthesis of highly conducting graphene by exfoliation of graphite oxide using focused solar radiation," J. Mater. Chem., **21,** 6800-6803 (2011).

[2.9] S. Wang, P. K. Ang, Z. Wang *et al.*, "High mobility, printable, and solution-processed graphene electronics," Nano Lett., **10,** 92-98 (2009).

[2.10] U. Khan, A. O'Neill, M. Lotya *et al.*, "High-concentration solvent exfoliation of graphene," Small, **6,** 864-871 (2010).

[2.11] C. J. Shih, A. Vijayaraghavan, R. Krishnan *et al.*, "Bi- and trilayer graphene solutions," Nature Nanotech., **6,** 439-445 (2011).

[2.12] C. Y. Su, A. Y. Lu, Y. Xu *et al.*, "High-quality thin graphene films from fast electrochemical exfoliation," ACS Nano, **5,** 2332-2339 (2011).

[2.13] P. Blake, P. D. Brimicombe, R. R. Nair *et al.*, "Graphene-based liquid crystal device," Nano Lett., **8,** 1704-1708 (2008).

[2.14] A. Reina, X. Jia, J. Ho *et al.*, "Large area, few-layer graphene films on arbitrary substrates by chemical vapor deposition," Nano Lett., **9,** 30-35 (2008).

[2.15] K. S. Kim, Y. Zhao, H. Jang *et al.*, "Large-scale pattern growth of graphene films for stretchable transparent electrodes," Nature, **457,** 706-710 (2009).

[2.16] J. Shang, T. Yu, J. Lin *et al.*, "Ultrafast electron−optical phonon scattering and quasiparticle lifetime in CVD-grown graphene," ACS Nano, **5,** 3278-3283 (2011).

[2.17] B. J. Schultz, C. J. Patridge, V. Lee et al., "Imaging local electronic corrugations and doped regions in graphene," Nature Commun., **2,** 372 (2011).

[2.18] V. Ivan, S. Sergei, I. Ilia *et al.*, "Electrical and thermal conductivity of low temperature CVD graphene: the effect of disorder," Nanotechnology, **22,** 275716 (2011).

[2.19] J. D. Wood, S. W. Schmucker, A. S. Lyons *et al.*, "Effects of polycrystalline Cu substrate on graphene growth by chemical vapor deposition," Nano Lett., **11,** 4547-4554 (2011).

[2.20] A. J. Van Bommel, J. E. Crombeen, and A. Van Tooren, "LEED and Auger electron observations of the SiC(0001) surface," Surf. Sci., **48,** 463-472 (1975).

[2.21] F. Owman, and P. Mårtensson, "The SiC(0001)$6\sqrt{3} \times 6\sqrt{3}$ reconstruction studied with STM and LEED," Surf. Sci., **369,** 126-136 (1996).

[2.22] C. Berger, Z. Song, T. Li *et al.*, "Ultrathin epitaxial graphite: 2D electron gas properties and a route toward graphene-based nanoelectronics," J. Phys. Chem. B, **108,** 19912-19916 (2004).

[2.23] K. V. Emtsev, A. Bostwick, K. Horn *et al.*, "Towards wafer-size graphene layers by atmospheric pressure graphitization of silicon carbide," Nature Mater., **8,** 203-207 (2009).

[2.24] C. Berger, Z. Song, X. Li *et al.*, "Electronic confinement and coherence in patterned epitaxial graphene," Science, **312,** 1191-1196 (2006).

[2.25] T. Ohta, A. Bostwick, J. L. McChesney *et al.*, "Interlayer interaction and electronic screening in multilayer graphene investigated with angle-resolved photoemission spectroscopy," Phys. Rev. Lett., **98,** 206802 (2007).

[2.26] S. V. Morozov, K. S. Novoselov, M. I. Katsnelson *et al.*, "Strong suppression of weak localization in graphene," Phys. Rev. Lett., **97,** 016801 (2006).

[2.27] D. Sun, C. Divin, J. Rioux *et al.*, "Coherent control of ballistic photocurrents

in multilayer epitaxial graphene using quantum interference," Nano Lett., **10,** 1293-1296 (2010).

[2.28] J. M. Dawlaty, S. Shivaraman, M. Chandrashekhar *et al.*, "Measurement of ultrafast carrier dynamics in epitaxial graphene," Appl. Phys. Lett., **92,** 042116 (2008).

[2.29] P. A. George, J. Strait, J. Dawlaty *et al.*, "Ultrafast optical-pump terahertz-probe spectroscopy of the carrier relaxation and recombination dynamics in epitaxial graphene," Nano Lett., **8,** 4248-4251 (2008).

[2.30] W. Chen, H. Xu, L. Liu *et al.*, "Atomic structure of the 6H–SiC(0001) nanomesh," Surf. Sci., **596,** 176-186 (2005).

[2.31] S. W. Poon, W. Chen, E. S. Tok *et al.*, "Probing epitaxial growth of graphene on silicon carbide by metal decoration," Appl. Phys. Lett., **92,** 104102 (2008).

[2.32] H. Huang, W. Chen, S. Chen *et al.*, "Bottom-up growth of epitaxial graphene on 6H-SiC(0001)," ACS Nano, **2,** 2513-2518 (2008).

[2.33] P. Sutter, "Epitaxial graphene: How silicon leaves the scene," Nature Mater., **8,** 171-172 (2009).

[2.34] A. d. H. Walt, B. Claire, X. S. Wu *et al.*, "Epitaxial graphene electronic structure and transport," J. Phys. D: Appl. Phys., **43,** 374007 (2010).

[2.35] A. Mattausch, and O. Pankratov, "Ab Initio study of graphene on SiC," Phys. Rev. Lett., **99,** 076802 (2007).

[2.36] X. Peng, and R. Ahuja, "Symmetry breaking induced bandgap in epitaxial

graphene layers on SiC," Nano Lett., **8,** 4464-4468 (2008).

[2.37] A. H. Castro Neto, F. Guinea, N. M. R. Peres *et al.*, "The electronic properties of graphene," Rev. Mod. Phys. , **81,** 109-162 (2009).

[2.38] F. Varchon, P. Mallet, L. Magaud *et al.*, "Rotational disorder in few-layer graphene films on 6H-SiC(000-1): A scanning tunneling microscopy study," Phys. Rev. B, **77,** 165415 (2008).

[2.39] D. A. Siegel, C. G. Hwang, A. V. Fedorov *et al.*, "Quasifreestanding multilayer graphene films on the carbon face of SiC," Phys. Rev. B, **81,** 241417 (2010).

[2.40] J. Borysiuk, J. Soltys, and J. Piechota, "Stacking sequence dependence of graphene layers on SiC (0001)---Experimental and theoretical investigation," J. Appl. Phys., **109,** 093523 (2011).

[2.41] A. Tiberj, N. Camara, P. Godignon *et al.*, "Micro-Raman and micro-transmission imaging of epitaxial graphene grown on the Si and C faces of 6H-SiC," Nanoscale Res. Lett., **6,** 478 (2011).

[2.42] M. Orlita, C. Faugeras, J. Borysiuk *et al.*, "Magneto-optics of bilayer inclusions in multilayered epitaxial graphene on the carbon face of SiC," Phys. Rev. B, **83,** 125302 (2011).

[2.43] A. C. Ferrari, J. C. Meyer, V. Scardaci *et al.*, "Raman spectrum of graphene and graphene layers," Phys. Rev. Lett., **97,** 187401 (2006).

[2.44] F. Andrea C, "Raman spectroscopy of graphene and graphite: Disorder, electron–phonon coupling, doping and nonadiabatic effects," Solid State

Commun., **143,** 47-57 (2007).

[2.45] D. Graf, F. Molitor, K. Ensslin *et al.*, "Spatially resolved Raman spectroscopy of single- and few-layer graphene," Nano Lett., **7,** 238-242 (2007).

[2.46] D. S. Lee, C. Riedl, B. Krauss *et al.*, "Raman spectra of epitaxial graphene on SiC and of epitaxial graphene transferred to SiO_2," Nano Lett., **8,** 4320-4325 (2008).

[2.47] Z. H. Ni, W. Chen, X. F. Fan *et al.*, "Raman spectroscopy of epitaxial graphene on a SiC substrate," Phys. Rev. B, **77,** 115416 (2008).

[2.48] Y. Y. Wang, Z. H. Ni, T. Yu *et al.*, "Raman studies of monolayer graphene: The substrate effect," J. Phys. Chem. C, **112,** 10637-10640 (2008).

[2.49] A. C. Ferrari, and J. Robertson, "Interpretation of Raman spectra of disordered and amorphous carbon," Phys. Rev. B, **61,** 14095-14107 (2000).

[2.50] I. Jung, M. Pelton, R. Piner *et al.*, "Simple approach for high-contrast optical imaging and characterization of graphene-based sheets," Nano Lett., **7,** 3569-3575 (2007).

[2.51] Z. H. Ni, H. M. Wang, J. Kasim *et al.*, "Graphene thickness determination using reflection and contrast spectroscopy," Nano Lett., **7,** 2758-2763 (2007).

[2.52] S. Shivaraman, M. Chandrashekhar, J. Boeckl *et al.*, "Thickness estimation of epitaxial graphene on SiC using attenuation of substrate Raman intensity," J. Electron. Mater., **38,** 725-730 (2009).

[2.53] J. M. Dawlaty, S. Shivaraman, J. Strait *et al.*, "Measurement of the optical

absorption spectra of epitaxial graphene from terahertz to visible," Appl. Phys. Lett., **93,** 131905 (2008).

[2.54] L. A. Falkovsky, and S. S. Pershoguba, "Optical far-infrared properties of a graphene monolayer and multilayer," Phys. Rev. B, **76,** 153410 (2007).

[2.55] T. Stauber, N. M. R. Peres, and A. K. Geim, "Optical conductivity of graphene in the visible region of the spectrum," Phys. Rev. B, **78,** 085432 (2008).

[2.56] R. Swanepoel, "Determination of the thickness and optical constants of amorphous silicon," J. Phys. E: Sci. Instrum., **16,** 1214 (1983).

Chapter 3

Nonlinear optical experimental techniques

3.1 Introduction

In the previous chapter, Raman spectroscopy, Scanning Tunneling Microscopy (STM), Scanning Electron Microscopy (SEM), and UV-Vis-IR absorption spectroscopy have been described. These experimental techniques can assist us to evaluate the quality of samples. In this chapter, we will focus on Z-scan technique and pump-probe measurement (also called transient absorption measurement), two vital experimental techniques in the investigation of nonlinear optical properties of materials as these two techniques will be employed to study the nonlinear optical properties of graphene in the following chapters.

3.2 Z-scan technique

The nonlinear optical properties of materials are important to many applications such as ultrafast optical switching, optical processing, bio-imaging and targeting. Thus, the characterization of these properties in materials has been intensely studied in the past decades. Many experimental techniques has been proposed and studied. Such as, degenerate four-wave mixing [3.1], ellipse rotation [3.2] and beam distortion measurement [3.3]. Even through these techniques show different advantages, they have the shortcoming of requiring either relatively complex optical alignment or wave propagation analysis.

3.2.1 Z-scan experiment set-up

Sheik-Bahae et al. proposed the Z-scan technique in 1990 [3.4]. The Z-scan technique is a sensitive technique with simple experiment set-ups to measure the nonlinear optical coefficients. In the Z-scan technique, the sample moves along the beam propagating direction (z-direction) through the focal plane, in which process the sample is under variable irradiance at each z-position. The transmittance through the sample is recorded at each z-position and analyzed using the Z-scan theory. The experimental set-up of transmittance Z-scan is sketched in Figure 3.1. The incoming beam is first split by a beam splitter. The reflected light is recorded by detector D_1, as a reference to balance the fluctuation of the light energy. The transmitted light is focused by a convex lens and the power of the light transmitted through the sample is measured by detector D_2. Then the information of the nonlinearity can be derived from the ratio of D_2 to D_1 as a function of the position z (relative to the focal plan). Without an aperture in front of D_2, the entire energy transmitted through the sample is collected and such that the nonlinear absorption can be extracted by fitting Z-scan theory to the experimental data. This method is thus called open-aperture Z-scan. For a material with nonlinear refractive property, when the intense laser beam passes through the sample, the refractive index of the sample will be modified according to the intensity distribution of the incident beam. At the meantime, the wave front of the transmitted beam will be modified related to the redistribution of the refractive index in the sample. If an aperture is placed in the far field before detector D_2 as shown in Figure 3.1, the modulation of the wave front of the beam can be detected. In such a

way, the information of the nonlinear refractive index of the sample can be measured. Such a configuration is called closed-aperture Z-scan.

In the Z-scan experiment, the thickness of the sample L should be smaller than the diffraction length of the focused beam ($L < z_0 = \pi w_0^2/\lambda$, w_0 is the beam waist). In this case, the sample length is small enough that changes in the beam diameter within the sample due to either diffraction or nonlinear refraction can be neglected, the sample can be regarded as thin sample, in which the self-refraction process can be referred to as “external self-action”.

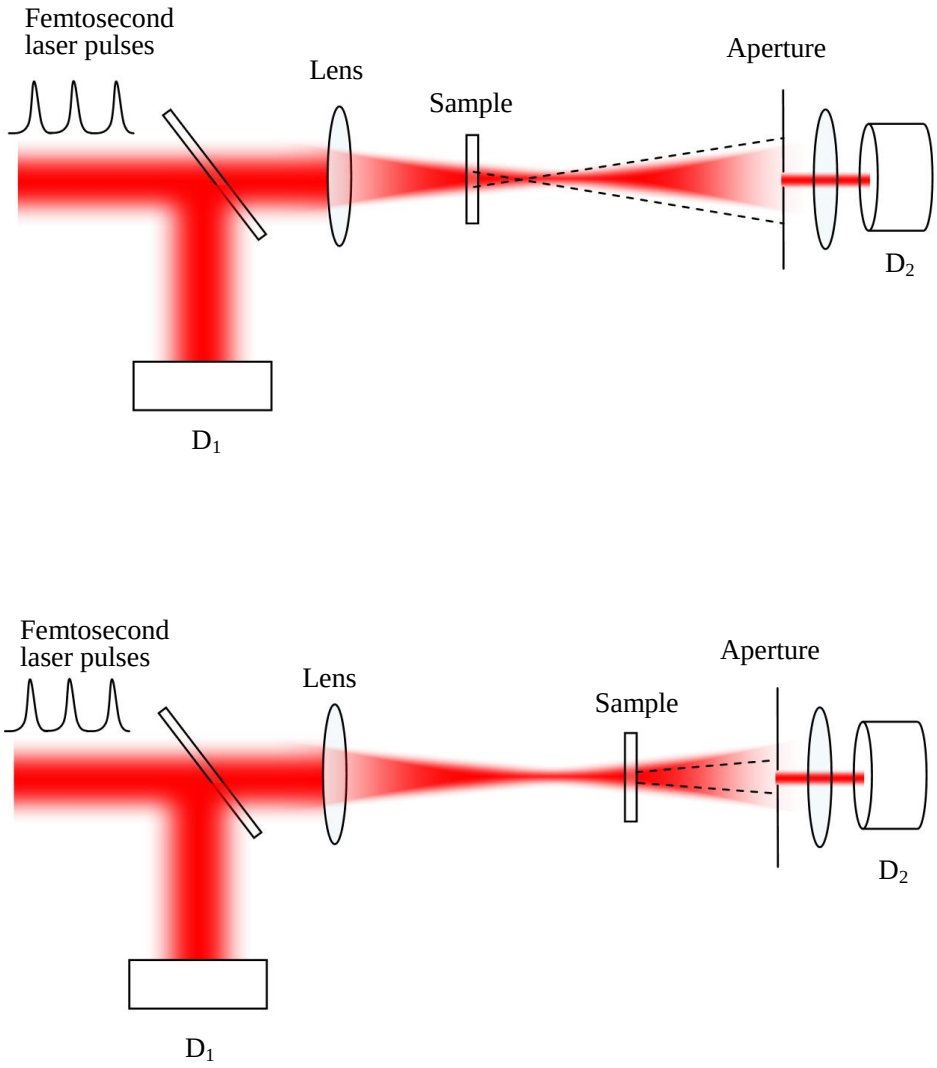

Figure 3.1. Closed-aperture transmission Z-scan experiment set-up for measuring the nonlinear absorption and nonlinear refraction properties of materials.

3.2.2 Closed-aperture Z-scan technique and data analysis

The nonlinear refraction properties of the third-order nonlinear optical materials can be measured using the closed-aperture (CA) Z-scan technique. In the CA Z-scan experiment, a finite aperture is put in the far field before detector D_2 as shown in

Figure 2.1. Assume, for instance, a material with a positive nonlinear refractive index and negligible nonlinear absorption with thickness can be assumed as “thin” sample. Starting the scan from a distance far away from the focus (negative z), the beam irradiance is low and negligible nonlinear refraction occurs; hence, the transmittance (D_2/D_1 in Figure 3.1) remains relatively constant. As the sample is brought closer to the focus, the beam irradiance increases, leading to self-lensing in the sample. A self-lensing prior to focus will lead to the divergence of the beam at the aperture, which results in a decrease in the measured transmittance. As the sample continue moves in the positive z direction and passes through the focal plane to the right, the self-focusing of the sample increases the beam collimate at the aperture, and thus leads to an increase in transmittance. This suggests that there is a null as the sample moves to the focal plane. This is analogous to placing a thin lens at or near the focus, resulting in a minimal change of the far-field pattern of the beam. The Z-scan is completed as the sample is moved away from focus (positive z) such that the transmittance becomes linear since the irradiance decreases. A typical closed-aperture Z-scan trace is shown in Figure 3.2 of 1-mm quartz wafer, which shows positive third-order nonlinear refractive index.

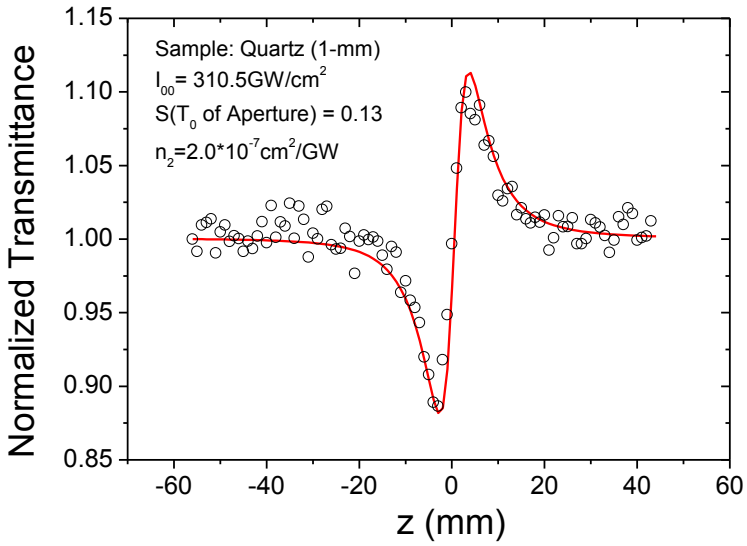

Figure 3.2. The closed-aperture Z-scan trace of the 1-mm quartz substrate, which possesses a positive third-order nonlinear refractive index.

In general, nonlinearities of any order should be considered. However, for simplicity, we first examine only a third-order nonlinearity where the refractive index n is expressed in terms of the nonlinear refractive index n_2 (Unit: m^2/W) by $n = n_0+n_2I$, where n_0 is the linear refaractive index of refraction, and I denotes the irradiance of the laser beam within the sample. Assuming a TEM_{00} Gaussian beam of beam waist radius w_0 traveling in the +z direction, we can write E as,

$$E(z,r,t) = E_0(t)\frac{w_0}{w(z)}\cdot\exp(-\frac{r^2}{w^2(z)}-\frac{ikr^2}{2R(z)})e^{-i\phi(z,t)} \qquad (3.1)$$

where $w^2(z) = w_0^2(1+z^2/z_0^2)$ is the beam radius, $R(z) = z/(1+ z_0^2/z^2)$ is the radius of curvature of the wavefront at z, $z_0 = kw_0^2/2$ is the diffraction length of the beam, $k = 2\pi/\lambda$. $E_0(t)$ denotes the radiation electric field at the focus and contains the temporal envelope of the laser pulse. The term $e^{-i\phi(z,t)}$ contains all the radially

uniform phase variations. Under slowly varying envelope approximation (SVEA), the differential equation of the phase and intensity change of beam propagating through the sample can be expressed as,

$$\frac{d\Delta\phi}{dz'} = \Delta n(I)k \tag{3.2}$$

$$\frac{dI}{dz'} = -\alpha(I)k \tag{3.3}$$

where z' is the propagation depth in the sample and $\alpha(I)$, in general, includes linear and nonlinear absorption terms. Note that z' should not be confused with the sample position *z*. In the case of a third-order nonlinearity and negligible nonlinear absorption, Equations (2.2) and (2.3) are solved to give the phase shift $\Delta\phi$ at the exit surface of the sample which simply follows the radial variation of the incident irradiance at a given position of the sample *z*. thus,

$$\Delta\phi(z,r,t) = \Delta\phi_0(z,t)\exp(-\frac{2r^2}{w^2(z)}) \tag{3.4}$$

with

$$\Delta\phi_0(z,t) = \frac{\Delta\Phi_0(t)}{1+z^2/z_0^2} \tag{3.5}$$

$\Delta\Phi_0(t)$, the on-axis phase shift at the focus, is defined as

$$\Delta\Phi_0(t) = k\Delta n_0(t)L_{eff} \tag{3.6}$$

where $L_{eff} = (1-e^{-\alpha_0 L})/\alpha_0$, with L the sample length and α_0 the linear absorption coefficient. Here, $\Delta n_0 = n_2 I_0(t)$ with $I_0(t)$ being the on-axis irradiance at focus (*z*=0) in the sample (deducting the Fresnel reflection losses at the front surface of the sample). The complex electric field exiting the sample E_e now contains the nonlinear

phase distortion

$$E_e(r,z,t) = E(z,r,t)e^{-\alpha L/2}e^{i\Delta\phi(z,r,t)} \tag{3.7}$$

As the beam propagates to the aperture, the electric field is determined by the Huygens-Fresnel propagation integral as follows [3.4]:

$$E_a(z,r,t) = \frac{2\pi}{i\lambda(d-z)}e^{\frac{i\pi r^2}{\lambda(d-z)}}\int_0^\infty r'E(z,r',t)e^{\frac{i\pi r'^2}{\lambda(d-z)}}J_0[\frac{2\pi rr'}{\lambda(d-z)}]dr' \tag{3.8}$$

where d is the distance between the aperture and the focal plane. $J_0(x)$ is the Bessel's function of the zero order. The transmitted power through the aperture is then given as:

$$P_t(z,t) = c\varepsilon_0 n_0 \pi\int_0^{r_a}\left|E_a(z,r,t)\right|^2 rdr \tag{3.9}$$

where r_a is the radius of the aperture. The normalized transmittance is given by:

$$T(z,s) = \frac{\int_{-\infty}^{\infty}P_t(z,t)dt}{S\int_{-\infty}^{\infty}P_i(t)dt} \tag{3.10}$$

where P_i(t) is the incident power

$$P_i(t) = I_{00}\frac{\pi w_0^2}{2}e^{-(\frac{t}{\tau_p})^2} \tag{3.11}$$

and S is the linear transmittance of the aperture,

$$S = 1 - e^{-2(\frac{r_a}{w_a})^2} \tag{3.12}$$

Under the approximation of small refractive change ($\left|\Delta\Phi_0\right| < \pi$) and S<<1, the normalized energy transmittance in closed-aperture Z-scan can be written as [3.5]:

$$T_{CA}(z) \approx 1 + \frac{4x\left\langle\Delta\Phi_0\right\rangle}{(1+x^2)(9+x^2)} \tag{3.13}$$

where $x = z/z_0, z_0 = \pi w_0^2/\lambda$.

A useful feature of the obtained Z-scan trace is the Z distance between the peak

and valley, ΔZ_{p-v}. For a closed-aperture Z-scan on a third-order nonlinear materials, ΔZ_{p-v} is derived from Equation (3.13):

$$\left|\Delta Z_{p-v}\right| \approx 1.71 \cdot z_0 \tag{3.14}$$

Being independent of the irradiance, this formula is quite helpful in estimating the diffraction length z_0 and hence the minimum beam waist w_0. Another useful formula derived from Equation (3.13) is to determine the nonlinear refractive index n_2 through the transmittance difference, ΔT_{p-v}, between the peak and the valley in a standard closed aperture Z-scan:

$$\Delta T_{p-v} \approx 0.406(1-S)^{0.25}\left\langle \Delta\Phi_0 \right\rangle \tag{3.15}$$

where $\left\langle \Delta\Phi_0 \right\rangle = \Delta\Phi_0 / \sqrt{2}$, $\Delta\Phi_0 = kn_2 I_{00} L_{eff}$, I_{00} is the on-axis peak intensity at the focal plane, which can be expressed as a function of pulse energy ε_i, t_{FWHM} is the full width at half maximum of the pulses, $I_{00} = 4\sqrt{\ln 2}\varepsilon_i / (\sqrt{\pi} \cdot \pi \cdot w_0^2 \cdot t_{FWHM})$, then the nonlinear index coefficient is determined by

$$n_2 = 0.38 \cdot \frac{\lambda w_0^2}{L_{eff}} \cdot \frac{t_{FWHM}}{\varepsilon_i} \cdot \left\langle \Delta\Phi_0 \right\rangle \tag{3.16}$$

From Equations (3.15) and (3.16), it is convenient to make a quick estimation of the magnitude of the nonlinear refractive index.

As mentioned above, the pure third-order nonlinear refraction of material can be detected using CA Z-scan technique. However, when the material exhibits nonlinear absorption properties, the open-aperture (OA) Z-scan technique needs to be performed. In the OA Z-scan technique, the linear transmittance of the aperture is kept 100%. The transmitted energy is completely collected and measured. In the theory analysis, the transmitted energy can be calculated by integrating the electric field at

the exit face of the sample as expressed in Equation (3.8).

3.2.3 Open-aperture Z-scan technique and data analysis

In the open-aperture Z-scan technique, the beam transmitted through the sample was totally collected and thus the pure nonlinear absorption of the sample can be measured. For the nonlinear absorption, material satisfies the attenuate equation,

$$\frac{dI}{dz'} = -(\alpha_0 + \alpha_2 I)I \tag{3.17}$$

where α_0, α_2 are the linear absorption and two-photon absorption coefficient. Integrating Equation (3.17) over z', we obtain the irradiance at the exit surface of the sample as follows [3.4, 3.6]:

$$I_e(z,r,t) = \frac{(1-R)^2 I_i(z,r,t)e^{-\alpha_0 L}}{1+q(z,r,t)} \tag{3.18}$$

where $q(z,r,t) = (1-R)\alpha_2 I_i(z,r,t)L_{eff}$, $L_{eff} = (1-e^{-\alpha_0 L})/\alpha_0$, R is the reflection from the interface, L is the sample thickness, incident beam intensity I_i (z,r,t) can be expressed as,

$$(1-R)I_i(z,r,t) = I_0(z)\exp[-2r^2/w^2(z)]\exp[-(t/t_0)^2] \tag{3.19}$$

where $I_0(z) = I_{00}/(1+z^2/z_0^2)$, $w^2(z) = w_0^2(1+z^2/z_0^2)$, $z_0 = \pi w_0^2/\lambda$, w_0 is the minimum beam waist at the focal plane.

The normalized energy transmittance can be obtained by integrating Equation (3.18) over the space and temporal Gaussian pulses. The result is expressed as [3.4, 3.6],

$$T_{OA}(z) = \frac{1}{\pi^{1/2} q_0}\int_{-\infty}^{\infty} \ln[1+q_0\exp(-x^2)]dx \tag{3.20}$$

where $q_0 = \alpha_2 I_0 L_{eff}$, $L_{eff} = (1-e^{-\alpha_0 L})/\alpha_0$.

Figure 3.3 shows the open-aperture Z-scan trances of the standard sample ZnSe bulk material, which is often used as a standard sample to calibrate the Z-scan set-up.

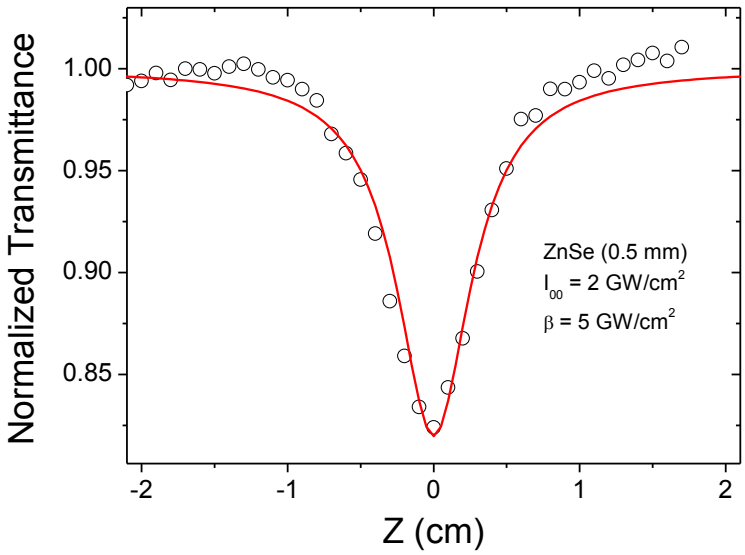

Figure 3.3. The open-aperture Z-scan trance of 0.5-mm ZnSe bulk material.

3.2.4 Open-aperture Z-scan theory for saturable absorption

For the beam propagation in a thin homogeneous broadening saturable absorber, the optical intensity loss is governed by the following differential equation:

$$dI / dz' = -f(I) = -\alpha(I)I = -\alpha_0 I /(1 + I / I_s) \tag{3.21}$$

In general, it is difficult to give explicit analytical solutions of the optical intensity transmitted through the saturable absorption material with a length of L. However, it can be calculated on the basis of the AD method [3.7, 3.8].

Equation (3.21) can be integrated formally

$$I^{out} = I^{in} - \int_0^L f(I)dz' \tag{3.22}$$

where I^{in} is the input optical intensity at the entrance face of the saturable absorber.

On the basis of the AD method, the solutions of I^{out} can be always expressed in terms of the polynomial, as follows

$$I^{out} = \sum_{m=0}^{\infty} u_m \tag{3.23}$$

and the nonlinear term by an infinite series of Adomian's polynomials

$$f(I) = \sum_{m=0}^{\infty} A_m(u_0, u_1, ..., u_m, ...) \tag{3.24}$$

where A_m polynomials is defined by

$$A_m = \frac{1}{m!}[\frac{d^m}{d\zeta^m} f(\sum_{k=0}^{m} \zeta^k u_k)]\Big|_{\zeta=0} \tag{3.25}$$

where ζ is an intermediate variable.

Substituting (3.23) and (3.24) into (3.22) gives

$$\sum_{m=0}^{\infty} u_m = I^{in} - \int_0^L \sum_{m=0}^{\infty} A_m dz' \tag{3.26}$$

Identifying the zeroth component $u_0 = I^{in}$, one gets u_{m} by the recurrence formula as follows:

$$u_{m+1} = -\int_0^L A_m dz' = -\frac{L}{(m+1)!}[\frac{d^m}{d\zeta^m} f(\sum_{k=0}^{m} \zeta^k u_k)]\Big|_{\zeta=0} \tag{3.27}$$

It is obvious that once u_0 is known, all u_m can be given by Equation (3.27). With this procedure, one can easily build the exact solution of the problem $I^{out} = \sum_{m=0}^{\infty} u_m$.

According to Equation (3.27), the exact solution of I^{out} in a series form is given by

$$I^{out} = I^{in}[1 + \sum_{m=1}^{\infty} \frac{(-\alpha_0 L)^m}{m!}] \frac{g_m(\eta)}{(1+\eta)^{2m-1}}] \tag{3.28}$$

where $\eta = I^{in} / I_s$. The first five terms of $g_m(\eta)$ are obtained as follows:

$$\begin{aligned} g_1(\eta) &= 1, \\ g_2(\eta) &= 1, \\ g_3(\eta) &= 1-2\eta, \\ g_4(\eta) &= 1-8\eta+6\eta^2, \\ g_5(\eta) &= 1-22\eta+58\eta^2-24\eta^3 \end{aligned} \tag{3.29}$$

For the Gaussian beam,

$$I^{in}(z,r,t) = [I_{00}/(1+z^2/z_0^2)]\exp[\frac{-2r^2}{w_0^2(1+z^2/z_0^2)}]\exp[-t^2/t_0^2] \tag{3.30}$$

Then the transmittance as a function of sample position *z* can be get by,

$$T(z) = \frac{\int_0^\infty I^{out}(z,r,t)rdrdt}{e^{-\alpha_0 L}\int_0^\infty I^{in}(z,r,t)rdrdt} \tag{3.31}$$

By fitting the Z-scan experiment data with the Equation (3.31), the characteristic parameter of saturable absorber I_s can be extracted.

3.2.5 Open-aperture Z-scan theory for material with saturble absorption and two-photon absorption

As many materials exhibit both saturable absorption (SA) and two-photon absorption (TPA) [3.9-3.12], the study of the Z-scan theory of the materials with saturable absorption and two-photon absorption can facilitate the full understanding of the nonlinear optical properties of these materials.

As laser beam propagates through the materials, the optical intensity loss is governed by the following differential equation:

$$dI/dz' = -f(I) = -\alpha(I)I = -[\alpha_0/(1+I/I_s)+\beta I]\cdot I \tag{3.32}$$

Similar to the pure saturable absorption materials, the solution of Equation (3.32) can be obtained by using the AD method. The analytical solution of the normalized

power transmittance dependent on the sample relative position *z* is deduced [3.13].

$$T(x,t)=\exp(\alpha_0 L)[1+\sum_{m=1}^{\infty}\frac{(-\alpha_0 L)^m}{m!}q_m(\rho)+\sum_{m=1}^{\infty}\frac{(-\beta L I_s)^m}{m!}q'_m(\rho)] \qquad (3.33)$$

where $x=z/z_0$, $\rho=I_0(t)/[I_s(1+x^2)]$. $I_0(t)=I_{00}\exp(-t^2/t_0^2)$ represents Gaussian temporal profile of the laser pulses, and I_{00} is the on-axis peak intensity. The first two terms of $q_m(\rho)$ and $q'_m(\rho)$ are showed:

$$\begin{aligned} q_1(\rho)&=\ln(1+\rho)/\rho,\\ q_2(\rho)&=\frac{-\frac{\alpha_0}{2(1+\rho)^2}+2\beta I_s(\rho-\ln(1+\rho))}{\alpha_0\rho},\\ q'_1(\rho)&=\rho/2,\\ q'_2(\rho)&=\frac{\frac{\alpha_0}{1+\rho}+\alpha_0\ln(1+\rho)}{\beta I_s\rho}+\frac{2\rho^2}{3}. \end{aligned} \qquad (3.34)$$

The normalized energy transmittance for a temporal Gaussian pulse can be yielded by

$$T(x)=\pi^{-1/2}\int_{-\infty}^{\infty}T(x,t)\exp(-t^2/\tau^2)dt \qquad (3.35)$$

As shown in Figure 3.4, the open aperture Z-scan traces of a thin sample, which exhibits saturable absorption and two-photon absorption. The parameters used for simulating are I_{00} = 0.011, 0.024, 0.041 and 0.065 GW/cm^2, respectively, when α_0= 1.43 cm^{-1}, L=0.2 cm, I_s = 0.0011 GW/cm^2, β = 32 cm/GW.

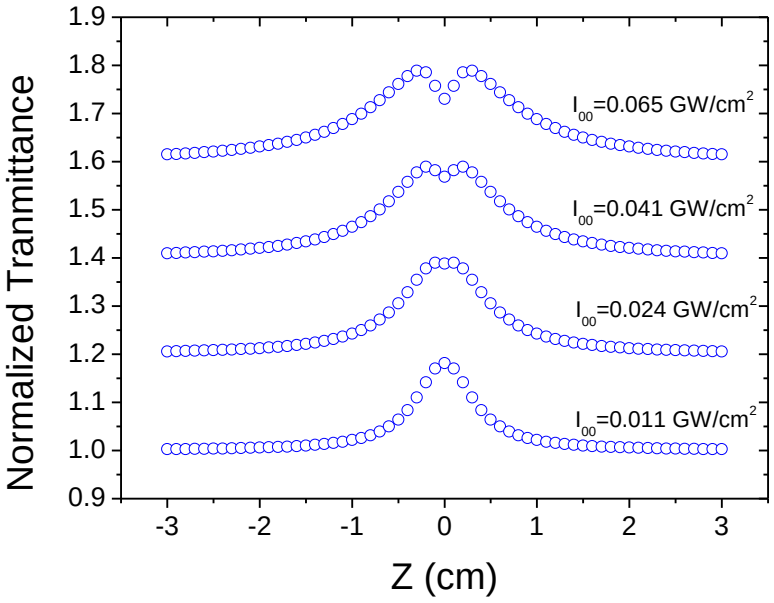

Figure 3.4. The simulated open aperture Z-scan traces of materials with saturable absorption and two-photon absorption (with parameters given in the text).

3.3 Pump-probe experiment technique and data analysis

Pump-probe experiment is another important technique used to gain the understanding of nonlinear optical properties of materials. In the pump-probe experiment, the pump and probe beam are overlapped in the sample. The intensity of the probe beam is much weaker than the pump beam ($I_{probe}/I_{pump} < 1/10$), such that the nonlinear optical effect induced by the probe beam can be ignored. The pump and probe pulses are delayed by a delay line in the experiment set-up. The photo-excited carrier dynamics can manifest itself in the measured transient transmittance or reflectance of the probe beam.

Figure 3.5 shows the schematic diagram of the pump-probe experimental set-up. As can be seen, the laser pulses are firstly divided by a beam splitter into two parts.

One part is the stronger beam, which is called pump beam, and it is delayed and chopped before being focused into the sample. The pump beam is blocked after transmits the sample. Another part is the weaker beam (probe beam), which is focused to the sample and its transmitted light is detected by a sensitive photodiode. In the pump-probe experiment, the temporal profile of photo-excited carrier relaxation dynamics is detected by a time delay between the pump and probe pulses. In order to detect the minimal signal of the transmittance change of the probe beam, the pump beam is chopped in a frequency (such as 600 Hz), which is outside the range of the background noise frequency. Then the transient transmittance of the probe beam is modulated by this certain frequency. Lock-in amplifier is used to pick up the signal of the transient transmittance difference of the probe beam with this frequency. A zero-order λ/2 wave plate as well as a linear polarizer is inserted in the optical path of the probe beam to make the polarization of the probe beam to be perpendicular with the pump light. When the pump and probe beam are cross-polarized, signals from any coherent effects can be eliminated. The pump intensity can be adjusted by a series of neutral density filter to study the pump-intensity dependence of material's nonlinear response.

The probe beam can be white light continuum to detect the transient absorbance in a wide spectrum range. When the wavelengths of the pump and the probe are the same, it is called degenerate pump-probe technique. In this thesis, we used the degenerate pump-probe technique.

Degenerate pump-probe technique is useful to detect the photo-excited carrier

dynamics, the nonlinear optical absorption, and nonlinear refraction properties [3.14].

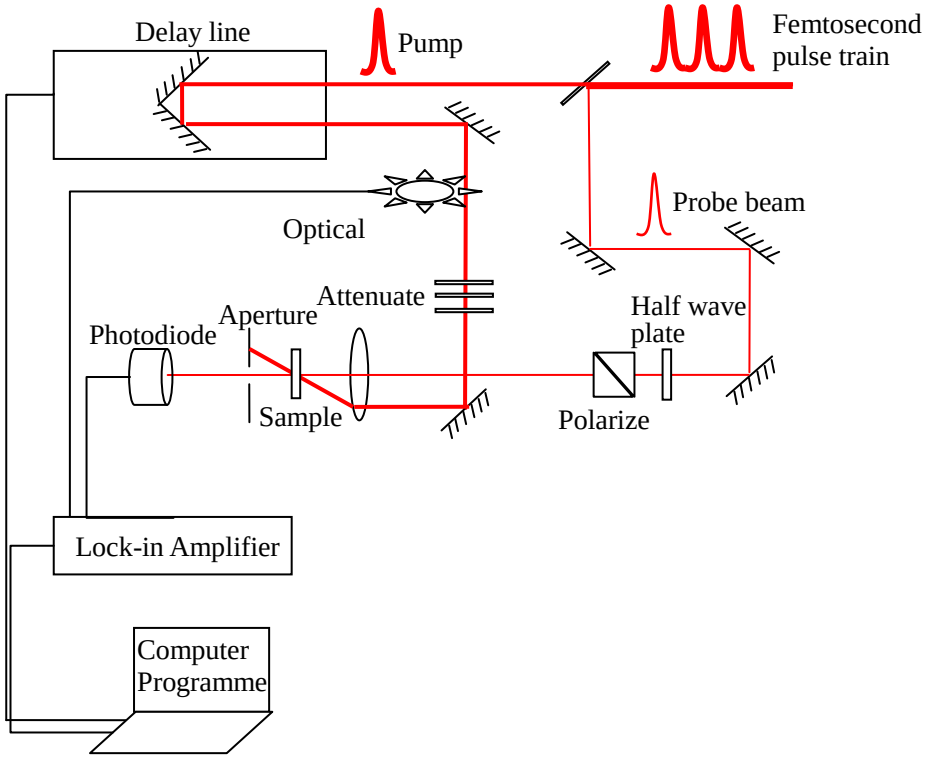

Figure 3.5. Sketch of pump-probe experiment set-up.

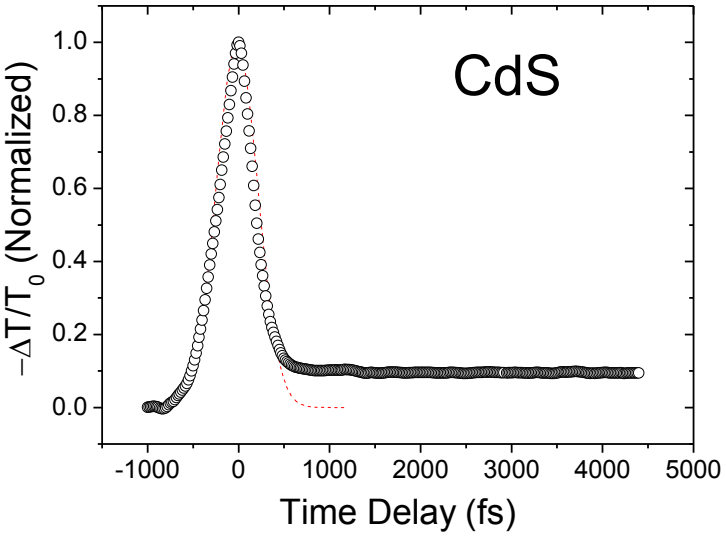

Figure 3.6. Pump-probe experiment signal of the standard sample 0.5-mm CdS bulk material. The slower relaxation dynamics is due to the two-photon absorption induced free carrier absorption. The red dashed line is the fitting with Gaussian function.

The pump-probe experiment is also important in detecting the nonlinear optical absorption properties. When the time delay between pump and probe beam is zero, the overlap of pump and probe in space and time in the sample can be used to detect the nonlinear optical properties of the material. For a sample with both saturable absorption and two-photon absorption, the pump-probe signal can be theoretically simulated as follows.

The differential propagation equation of the pump and probe beam can be expressed as [3.15],

$$\frac{dI_{pu}}{dz} = -\frac{\alpha_0}{1+I_{pu}/I_s} I_{pu} - \beta I_{pu}^2 - 2\beta I_{pu} I_{pr} \tag{3.36}$$

$$\frac{dI_{pr}}{dz} = -\frac{\alpha_0}{1+I_{pu}/I_s} I_{pr} - 2\beta I_{pr} I_{pu} - \beta I_{pr}^2 \tag{3.37}$$

When the probe's delay relative to the pump is τ, then

$$I_{pu}(z,r,t) = I_{pu}(z)\exp(-2r^2/w_0^2)\exp[-(t/\tau_p)^2] \tag{3.38}$$

$$I_{pr}(z,r,t) = I_{pr}(z)\exp(-2r^2/w_0^2)\exp[-(t+\tau)^2/\tau_p^2] \tag{3.39}$$

The transmitted energy of probe beam with pump perturbation is

$$E_{pr} = \int_{-\infty}^{\infty} dt \int_0^{\infty} I_{pr}(L) 2\pi r dr \tag{3.40}$$

The transmitted energy of probe beam without the disturbance of pump beam should be:

$$E_{pr}(0) = \int_{-\infty}^{\infty} dt \int_0^{\infty} I_{pr}(0) 2\pi r dr \tag{3.41}$$

Normalized Differential Transmitted Energy (NDTE) of the probe beam is given by

$$NDTE(\tau_D) = \frac{E_{pr} - E_{pr}(0)}{E_{pr}(0)} \tag{3.42}$$

By fitting the above solution to the experimentally measured data, one can extract both the saturation intensity (I_s) and the two-photon absorption coefficient (β).

3.4 The femtosecond laser systems

In this thesis, the experiments were performed with two femtosecond laser systems. The first one was the Quantronix femtosecond laser system which includes three parts: (1) a pump laser (Qantronix, Darwin) at 527 nm, which has a pulse duration of 150 ns, and a repetition rate of 1kHz); (2) an amplifier laser: Ti:Sapphire regenerative amplifier (Quantronix, Titan), with the oscillator inside and being pumped by the Darwin laser. The output is at 780 nm with a repetition rate of 1 kHz, the full width at e^{-1} maximum pulse width is around 400 fs; and (3) an optical parametric amplifier (Quantronix, TOPAS) pumped by the Ti:Sapphire regenerative amplifier (Quantronix, Titan) at 1-kHz repetition rate. The TOPAS generates the tunable wavelength laser pulses from 500 nm to 1550 nm.

The second femtosecond laser system is composed of the Coherent regenerative amplifier (Coherent Legend, 780 nm, 100 fs, 1 kHz) and the optical parametric amplifier (Coherent TOPAZ).

References

[3.1] S. R. Friberg, and P. W. Smith, "Nonlinear optical-glasses for ultrafast optical switches," IEEE J. Quantum Elect., **23,** 2089-2094 (1987).

[3.2] A. Owyoung, "Ellipse rotation studies in laser host materials," IEEE J. Quantum Elect., **9,** 1064-1069 (1973).

[3.3] W. E. Williams, M. J. Soileau, and E. W. Van Stryland, "Optical switching and n_2 measurements in CS_2," Opt. Commun., **50,** 256-260 (1984).

[3.4] M. Sheikbahae, A. A. Said, T. H. Wei *et al.*, "Sensitive measurement of optical nonlinearities using a single beam," IEEE J. Quantum Elect., **26,** 760-769 (1990).

[3.5] M. Dinu, F. Quochi, and H. Garcia, "Third-order nonlinearities in silicon at telecom wavelengths," Appl. Phys. Lett., **82,** 2954-2956 (2003).

[3.6] J. He, Y. Qu, H. Li *et al.*, "Three-photon absorption in ZnO and ZnS crystals," Opt. Express, **13,** 9235-9247 (2005).

[3.7] A. G, "A review of the decomposition method in applied mathematics," J. Math. Anal. Appl., **135,** 501-544 (1988).

[3.8] B. Gu, Y. X. Fan, J. Wang *et al.*, "Characterization of saturable absorbers using an open-aperture Gaussian-beam Z scan," Phys. Rev. A, **73,** 065803 (2006).

[3.9] S. Venugopal Rao, N. K. M. Naga Srinivas, and D. Narayana Rao, "Nonlinear absorption and excited state dynamics in Rhodamine B studied using Z-scan and degenerate four wave mixing techniques," Chem. Phys.

Lett., **361,** 439-445 (2002).

[3.10] Y. Gao, X. Zhang, Y. Li *et al.*, "Saturable absorption and reverse saturable absorption in platinum nanoparticles," Opt. Commun., **251,** 429-433 (2005).

[3.11] T. Cassano, R. Tommasi, A. P. Meacham *et al.*, "Investigation of the excited-state absorption of a Ru dioxolene complex by the Z-scan technique," J. Chem. Phys., **122,** 154507-6 (2005).

[3.12] M. Joschko, P. Langlois, E. R. Thoen *et al.*, "Ultrafast hot-carrier dynamics in semiconductor saturable absorber mirrors," Appl. Phys. Lett., **76,** 1383-1385 (2000).

[3.13] J. Wang, B. Gu, H. T. Wang *et al.*, "Z-scan analytical theory for material with saturable absorption and two-photon absorption," Opt. Commun., **283,** 3525-3528 (2010).

[3.14] A. Dogariu, T. Xia, D. J. Hagan *et al.*, "Purely refractive transient energy transfer by stimulated Rayleigh-wing scattering," J. Opt. Soc. Am. B, **14,** 796-803 (1997).

[3.15] R.L. Sutherland, S. Kirkpatrick, D.G. Mclean, Handbook of Nonlinear Optics, 2nd ed.; Marcel Dekker: New York, 2003.

Chapter 4

Saturable absorption in graphene

4.1 Introduction

Graphene, as a two-dimensional semi-metal material, possesses a linear dispersion for its energy-momentum relation near the Dirac point [4.1, 4.2]. The linear and nonlinear optical properties of graphene have received intensive attention due to the unique electronic structure [4.3-4.34]. Graphene has been demonstrated to be an ideal saturable absorber for generating ultrashort laser pulses, as it shows lower insertion loss, larger modulation depth and lower saturation intensity [4.21].

The saturation intensity is defined as the light intensity at which, the intrinsic absorption coefficient drops to half of its original value. The saturation intensity is an important parameter in determining the performance of a saturable absorber. The saturation intensity of graphene has been studied intensely [4.21-4.28]. However, due to different measurement conditions and variation in synthesizing methods, there is a large discrepancy in the reports of the saturation intensity of graphene. The saturation intensity of CVD graphene was firstly studied by the nonlinear transmittance measurements with ultrafast laser pulses at 1550 nm [4.21]. The pulse width and repetition rate were 1 ps and 100 MHz, respectively. The saturation intensity of 2-4 layer CVD graphene was reported to be 0.71 MW/cm^2. In a following study, the saturation intensity of graphene fabricated using wet-chemistry techniques was measured by the nonlinear transmittance with ultrafast laser pulses at 1558 nm with

pulse duration and repetition rate of 0.58 ps and 38.83 MHz [4.23]. The saturation intensity of the chemically synthesized graphene was measured to be 266 MW/cm^2, which is much higher than the previous report of the CVD-grown graphene. Recently, the saturation intensity of exfoliated graphene was studied by depositing the exfoliated graphene flakes on a fiber core [4.26]. The nonlinear transmittance was measured with ultrafast laser pulses at 1550 nm with pulse duration of 500 fs and repetition rate of 50 MHz. The saturation intensities of 8, 13, 30 layer graphene were measured to be 90 MW/cm^2, 350 MW/cm^2, and 380 MW/cm^2, respectively. This value is of the same order with the report of the chemically synthesized graphene. Besides, the saturable absorption of epitaxial graphene has been studied intensely due to its large scale, high quality and uniformity. The saturation intensity of epitaxial graphene was measured to be 4 GW/cm^2 at 800 nm using Z-scan technique [4.22]. This saturation intensity is one order higher than the report of exfoliated graphene at 1550 nm, which could result from different operating wavelength, as predicted theoretically by Vasko [4.32].

Apart from the quality of graphene samples (that is varying from one synthesis method from the other), the saturation intensity of graphene can also be influenced by the operating wavelength [4.32]. It has been predicted by Vasko that the interband saturable absorption of graphene is sensitive to the operating wavelength [4.32]. And it has been experimentally measured in the near infrared spectral range [4.13-4.28]. However, a systematical study on the spectral dependence of saturable absorption of graphene has not been reported yet. The spectral dependence of saturable absorption

is desirable for both fundamental studies and applications. The study will give a deep understanding of the mechanism of saturable absorption in graphene and facilitate the applications of graphene as saturable absorber in a wide spectrum range.

In this chapter, we report a systematical measurement of saturable absorption by carrying out Z-scan experiments on monolayer, bilayer and 6-layer epitaxial graphene in a spectral range from 780 nm to 1100 nm with femtosecond laser pulses. This chapter is organized in the following manner. Sections 4.2 and 4.3 present both theoretical description of saturable absorption and special considerations in the Z-scan measurements on our graphene samples, respectively. Sections 4.4 and 4.5 present our open-aperture Z-scans on epitaxial graphene. Section 4.6 details a comparison with carbon nanotubes, followed by a summary in Section 4.7.

4.2 Propagation of light through graphene

When the light propagates through graphene, the Maxwell equation can be written as [4.35],

$$\nabla^2\mathbf{E} - \mu\sigma\frac{\partial\mathbf{E}}{\partial t} - \mu\varepsilon\frac{\partial^2\mathbf{E}}{\partial t^2} = 0 \tag{4.1}$$

where σ is the optical conductivity, μ is the magnetic permeability, ε is electric permittivity.

If we assume the electromagnetic field is in the form, $\mathbf{E}(\mathbf{r},t) = \mathbf{E}_0 e^{i(\mathbf{k}\cdot\mathbf{r}-\omega t)}$, we can get the expression of the wave vector as,

$$-k^2 + i\cdot\omega\mu\sigma + \omega^2\mu\varepsilon = 0 \tag{4.2}$$

where $k = \omega\cdot(n+i\kappa)/c$, ω is the optical frequency, n and κ are the real and

imaginary part of the complex refractive index of graphene, ε and σ are the complex dielectric constant and photoconductivity of the medium, respectively. Thus, we can get the expression of the imaginary part of the wave propagator as [4.35],

$$\kappa = \frac{1}{2n}[\frac{1}{\omega\varepsilon_0}\mathrm{Re}(\sigma) + \mathrm{Im}(\chi^{(1)})] \tag{4.3}$$

where ε_0 is the permittivity in the free space, $\chi^{(1)}$ denotes the linear susceptibility. Thus, the absorption coefficient of the medium can be expressed as [4.35],

$$\alpha(\omega) = \frac{\omega[\mathrm{Im}(\chi^{(1)}) + \mathrm{Re}(\sigma)/\varepsilon_0\omega]}{n(\omega)c} \tag{4.4}$$

In a conductive material such as graphene, we may assume that the conductive current density is much greater than the displacement current density. We can get the expression in this material as,

$$\alpha(\omega) = \frac{\omega[\mathrm{Re}(\sigma)/\varepsilon_0\omega]}{n(\omega)c} \tag{4.5}$$

Due to the linear dispersion relation near the Fermi level, the optical conductivity of intrinsic graphene exhibits a frequency-independent value of $\sigma = e^2/(4\hbar)$ [4.10]. However, a more practical expression for graphene has been derived by considering the local sample environment [4.6],

$$\sigma_{\mathrm{inter}}(\omega) = i\frac{e^2\omega}{\pi}\int_0^\infty dE\,\frac{1}{(2E)^2 - (\hbar\omega + i\Gamma)^2}\cdot[f(E - E_f^c) - f(-E - E_f^v)] \tag{4.6}$$

$$\sigma_{\mathrm{intra}}(\omega) = i\frac{e^2/\pi\hbar^2}{\omega + i/\tau}\int_0^\infty dE[f(E - E_f^c) + f(-E - E_f^v)] \tag{4.7}$$

where e is the electron charge, $\hbar\omega$ is the photon energy, f $(E\text{-}E_f^{c/v})$ $=1/(1+\exp[(E\text{-}E_f)/k_bT_e]$ is the Fermi distribution function, $E_f{}^{c/v}$ is the Fermi energy in the conduction/valence band, Γ describes the broadening of the interband transitions,

k_b is the Boltzmann constant, T_e is the electronic temperature, and τ is the intra-momentum relaxation time due to carrier-carrier scattering.

From Equations (4.6) and (4.7), it is found that the photoconductivity is a function of Fermi levels of graphene. When graphene is under intense irradiance, more electrons and holes are generated. As a consequence, the Fermi levels are altered, giving rise to a decrease in the optical conductivity via Equation (4.6), which is so called 'band-filling' effect. The decrease in the optical photoconductivity then leads to saturable absorption in graphene [4.13].

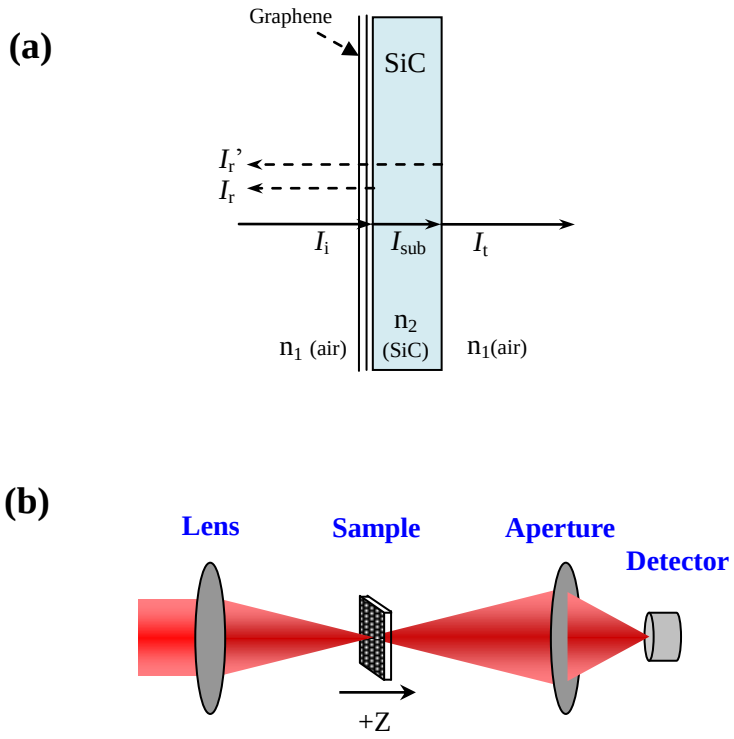

Figure 4.1. (a) Geometry of light scattering between two media (air and SiC) with graphene separating them. (b) Sketch of open aperture Z-scan experiment set-up.

4.3 Special considerations for open-aperture Z-scan on graphene/SiC samples

As introduced in Chapter 3, open-aperture Z-scan experiment is a sensitive method of measuring material's nonlinear optical absorption. As sketched in Figure 4.1, a single beam is normally incident on the epitaxial graphene sample, and the transmitted beam is totally collected by a convex lens and measured by a photo detector. For the saturable absorption of graphene, we assume that the saturable absorption can be quantified by a classical expression: $\alpha = \alpha_0/(1+I/I_s)$, where α_0 is the linear absorption coefficient and I_s is the saturation intensity. Then the light intensity within the graphene is governed by the following differential equation [4.22, 4.32],

$$\frac{dI}{dz'} = -\frac{\alpha_0}{1+I/I_s}\cdot I \tag{4.8}$$

The magnitude of α_0 for monolayer graphene has been well understood and documented [4.3. 4.4].

The transmitted intensity through graphene sample can be expressed by the integration,

$$I_G^{out} = I^{in} - \int_0^L \frac{\alpha_0 I}{1+I/I_s}dz' \tag{4.9}$$

where L is the thickness of graphene sample, $L = n\,l$, n is the number of graphene layers, l (l = 0.335 nm) is the thickness of monolayer graphene. z' and I^{in} is the propagation distance and intensity in graphene sample. For the Gaussian beam, $I^{in} = [I_{00}/(1+x^2)]\exp[-2r^2/\omega^2(x)]\exp[-t^2/t_0^2]$, where I_{00} is the on-axis peak intensity at focal plane; $x = z/z_0$ is the sample relative position in the Z-scan experiment; z is the sample

position; $w^2(x) = w_0^2(1+x^2)$, w_0 and $z_0 = \pi w_0^2/\lambda$ are the radius of the beam waist and the Rayleigh length, respectively. Equation (4.9) can be solved by using AD method, which has been discussed in detail in Chapter 3.

It should be pointed that the epitaxial graphene is on SiC substrate whose influence on the totally measured transmitted intensity is given by,

$$I_t = I_G^{out} \cdot (1 - R_{air/G-SiC}) \cdot (1 - R_{SiC/air}) \tag{4.10}$$

where $R_{\text{air/G-SiC}}$ is the reflection from the front interface (air/graphene-SiC), $R_{\text{SiC/air}}$ is the reflection from the rear interface (SiC/air). As the reflection of free-standing graphene has been measured to be <0.1%, which is negligible [4.3, 4.4]. It is reasonable to assume that $R_{\text{air/G-SiC}} \approx R_{\text{air/SiC}}$.

The normalized transmittance through the epitaxial graphene/SiC sample can be expressed as,

$$\frac{T}{T_0} = \frac{I_t}{I_{t0}} = \frac{I_G^{out}}{I_i \cdot e^{-\alpha_0 L}} \tag{4.11}$$

To fit the experimental Z-scans in which the laser pulse energy is measured, Equation (4.11) is integrated in both space and time for the transmitted laser pulse energy.

4.4 Open-aperture Z-scans in epitaxial graphene at 780 nm

In Figure 4.2 (a), it is the open-aperture Z-scan traces of monolayer, bilayer and 6-layer graphene using femtosecond laser pulses with $I_{00} = 12$ GW/cm^2 (on-axis peak intensity at focal plane). It can be seen that the normalized transmittance increases due to the saturable absorption of graphene, as the sample moves to the focal plane with

higher irradiance. As shown in Figure 4.2 (a), the normalized transmittance increases proportionally as the number of layer increases. The Z-scan data were analyzed with the method introduced above.

The above Z-scan data is the plot of nonlinear signal versus the position of sample (z). It can be converted to the plot of nonlinear optical transmittance versus irradiance by the formula $I_i = I_{00}/(1+z^2/z_0^2)$, where I_i, I_{00} are the on-axis peak intensity at position z and focal plane, respectively, z_0 is the Rayleigh length of the laser beam and is equal to $\pi\omega_0^2/\lambda$. Figure 4.2(b) shows the converted Z-scan data of the graphene samples.

From the best fits between the experimental data and Z-scan theory (see Section 4.3), we extract the saturation intensities. The saturation intensities of the monolayer, bilayer and 6-layer epitaxial graphene are tabulated in Table 4.1. We can see that the saturation intensities of the epitaxial graphene samples do not change significantly, as the number of graphene layers increases from 1 to 6. It indicates that the saturable absorption of graphene can be enhanced by stacking the graphene layers (up to 6 layers in the present measurements).

(a)

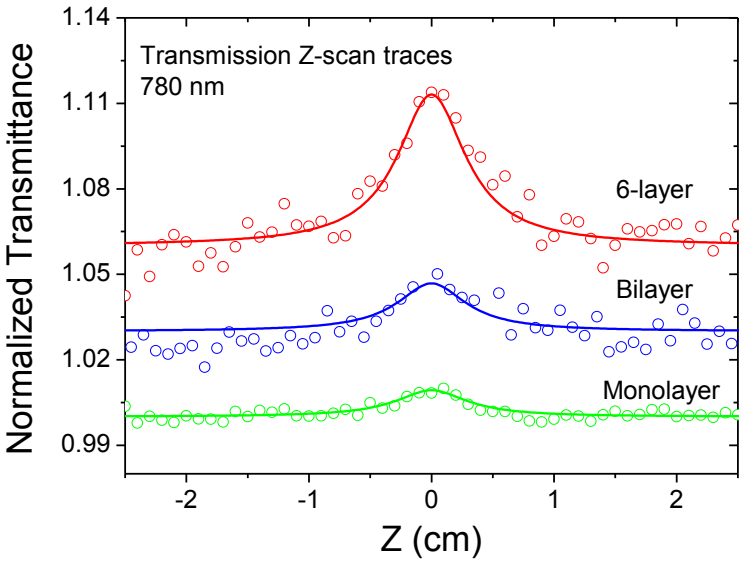

(b)

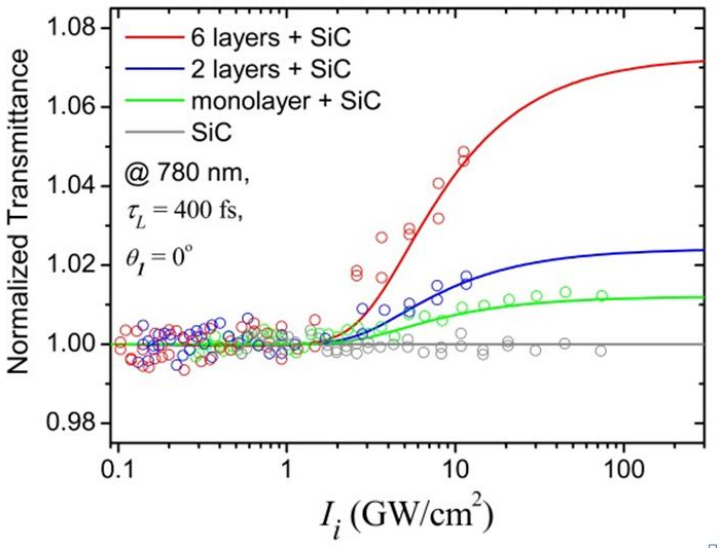

Figure 4.2. (a) Open-aperture transmission Z-scan traces of monolayer, bilayer and 6-layer graphene at 780 nm with femtosecond laser pulses. (b) Normalized transmittance versus incident light irradiance for graphene on SiC substrate at 780 nm, transformed from the original Z-scan data as discussed in the text. The circles are converted from the Z-Scan data, and the curves are the theoretical simulations.

Table 4.1. Measurements of saturation intensity of graphene.

Sample		**Laser**			**I_s**	**References**
Synthesis method	Number of layers	Wavelength (nm)	Pulse width (ps)	Repetition Rate	Experimental (GW/cm^2)	
Epitaxial Graphene	1	780	0.4	1 kHz	6 ±2	Current work
	2				6 ±2	
	6				5 ±2	
Epitaxial Graphene	2	800	0.2	1 kHz	4 ±1	[4.22]
Exfoliated Graphene	8	1550	0.5	50 MHz	0.09	[4.26]
	13				0.35	
	30				0.38	

It should be pointed out that the above Z-scans were conducted with the laser maximum intensity less than the damage threshold. It was reported that the damage threshold of graphene under femtosecond excitation could be as high as ~ 300 GW/cm^2 [4.22, 4.36], which were in agreement with our Z-scan experiment on the epitaxial graphene samples. In order to avoid laser-induced damage and other higher-order nonlinear effects [4.37], we performed Z-scan measurements of bilayer and 6-layer graphene with the irradiance below ~12 GW/cm^2, while for monolayer graphene, the highest irradiance was ~70 GW/cm^2. In the Z-scan experiments, the laser induced damage can be excluded from the symmetry and repeatability of the Z-scan traces, as shown in Figure 4.2 (a) and (b), as the damage of the sample can induce the asymmetry of Z-scan traces [4.38], due to irreversible nature of damage.

4.5 Spectral dependence of saturable absorption in epitaxial graphene

We also performed open-aperture Z-scans in a spectral range (900 nm – 1100 nm) at room temperature. The femtosecond laser pulses were produced from an optical parametric amplifier (Coherent TOPAZ) pumped by another regenerative amplifier (Coherent Legend, 780 nm, 100 fs, 1 kHz). Figure 4.3 (a) shows the Z-scan data at the wavelength of 900 nm, 1000 nm, and 1100 nm with the on-axis peak intensity of 7 GW/cm^2. In these Z-scan traces, the saturable absorption signal (T/T_0) increases as the wavelength increases from 900 nm to 1100 nm. It indicates that graphene is an excellent material as a saturable absorber in the infrared range for optical communication. In Figure 4.3 (b), the original Z-scan data is transformed into the plot of normalized absorption coefficient versus the laser irradiance by the formula, $I_i = I_{00}/(1+z^2/z_0^2)$, $z_0 = \pi w_0^2/\lambda$. The normalized absorption coefficient is transformed from the nonlinear transmittance by the formula, $T/T_0 = e^{-l\cdot(\alpha-\alpha_0)}$. As shown in Figure 4.3 (b), it is found that the saturation intensity (I_s) decreases from 5(±2) GW/cm^2 at 900 nm to 1.5(±0.5) GW/cm^2 at 1100 nm. The experimental findings are consistent with the theoretical predictions by Vasko [4.32]. The study of spectral dependence of saturable absorption of graphene should facilitate the applications of graphene as an ultrafast saturable absorber in this spectral region. The experimental findings of our study are compared with the reports from other groups, as shown in Table 4.2.

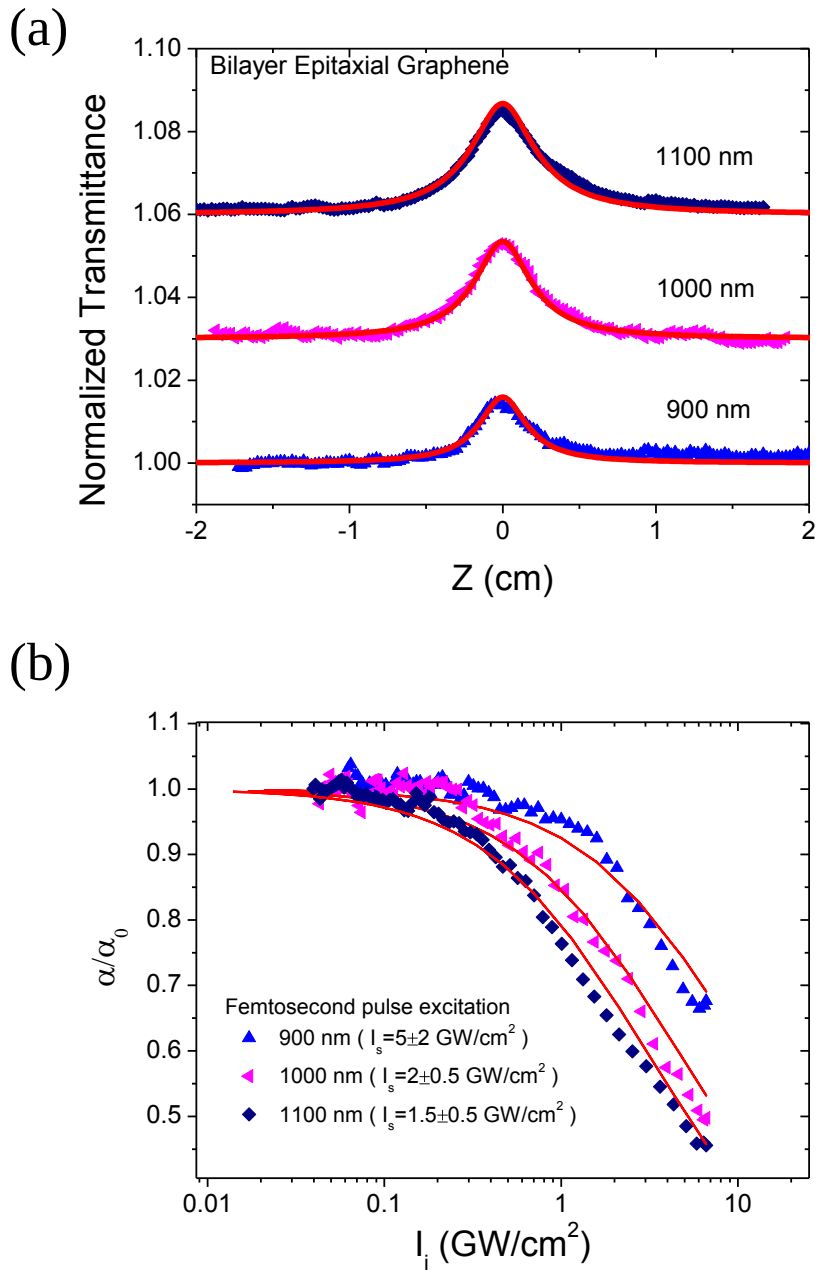

Figure 4.3. The spectral dependence of saturable absorption of graphene. (a) Open aperture Z-scan trances at 900 nm, 1000 nm and 1100 nm with femtosecond pulses at repetition rate of 1 kHz and on-axis peak intensity of ~7 GW/cm^2. (b) Normalized absorption coefficient versus irradiance from 900 nm to 1100 nm, transformed from original Z-scan data as discussed in the text.

Table 4.2. Spectral dependence of saturable absorption of graphene.

Sample	**Laser**			**I_s**	**References**
Synthesis method	Wavelength (nm)	Pulse width (ps)	Repetition Rate	Experimental (GW/cm^2)	
Epitaxial Graphene	900	0.2	1 kHz	5 ±2	Current work
	1000			2 ±0.5	
	1100			1.5 ±0.5	
Epitaxial Graphene	800	0.2	1 kHz	4 ±1	[4.22]
Exfoliated Graphene	1550	0.58	38 MHz	0.266	[4.23]
Exfoliated Graphene	1550	0.5	50 MHz	0.09-0.38	[4.26]

4.6 Comparison and discussion

The saturable absorption of graphene has been studied intensely due to its ultrafast responsibility, large nonlinear susceptibility and modulation depth. The saturable absorption of graphene has been measured with the techniques such as, measurement of nonlinear transmittance (also called, direct measurement), Z-scan, and pump-probe techniques. The graphene samples studied in the previous reports include exfoliated graphene, epitaxial graphene, CVD graphene, and chemically synthesized graphene. Besides, the theoretical studies of saturable absorption of graphene have also attracted much attention [4.31-4.33]. As shown in Table 4.3 and Figure 4.4, we compare our experimental study with reports from other groups. It can be seen that graphene is superior saturable absorber in generating ultrashort pulses in a wide spectral range. As

the wavelength increases, the saturation intensity decreases, which indicates that graphene is especially an excellent saturable absorber in the infrared range. In comparison with graphene samples synthesized by different methods, the saturation intensity of CVD graphene is nearly three orders lower than the value of other graphene samples [4.21]. Such a lower saturation intensity could be induced by the unique characteristic of CVD graphene. It was reported that the mobility of CVD graphene is much lower than that of exfoliated graphene and epitaxial graphene, due to the local electronic corrugations and doped regions in CVD graphene [4.39]. However, it should be pointed out that up to now, no theory is able to predict such a low saturation intensity, further systematic investigations are required.

The saturable absorption of carbon nanotubes (CNT), which is an important allotrope of graphene, has been studied intensely due to its ultrafast recovery time and large third-order optical nonlinearity [4.40-4.43]. Since 2003, CNT-based devices have been designed in multiple configurations [4.43]. Despite the great promise of this material, there are also some drawbacks inherent to their physical properties. The optical absorption of CNTs is related to their chirality and diameter, only the CNTs that are in resonance with the optical wavelength can perform as saturable absorbers while the remaining CNTs are responsible for excess background losses and scattering.

We also investigated the multiwalled carbon nanotubes using Z-scan technique. The MWNTs were grown vertically on the quartz substrate using the Chemical Vapor Deposition (CVD) method [4.44]. Figure 4.5 (b) shows the SEM and TEM images of

the MWNTs with mean diameter of 3 nm. Figure 4.5 (c) shows the absorption spectrum of MWNTs. The broad absorption peak, which centred at 230 nm (5.4 eV) and extended to the infrared regime, originates from the surface Plasmon resonance (SPR) of π-electrons in MWNTs. The saturable absorption is believed to be originated from the saturation of the surface Plasmon absorption at intense laser irradiance. In order to make a comparison between graphene and CNTs, Z-scan experiments on the 6-layer graphene and 2 μm thick MWNT thin film were carried out. As shown in Figure 4.5 (a), we can see that the graphene film shows superior saturable absorption properties with deeper modulation depth of transmittance. The saturation intensity of the graphene film was measured to be ~6 GW/cm^2, much smaller than the value of MWNT, which was measured to be 20 GW/cm^2. The superior behavior of graphene as a saturable absorber, can be attributed to its compact structure, lower saturation intensity and less scattering.

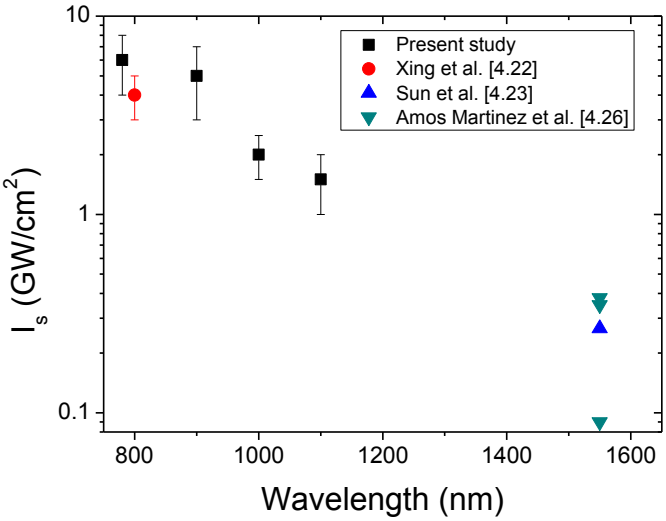

Figure 4.4. Comparison of saturation intensity of graphene.

Table 4.3. Comparison of SA of graphene with reports from other groups.

Sample	**Laser**		**I_s (GW/cm^2)**	**Method**	**References**
Epitaxial Graphene	400 fs, 1kHz, 780 nm		6 ±2	Z-scan	Present study
	200 fs, 1kHz	900 nm	5 ±2		
		1000 nm	2 ±0.5		
		1100 nm	1.5 ±0.5		
CVD	1 ps, 100 MHz,1550 nm		0.0007	Transmittance	[4.21]
Epitaxial Graphene	200 fs, 1 kHz, 800 nm		4	Z-scan	[4.22]
Exfoliate Graphene in PVA polymer	580 fs, ~1550 nm		~0.266	Transmittance	[4.23]
Exfoliate Graphene	500 fs,50 MHz, 1550nm		0.09-0.38	Transmittance	[4.26]
Intrinsic Graphene	0.4 ps, 750 nm		0.6	Theory	[4.32]
	0.6 ps, 1550 nm		0.06		
	1 ps, 10.36 μm		0.0002		
Intrinsic Graphene	800 nm		4	Theory	[4.33]

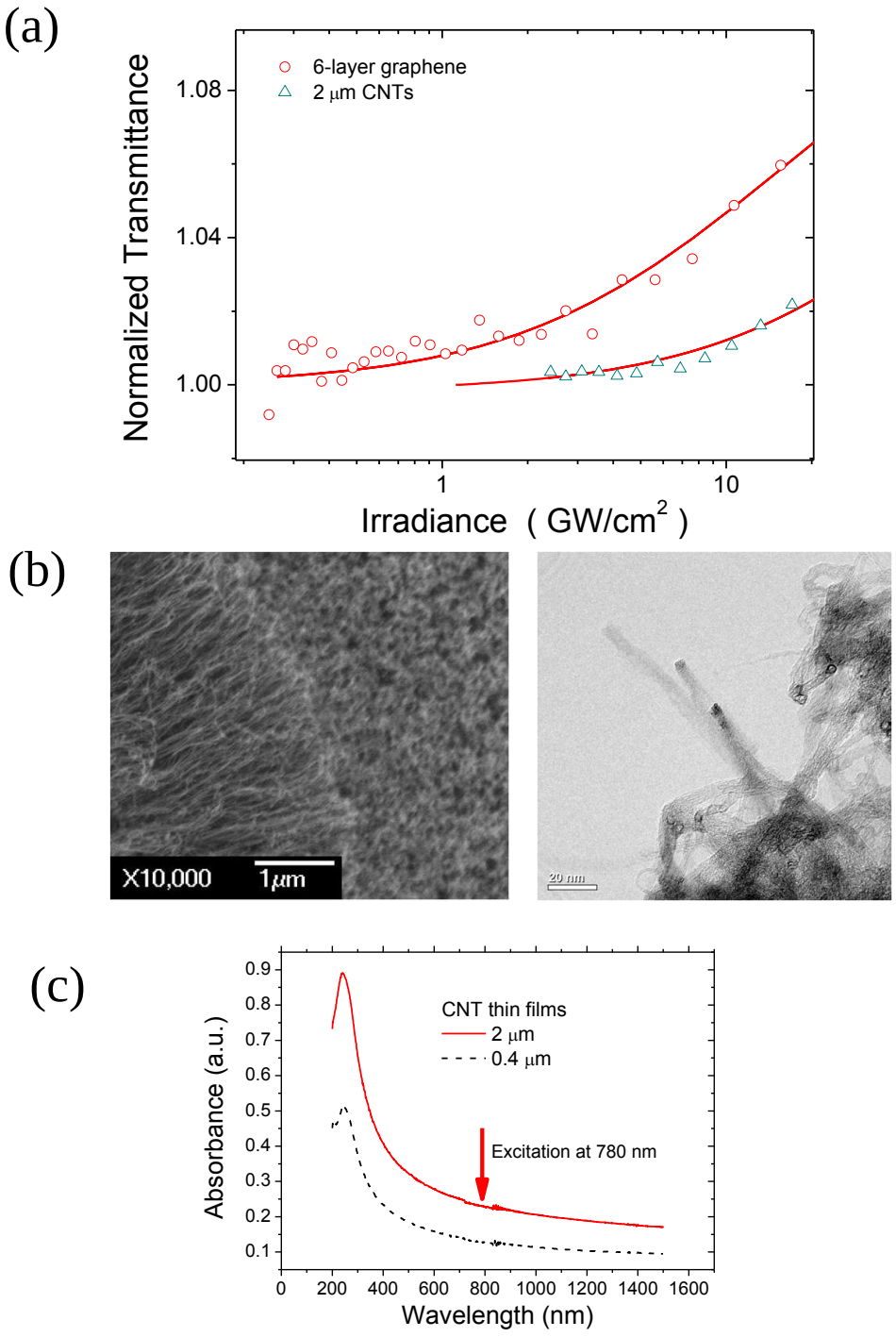

Figure 4.5. Comparison of saturable absorption induced transmittance change of graphene and vertical aligned MWNT thin film on quartz substrate. (a) Modulation of normalized transmittance of the two carbon allotropes. (b) SEM and TEM image of a MWNT thin film (side view). (c) Linear absorption spectra of MWNT films with different length.

4.7 Conclusion

In this chapter, we have systematically studied saturable absorption of epitaxial graphene and its spectral dependence by carrying out open-aperture Z-scan experiments on monolayer, bilayer and 6-layer epitaxial graphene samples with high quality and uniformity. From the Z-scan experiments at 780 nm, the saturation intensity was measured to be ~6(±2) GW/cm^2. We have also determined the spectral dependence of ultrafast saturable aborption of graphene by carrying out TZ-scan experiments on the bilayer graphene in a spectral range (900 nm-1100 nm), which indicates graphene's saturation intensity decrease as the light wavelength increases. Finally, we have compared the saturable absorption of graphene with the reports from other groups and CNTs. It is concluded that graphene behaves superiorly as a saturable absorber due to its large modulation depth, low loss of scattering and ultrafast recovery time.

References

[4.1] K. S. Novoselov, A. K. Geim, S. V. Morozov *et al.*, "Electric field effect in atomically thin carbon films," Science, **306,** 666-669 (2004).

[4.2] A. H. Castro Neto, F. Guinea, N. M. R. Peres *et al.*, "The electronic properties of graphene," Rev. Mod. Phys. , **81,** 109-162 (2009).

[4.3] R. R. Nair, P. Blake, A. N. Grigorenko *et al.*, "Fine structure constant defines visual transparency of graphene," Science, **320,** 1308 (2008).

[4.4] T. Stauber, N. M. R. Peres, and A. K. Geim, "Optical conductivity of graphene in the visible region of the spectrum," Phys. Rev. B, **78,** 085432 (2008).

[4.5] M. Orlita, and M. Potemski, "Dirac electronic states in graphene systems: optical spectroscopy studies," Semicond. Sci. Tech., **25,** 063001 (2010).

[4.6] J. M. Dawlaty, S. Shivaraman, J. Strait *et al.*, "Measurement of the optical absorption spectra of epitaxial graphene from terahertz to visible," Appl. Phys. Lett., **93,** 131905 (2008).

[4.7] L. A. Falkovsky, and S. S. Pershoguba, "Optical far-infrared properties of a graphene monolayer and multilayer," Phys. Rev. B, **76,** 153410 (2007).

[4.8] Z. Q. Li, E. A. Henriksen, Z. Jiang *et al.*, "Dirac charge dynamics in graphene by infrared spectroscopy," Nature Phys., **4,** 532-535 (2008).

[4.9] I. Jung, M. Pelton, R. Piner *et al.*, "Simple approach for high-contrast optical imaging and characterization of graphene-based sheets," Nano Lett., **7,** 3569-3575 (2007).

[4.10] K. F. Mak, M. Y. Sfeir, Y. Wu *et al.*, "Measurement of the optical conductivity of graphene," Phys. Rev. Lett., **101,** 196405 (2008).

[4.11] E. J. Nicol, and J. P. Carbotte, "Optical conductivity of bilayer graphene with and without an asymmetry gap," Phys. Rev. B, **77,** 155409 (2008).

[4.12] Y. Wang, Z. Ni, L. Liu *et al.*, "Stacking-dependent optical conductivity of bilayer graphene," ACS Nano, **4,** 4074-4080 (2010).

[4.13] J. M. Dawlaty, S. Shivaraman, M. Chandrashekhar *et al.*, "Measurement of ultrafast carrier dynamics in epitaxial graphene," Appl. Phys. Lett., **92,** 042116 (2008).

[4.14] P. A. George, J. Strait, J. Dawlaty *et al.*, "Ultrafast optical-pump Terahertz-probe spectroscopy of the carrier relaxation and recombination dynamics in epitaxial graphene," Nano Lett., **8,** 4248-4251 (2008).

[4.15] D. Sun, Z. K. Wu, C. Divin *et al.*, "Ultrafast relaxation of excited dirac fermions in epitaxial graphene using optical differential transmission spectroscopy," Phys. Rev. Lett., **101,** 157402 (2008).

[4.16] L. Huang, G. V. Hartland, L. Q. Chu *et al.*, "Ultrafast transient absorption microscopy studies of carrier dynamics in epitaxial graphene," Nano Lett., **10,** 1308-1313 (2010).

[4.17] M. Breusing, C. Ropers, and T. Elsaesser, "Ultrafast carrier dynamics in graphite," Phys. Rev. Lett., **102,** 086809 (2009).

[4.18] R. W. Newson, J. Dean, B. Schmidt *et al.*, "Ultrafast carrier kinetics in exfoliated graphene and thin graphite films," Opt. Express, **17,** 2326-2333

(2009).

[4.19] P. A. Obraztsov, M. G. Rybin, A. V. Tyurnina *et al.*, "Broadband light-induced absorbance change in multilayer graphene," Nano Lett., **11,** 1540-1545 (2011).

[4.20] J. Shang, T. Yu, J. Lin *et al.*, "Ultrafast electron−optical phonon scattering and quasiparticle lifetime in CVD-grown graphene," ACS Nano, **5,** 3278-3283 (2011).

[4.21] Q. Bao, H. Zhang, Y. Wang *et al.*, "Atomic-layer graphene as a saturable absorber for ultrafast pulsed lasers," Adv. Funct. Mater., **19,** 3077-3083 (2009).

[4.22] G. Xing, H. Guo, X. Zhang *et al.*, "The physics of ultrafast saturable absorption in graphene," Opt. Express, **18,** 4564-4573 (2010).

[4.23] Z. Sun, T. Hasan, F. Torrisi *et al.*, "Graphene mode-locked ultrafast laser," ACS Nano, **4,** 803-810 (2010).

[4.24] A. Martinez, K. Fuse, B. Xu *et al.*, "Optical deposition of graphene and carbon nanotubes in a fiber ferrule for passive mode-locked lasing," Opt. Express, **18,** 23054-23061 (2010).

[4.25] Y. W. Song, S. Y. Jang, W. S. Han *et al.*, "Graphene mode-lockers for fiber lasers functioned with evanescent field interaction," Appl. Phys. Lett., **96,** 051122 (2010).

[4.26] A. Martinez, K. Fuse, and S. Yamashita, "Mechanical exfoliation of graphene for the passive mode-locking of fiber lasers," Appl. Phys. Lett., **99,** 121107

(2011).

[4.27] J. L. Xu, X. L. Li, Y. Z. Wu *et al.*, "Graphene saturable absorber mirror for ultra-fast-pulse solid-state laser," Opt. Lett., **36,** 1948-1950 (2011).

[4.28] H. Kim, J. Cho, S. Y. Jang *et al.*, "Deformation-immunized optical deposition of graphene for ultrafast pulsed lasers," Appl. Phys. Lett., **98,** 021104 (2011).

[4.29] F. Bonaccorso, Z. Sun, T. Hasan *et al.*, "Graphene photonics and optoelectronics," Nature Photon., **4,** 611-622 (2010).

[4.30] E. Hendry, P. J. Hale, J. Moger *et al.*, "Coherent nonlinear optical response of graphene," Phys. Rev. Lett., **105,** 097401 (2010).

[4.31] E. G. Mishchenko, "Dynamic conductivity in graphene beyond linear response," Phys. Rev. Lett., **103,** 246802 (2009).

[4.32] F. T. Vasko, "Saturation of interband absorption in graphene," Phys. Rev. B, **82,** 245422 (2010).

[4.33] Z. Zhang, and P. L. Voss, "Full-band quantum-dynamical theory of saturation and four-wave mixing in graphene," Opt. Lett., **36,** 4569-4571 (2011).

[4.34] M. S.A, "Theory of the nonlinear optical frequency mixing effect in graphene," Physica E, DOI: 10.1016/j.physe.2010.10.014.

[4.35] R. L. Sutherland, D. G. Mclean, S. Kirkpatrick, "Handbook of nonlinear optics," Marcel Dekker: New York (2003).

[4.36] M. Currie, J. D. Caldwell, F. J. Bezares *et al.*, "Quantifying pulsed laser induced damage to graphene," Appl. Phys. Lett., **99,** 211909 (2011).

[4.37] H. Yang, X. Feng, Q. Wang *et al.*, "Giant two-photon absorption in bilayer

graphene," Nano Lett., **11,** 2622-2627 (2011).

[4.38] R. Edziah, E. Lalanne, V. Torres *et al.*, "Z-scan measurements using ultrashort high-repetition-rate lasers: how to recognize the parasitic effects of nonlinear behavior of fused-silica damage sites," J. Opt. Soc. Am. B, **28,** 1385-1390 (2011).

[4.39] B. J. Schultz, C. J. Patridge, V. Lee *et al.*, "Imaging local electronic corrugations and doped regions in graphene," Nature Commun., **2,** 372 (2011).

[4.40] J. S. Lauret, C. Voisin, G. Cassabois *et al.*, "Ultrafast carrier dynamics in single-wall carbon nanotubes," Phys. Rev. Lett., **90,** 057404 (2003).

[4.41] H. I. Elim, W. Ji, G. H. Ma *et al.*, "Ultrafast absorptive and refractive nonlinearities in multiwalled carbon nanotube films," Appl. Phys. Lett., **85,** 1799-1801 (2004).

[4.42] D. Shimamoto, T. Sakurai, M. Itoh *et al.*, "Nonlinear optical absorption and reflection of single wall carbon nanotube thin films by Z-scan technique," Appl. Phys. Lett., **92,** 081902 (2008).

[4.43] T. Hasan, Z. Sun, F. Wang *et al.*, "Nanotube–polymer composites for ultrafast photonics," Adv. Mater., **21,** 3874-3899 (2009).

[4.44] Z. Q. Luo, S. H. Lim, Y. M. You *et al.*, "Effect of ion bombardment on the synthesis of vertically aligned single-walled carbon nanotubes by plasma-enhanced chemical vapor deposition," Nanotechnology, **19,** 255607(2008).

Chapter 5

Two-photon absorption in bilayer graphene

5.1 Introduction

Graphene exhibits unique one-photon absorption (1PA) features, which have attracted a great deal of research interest [5.1-5.3] and discussed in the previous chapter. Recently, two-photon absorption (2PA) in graphene and graphite has also received attention [5.4-5.5]. Quantum interference between 1PA and 2PA has been demonstrated [5.4] to provide a solution to the coherent control and noncontact generation of ballistic photocurrent in multilayer graphene, which have applications in quantum technology. Furthermore, 2PA in graphene is one of the fundamental yet relevant processes if graphene is considered as a material candidate for next-generation photonic and optoelectronic devices. Despite such potentials and importance, up to date, there is no report on the characteristics and magnitudes of 2PA in graphene. Here, we present our experimental observation of frequency-degenerate 2PA in graphene and comparison with a 2PA theory. Our findings show that 2PA is significantly different and greater in Bernal-stacked (or AB-stacked) bilayer graphene than in monolayer graphene. Such significant difference provides a practically efficient and explicit way of indentifying the stacking orders of bilayer graphene.

This chapter is organized in the following way. Section 5.2 presents our experimental observation of 2PA in graphene. Section 5.3 details a quantum perturbation theory for 2PA in graphene. The comparison between the experiment and

theory and discussion are given in Section 5.4, followed by a conclusion in Section 5.5.

5.2 Experimental evidence of two-photon absorption (2PA) in graphene

In order to study the 2PA of graphene, we carried out optical experiments on high-quality monolayer and bilayer epitaxial graphene as their band structure and 1PA have been well-investigated and well-documented [5.1-5.3, 5.6-5.16]. The characterization of the monolayer and bilayer epitaxial graphene samples used in this chapter has been introduced in detail in Chapter 2.

The nonlinear light absorption of the above samples was detected by using both transient absorption (or frequency-degenerate, time-resolved pump-probe) measurement and Z-scan technique [5.17] at 780 nm at room temperature. The laser pulses (780 nm, 400 fs, 1 kHz) were produced by a mode-locked Ti:Sapphire laser (Quantronix, IMRA), which seeded a Ti:Sapphire regenerative amplifier. In the transient absorption measurement, see the set-up in Figure 5.1 (a), the pump and probe pulses were orthogonally polarized with the incident angle between them was less than three degrees. The energy ratio of the probe to pump pulse was less than 5%. The set-up was calibrated by using a wide-gap semiconductor CdS as a standard sample, as shown in Figure 5.2 (a). The measured signals are fit with a two-exponential-component decay, the fast lifetime accounts for the laser pulse duration and the slow lifetime indicates the carrier recombination time (~1 ps for the

bilayer graphene sample, for example). The transient absorption measurements were also conducted at various maximum excitation intensities, as shown in Figure 5.2 and Figure 5.3. From these data, we plot the transient absorption signal at zero delay as a function of the maximum excitation intensity, as displayed in Figure 5.4.

The transient absorption signals of graphene in our measurements are compared with the reports from other groups, as shown in Table 5.1. There are two main time scales in the relaxation process of photo-excited carriers in graphene. Immediately after the electrons are excited to the conduction band, carrier-carrier and carrier-optical phonon will domination the initial thermalization and a quasi-equilibrium will be established. The time scale of this process is around 10-100 fs [5.18, 5.23]. Subsequently, electron-phonon scattering and interband recombination will dominant the slower relaxation process, which is in the time scale of few picoseconds. In our measurements, the ultrafast τ_1 is not resolvable with the pulse duration used in the experiment (~400 fs). The slower relaxation process is measured to be around 1 ps, which is consistent with results from other groups [5.18, 5.21]. The carrier dynamics of CVD graphene is relatively faster as reported [5.22]. The reason could be that the photo-excited carriers in CVD graphene are strongly localized due to the lower electric conductivity [5.27]. The accumulation of the high density of hot carriers enhances carrier-carrier and carrier-phonon scattering and accelerates the relaxation process [5.29]. Besides, the photo-excited carrier dynamics could also be affected by the substrate, which could be an energy exchange interface [5.22, 5.24, 5.26].

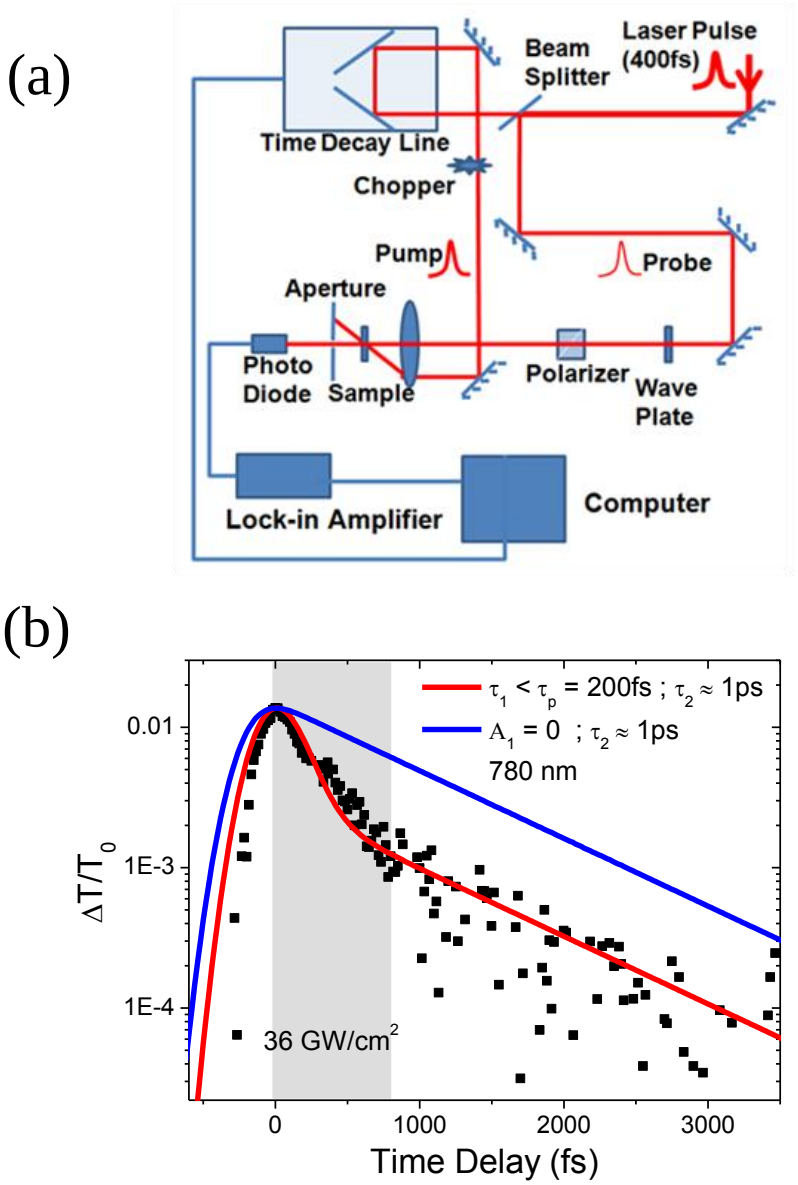

Figure 5.1. (a) Schematic set-up for transient absorption measurement on the bilayer graphene. (b) Experimental data (black) and theoretical fits with $\int_0^\infty (A_1 e^{-\tau/\tau_1} + A_2 e^{-\tau/\tau_2}) e^{-(t-\tau-t_0)^2/\tau_p^2} d\tau$, where A_1, A_2 and t_0 are constants, and $\tau_p \approx 200$ fs (HWe-1M for pulse duration). The red curve is the bi-exponential fit with $A_1 \neq 0$, while the blue curve is the mono-exponential fit with $A_1 = 0$.

Table 5.1. Comparison of transient absorption signals.

Sample	**Pump condition**	**Probe condition**	**Time scale**		**References**
			τ_1	τ_2	
Epitaxial 6,12,37 layers	780 nm, 85 fs, 81 MHz	degenerate	70-120 fs	0.4-1.7 ps	[5.18]
CVD 8 layers	350 nm, 65 fs, 1 kHz	380-670 nm	50-70 fs	0.1-0.2 ps	[5.20]
Epitaxial 2 layers	390 nm, 200 fs, 89 MHz	780 nm	N.A.	1.1-1.3 ps	[5.21]
CVD 1-4, 10 layers	350 nm, 65 fs, 1 KHz	550-676 nm	60 ±20 fs	0.15-0.2 ps	[5.22]
Exfoliated graphene	828 nm, 7 fs,71 MHz	828 nm	50 fs	0.3 ps	[5.23]
Exfoliated graphene	830 nm, 180 fs	1100-1400 nm, 240 fs	N.A.	3.35-3.6 ps	[5.24]
Epitaxial graphene 15-20 layers (Temperature 10-300 K)	800 nm, 100 fs, 250 kHz	1600-2600 nm	N.A.	1-10 ps	[5.25]
CVD graphene few layer	350 nm (120 fs), 680 nm (90 fs), 1kHz	400-650 nm	50 fs	0.09-0.22 ps	[5.26]
Epitaxial graphene 1,2 layers	780 nm, 400 fs, 1kHz	degenerate	N.A.	1 ps	Current study

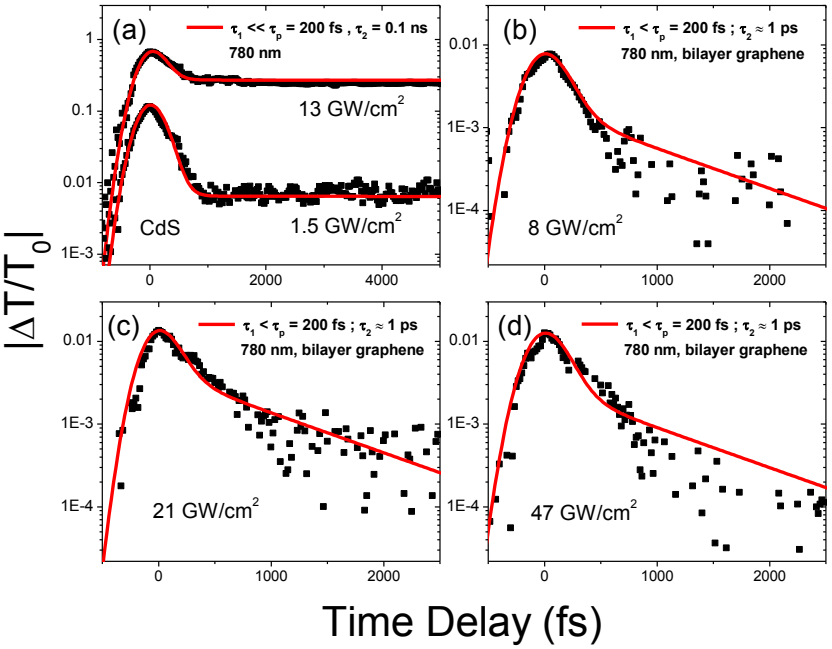

Figure 5.2. Transient absorption signals at 780 nm for a standard sample (CdS) and the bilayer graphene on the C-face of SiC. The black squares are the experimental data and the red curves are the theoretical fits with the bi-exponential decay modeling.

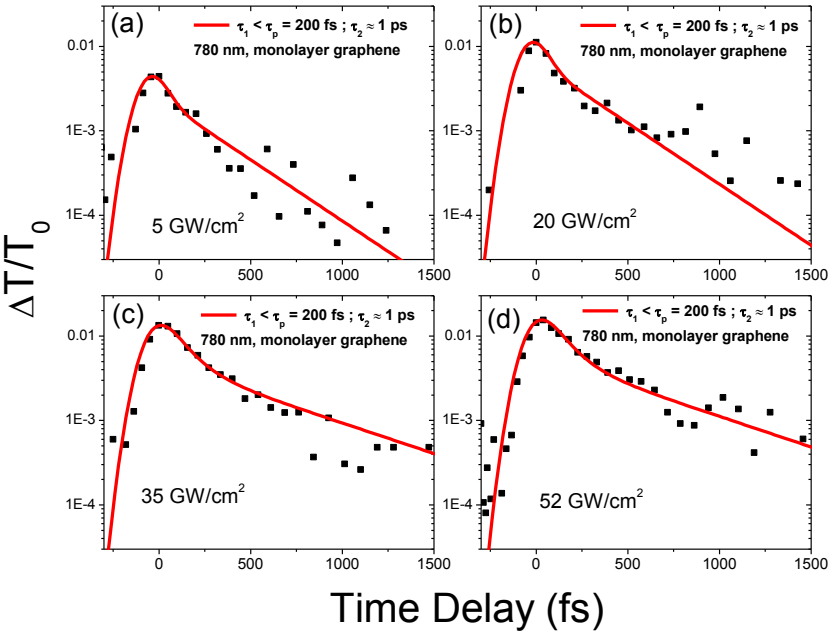

Figure 5.3. Transient absorption signals at 780 nm for the monolayer graphene on the C-face of SiC. The black squares are the experimental data and the red curves are the theoretical fits with the bi-exponential decay modeling.

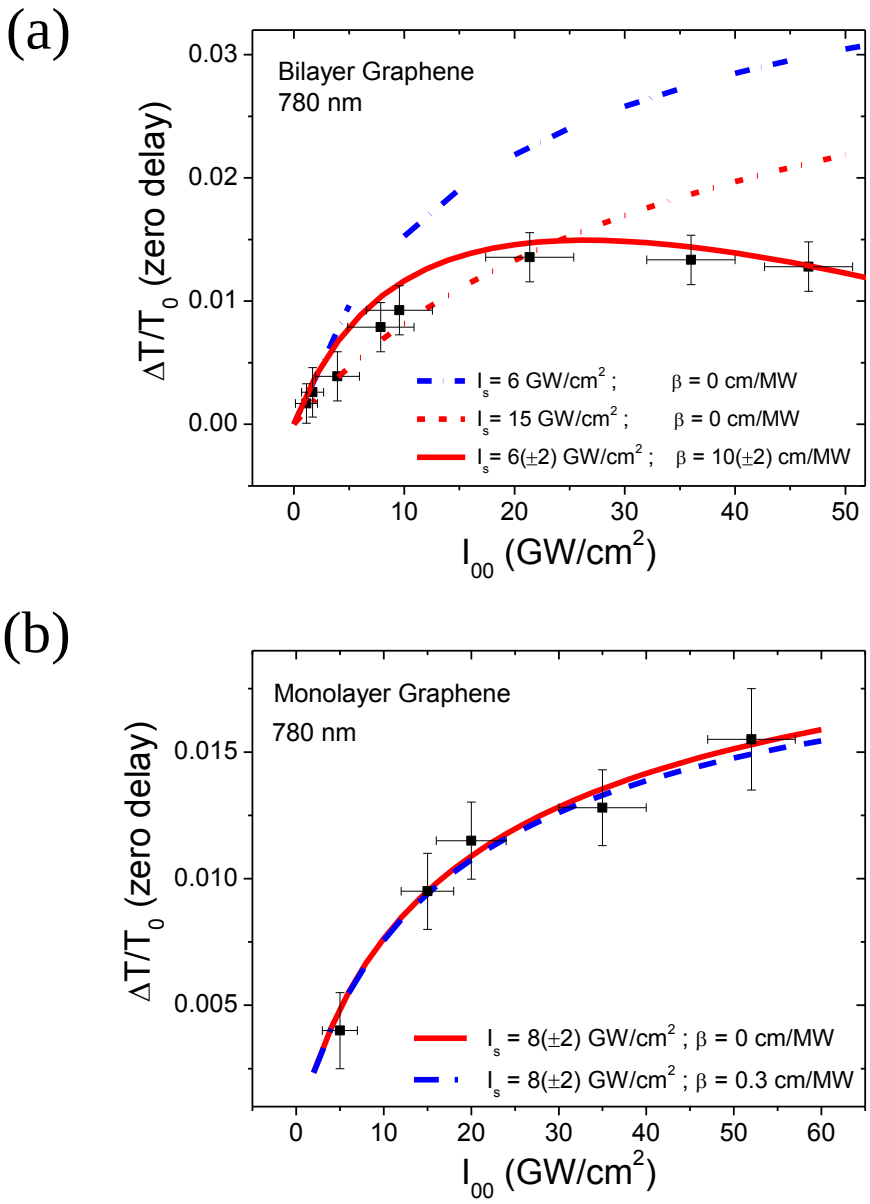

Figure 5.4. Experimental data (black squares) and theoretical fits (curves) for transient absorption at zero delay on (a) bilayer and (b) monolayer graphene at 780 nm. The error bars are calculated from 5 series of repeated measurements at each intensity, taking into account of estimated error (~5%) in the measurement of laser pulse energy. The details of the theoretical fits are described in the text.

In the Z-scans, the laser pulses were focused with the minimum beam waist of 25±2 μm. The Z-scan set-up was calibrated by using another standard sample, ZnSe. As displayed in Figure 5.5 (a), the transmitted laser pulse energies were monitored by

moving the sample along the propagation direction (or z-axis) of the laser pulses. Additional Z-scans at 1100 nm were measured with an optical parametric amplifier (Coherent TOPAZ) pumped by another regenerative amplifier (Coherent Legend, 780 nm, 100 fs, 1 kHz). For all the Z-scans reported here, the maximum on-axis irradiance (I_{00}) of the laser pulses was 150 GW/cm^2 or lower at the focus. No laser-induced damage was observed at 150 GW/cm^2 or less. As the sample was scanned and the incident laser pulse energies were kept at a constant level, the sample experienced different laser irradiances at different *z*-positions, giving rise to a different transmission if the sample absorbed light nonlinearly, see examples in Figures 5.5 (b)&(c). The measured nonlinear transmittance (Z-scan or $\Delta T/T_0$ at zero delay) was analyzed by using the nonlinear propagation equation, $dI/dz = -[\alpha_0/(1+I/I_s)+\beta I]I$, which was solved numerically and then integrated over space and time to obtain the transmitted laser pulse energy, as introduced in Chapter 3. In the numerical simulation for the best fit, the α_0 parameter used matches to the theoretical 1PA coefficient [5.10-5.13].

(a)

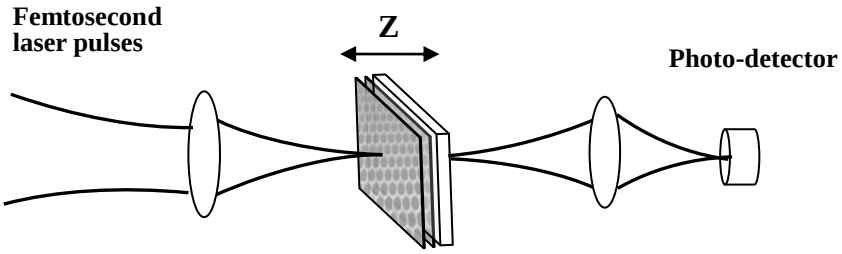
Femtosecond
laser pulses
Z
Photo-detector

(b)

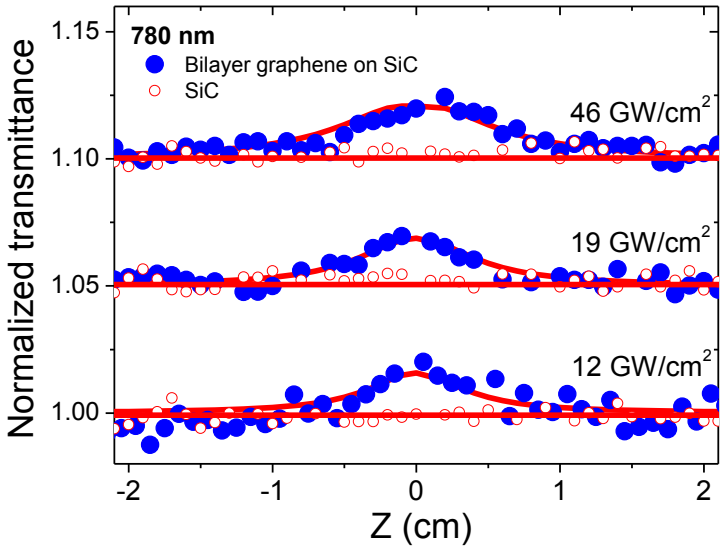
780 nm
Bilayer graphene on SiC
SiC
46 GW/cm2
19 GW/cm2
12 GW/cm2
Normalized transmittance
1.15
1.10
1.05
1.00
-2
-1
0
1
2
Z (cm)

(c)

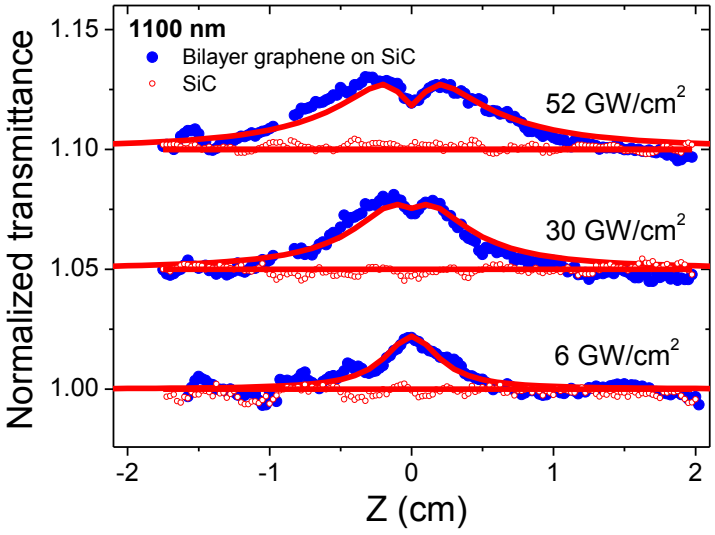
1100 nm
Bilayer graphene on SiC
SiC
52 GW/cm2
30 GW/cm2
6 GW/cm2
Normalized transmittance
1.15
1.10
1.05
1.00
-2
-1
0
1
2
Z (cm)

Figure 5.5. Schematic set-up and Z-scans on the bilayer graphene on the substrate (blue symbols) and the substrate alone (red symbols) at 780 nm and 1100 nm. The upper Z-scans are vertically shifted for clear presentation. The on-axis maximum power density at focus for each Z-scan is shown for each Z-scan. The theoretical fits (red solid line) to the Z-scan data are calculated from the nonlinear propagation equation, $dI/dz = -[\alpha_0/(1+I/I_s)+\beta I]I$, where α_0 is the linear absorption coefficient, I_s is the saturation intensity, and β is the 2PA coefficient. More details on modeling can be found in the text.

Both transient nonlinear transmission measurements in Figure 5.1 and Z-scans in Figure 5.5 indicate that their signals are dominated by saturable absorption due to Pauli blocking resulting from 1PA, in agreement with previous reports [5.18-5.26, 5.28, 5.29]. At relatively lower excitation (I_{00} < 10 GW/cm^2), the 2PA is too small to outperform the saturation of 1PA. However, the 2PA manifests itself at higher excitation in bilayer graphene, see the bending of $\Delta T/T_0$ (zero delay) in Figure 5.1 (c) and the dip on the Z-scan (z = 0) in Figure 5.5 (c). It should be pointed out that in the pump-probe experiment, the minimum beam waist of the pump pulses was adjusted to ~50 μm, in order to ensure the total overlapping between the pump and probe pulses. As such, the maximum excitation level (or I_{00}) was reduced to ~50 GW/cm^2. Though the excitation level could be up to 150 GW/cm^2 in the Z-scans, our analysis is limited to the range from a few to 70 GW/cm^2, avoiding other high-order nonlinear mechanisms (such as three-photon absorption). Even within this limited range of excitation, it is found that the data cannot be fit with a saturation model alone, as discussed in the following.

The 2PA contribution to the overall nonlinear signal can be uncovered by analyzing the data with the total absorption coefficient, $\alpha_0/(1+I/I_s)+\beta I$, where the first

term is a phenomenological expression for absorption saturation (with α_0 being the small-signal 1PA coefficient and I_s being the saturation irradiance); and the second term quantifies 2PA. The best fits to all the measurements, obtained at two different light wavelengths, various excitation irradiance (I_{00} = a few to 70 GW/cm^2) and different positions on the sample, lead to that I_s = 6±2, 1.5±0.5 GW/cm^2; and β = 10±2, 20±4 cm/MW at wavelengths of 780 and 1100 nm, respectively. If β = 0 cm/MW, the above simulation becomes a simple saturation modeling. The dashed curves in Figure 5.4 (a) show the failure of the saturation model [$\alpha = \alpha_0/(1+I/I_s)$]. The transient absorption signals for a standard sample (CdS) and the bilayer graphene sample at 780 nm are shown in Figure 5.2. The slow process in the transient absorption signal for CdS is due to the free carrier absorption. We have also conducted similar experiments on a monolayer graphene sample. The transient absorption signals for the monolayer graphene at 780 nm are shown in Figure 5.3. As shown in Figure 5.2 and 5.3, the time scale τ_2 in monolayer and bilayer graphene are measured to be around 1 ps. The scattering between sub-bands in bilayer graphene is mixed with the scattering between conduction and valence bands, and is timely unresolved with the pump condition. The measurement of $\Delta T/T_0$ at zero delay for monolayer graphene at 780 nm is shown in Figure 5.4 (b). It is found that its 2PA is too insignificant to be detected in monolayer graphene, consistent with Equation (5.4), as discussed in the next section. Our femtosecond time-solved transient absorption measurements show that the carbon-rich layer made no contribution to the measured overall nonlinear absorption.

The Z-scans on the monolayer graphene sample at 780 nm and 1100 nm are shown in Figure 5.6. It is found that all the Z-scans can be fitted with $dI/dz = -[\alpha_0/(1+I/I_s)]I$ without the 2PA term even the excitation intensity is up to 150 GW/cm^2. It indicates that 2PA is too small to be detected, which is consistent with our theoretical results, as given in Section 5.3.

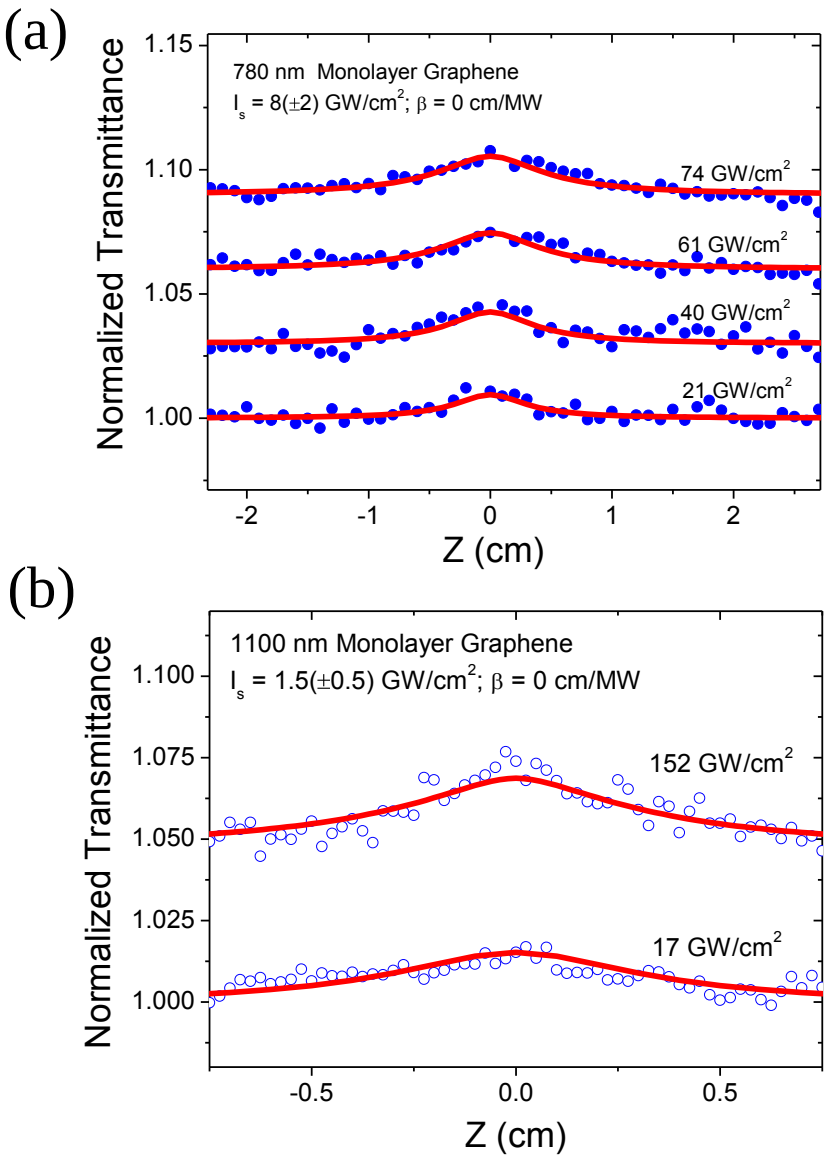

Figure 5.6. Z-scans on the monolayer graphene sample at 780 nm and 1100 nm. The circles are the experimental data and the curves are the theoretical fits. The upper Z-scans are vertically shifted for clear presentation.

For clear comparison, we convert the Z-scan data with $I_0 = I_{00} / (1 + z^2/z_0^2)$, I_{00} is on-axis maximum power density at the focus, z is the position of the sample from the focal plane, z_0 is equal to $\pi w_0^2/\lambda$ and w_0 is the minimum beam waist at focus. Then, we plot the normalized transmittance versus I_0 for the mono- and bi-layer graphene samples at 780 nm and 1100 nm, as shown in Figure 5.7. It is clear to see that the 2PA contribution to the overall nonlinear signal is significant in the bilayer graphene.

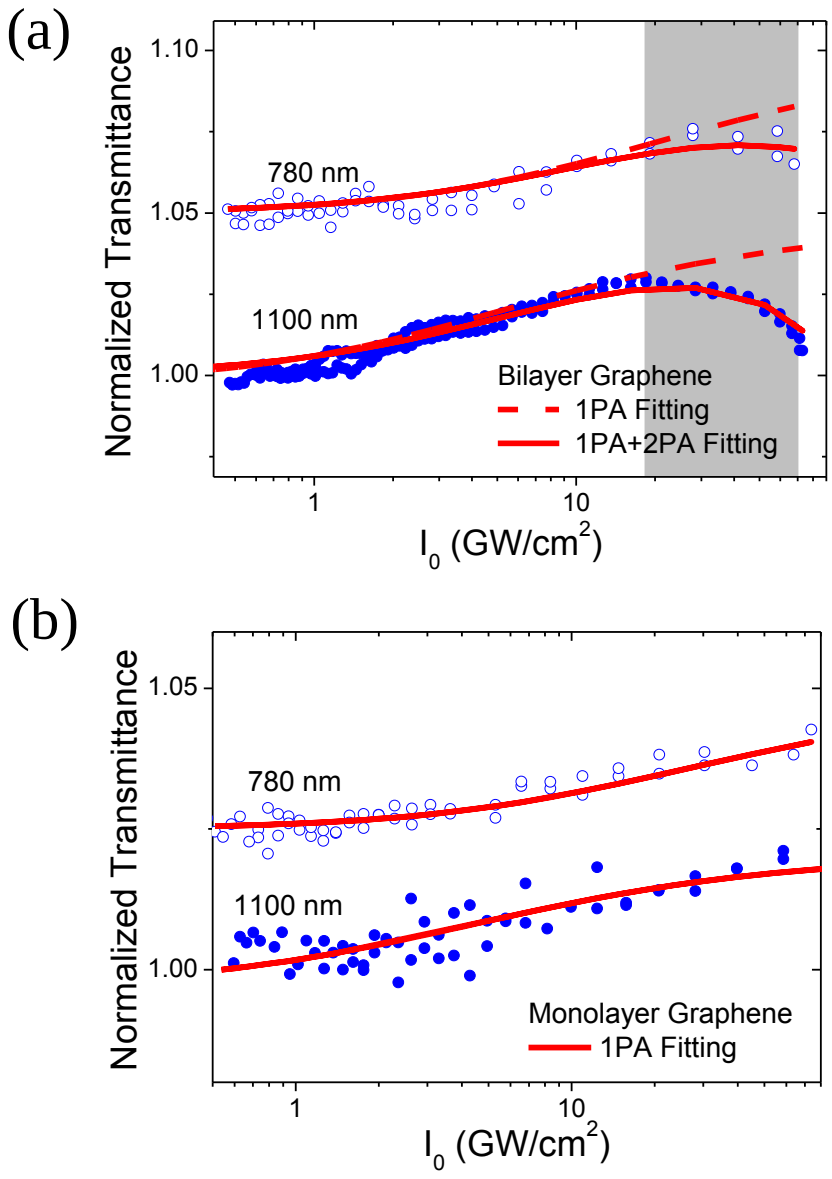

Figure 5.7. The normalized transmittance versus the irradiance for (a) bilayer and (b) monolayer graphene sample at 780 nm and 1100 nm. The circles are the experimental data and the curves are the theoretical fits. The upper curves are vertically shifted for clear presentation.

5.3 Quantum perturbation theory

To gain a full understanding of the observed 2PA coefficient of bilayer graphene and to explain why there is the absence of 2PA in monolayer graphene, a 2PA theory was developed from quantum mechanics by my collaborator, Dr. Xiaobo Feng; and is presented as follows.

The quantum perturbation theory here is limited to both un-doped monolayer and bilayer graphene since their band structures and 1PA have been well-understood [5.1-5.3, 5.6-5.16]. As illustrated in Figure 5.8, 2PA is an interband transition wherein two photons, each of energy $\hbar\omega$, are absorbed simultaneously, thereby creating an electron in the conduction band and a hole in the valence band. In monolayer graphene, the electronic dispersion of the conduction (π^*) or valence (π) band can be written as $E^{+}(k) = \pm\hbar\upsilon_F|k|$, due to the Fermi-Dirac-like nature of the two-dimensional atomic layer [5.30-5.31]. The electron wave function $\psi(r)$ close to the K point, obeys the two-dimensional Dirac equation as follows [5.30],

$$-i\upsilon_F\boldsymbol{\sigma}\cdot\nabla\psi(\mathbf{r}) = E\psi(\mathbf{r}) \tag{5.1}$$

In the momentum space, for momentum around the K point, the wave function has the form of [5.30]

$$\psi_{\pm}(\mathbf{k}) = \frac{1}{\sqrt{2}} \begin{pmatrix} e^{-i\theta_{\mathbf{k}}/2} \\ \pm e^{i\theta_{\mathbf{k}}/2} \end{pmatrix} \tag{5.2}$$

where the $\pm$ signs correspond to the eigenenergies for the π^* and π band, respectively, and θ_k is given by $\theta_k = \arg(k_x + ik_y)$. By using the second-order perturbation theory of quantum mechanics, the second-order interband transition probability rate per unit area (W_2) can be written as [5.32]:

$$W_2 = \frac{2\pi}{\hbar} \int \left| \sum_i \frac{\langle \psi_+(\mathbf{k}) | H | \psi_i(\mathbf{k}') \rangle \langle \psi_i(\mathbf{k}') | H | \psi_-(\mathbf{k}) \rangle}{E_i(\mathbf{k}') - E_-(\mathbf{k}) - \hbar\omega} \right|^2 \delta[E_+(\mathbf{k}) - E_-(\mathbf{k}) - 2\hbar\omega] \frac{d^2\mathbf{k}}{(2\pi)^2} \tag{5.3}$$

where ψ_- and ψ_+ are the electronic wave function for the initial and final state of the transition, respectively; ψ_i is the all-possible intermediate state; and H is the interaction Hamiltonian: $H = (e/c)\mathbf{A} \cdot \upsilon_F \boldsymbol{\sigma}$, where $\mathbf{A} = A\mathbf{e}$ is the vector potential of the light wave with the amplitude A and the polarization vector e. The amplitude A is related to the light irradiance by $I = \varepsilon_\omega^{1/2} \omega^2 A^2 (2\pi c)^{-1}$. The density-of-state argument is implicitly included in the integration of k in Equation (5.3) [5.33]. By including all possible intermediate states in the two bands, we find an analytical expression for the 2PA coefficient ($\beta = 4W_2\hbar\omega / I^2$) as follows:

$$\beta^{monolayer} = \frac{4\pi^2}{\varepsilon_\omega \omega^4 \hbar^3} \left(\frac{\upsilon_F e^2}{c} \right)^2 \tag{5.4}$$

As for AB-stacked bilayer graphene, it is differentiated from monolayer graphene because bilayer possesses two more bands. In the continuum limit, by expanding

momentum close to the K point in the Brillouin Zone (BZ), the Hamiltonian in the momentum space can be written as a matrix as follows [5.30]:

$$\mathrm{H}_K = \begin{pmatrix} -V & \upsilon_F k\hbar & 0 & 3\gamma_3 a k^* \\ \upsilon_F k^*\hbar & -V & \gamma_1 & 0 \\ 0 & \gamma_1 & V & \upsilon_F k\hbar \\ 3\gamma_3 a k & 0 & \upsilon_F k^*\hbar & V \end{pmatrix} \tag{5.5}$$

where γ_1 is the hopping energy between atom A_1 and atom A_2, as shown in Figure 2.2, γ_3 is the hopping energy between atom B_1 and atom B_2 in the graphite nomenclature; and V is half the shift in electrochemical potential between the two layers. If $V = 0$, $\gamma_3 = 0$, and $\upsilon_F k\hbar << \gamma_1$ (= 0.4 eV), Equation (5.5) gives rise to four parabolic bands, as shown in the inset of Figure 5.1. Two bands ($E_1 \approx \pm\hbar^2\upsilon_F^2 k^2 / \gamma_1$) touch each other at k = 0, while other two bands ($E_2 \approx \pm\gamma_1 \pm \hbar^2\upsilon_F^2 k^2 / \gamma_1$) have a minimum energy of $\pm\gamma_1$ (or a band gap energy of $2\gamma_1$) at $k = 0$. The electron effective mass can be derived as $m = \gamma_1 / (2\upsilon_F^2)$. There are four possible transitions, as shown in Figure 5.8 (a). All the four transitions are included in the calculation of 2PA coefficient if $\hbar\omega > \gamma_1$, which leads to an analytical expression as follows:

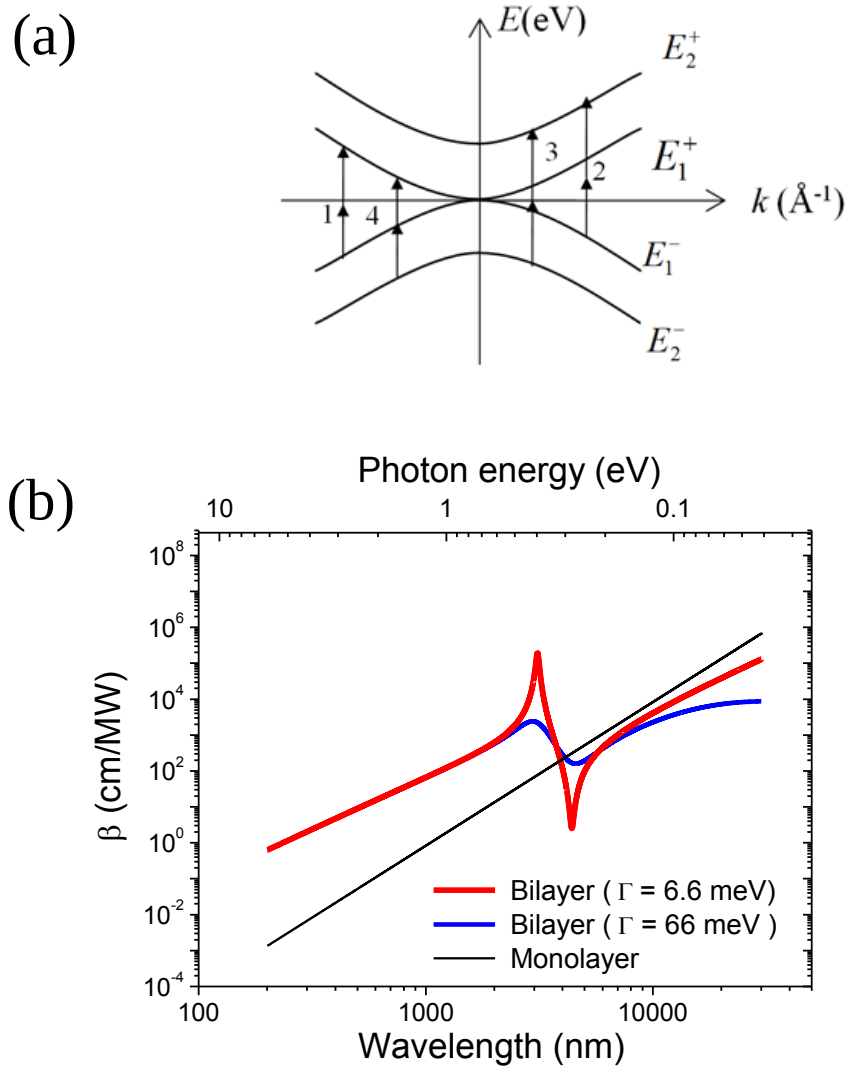

Figure 5.8. (a) Four possible transitions in bilayer graphene. (b) 2PA spectra of monolayer and bilayer graphene.

$$\begin{aligned}\beta^{bilayer} = 8\beta^{monolayer}\frac{\hbar\omega}{\gamma_1}[&16\hbar^2\omega^2\left(\frac{1}{\hbar\omega}+\frac{1}{\gamma_1+\hbar\omega}\right)^2 \\ &+(2\hbar\omega-\gamma_1)^2\left(\frac{2}{\hbar\omega}+\frac{1}{\hbar\omega+\gamma_1}+\frac{1}{\hbar\omega-\gamma_1}\right)^2 \\ &+16(\hbar\omega-\gamma_1)^2\left(\frac{1}{\hbar\omega}+\frac{1}{\hbar\omega-\gamma_1}\right)^2 \\ &+(2\hbar\omega-\gamma_1)^2\left(\frac{2}{\hbar\omega}+\frac{1}{\hbar\omega+\gamma_1}+\frac{1}{\hbar\omega-\gamma_1}\right)^2]\end{aligned} \tag{5.6}$$

where the four terms in the square bracket correspond to Transitions 1-4, respectively, in Figure 5.8 (a). There are four possibilities of interband transitions for incident photon energy $\hbar\omega > \gamma_1$: from the lower valence band (E_2^-) to the conduction band (E_1^+ or E_2^+), and from the upper valance band (E_1^-) to the conduction band (E_1^+ or E_2^+). As they all satisfy the law of energy conservation, they all contribute to the 2PA coefficient. If $\hbar\omega < \gamma_1/2$, only Transition 1 is possible because three other transitions do not satisfy the law of energy conservation. As such, the first term in Equation (5.6) remains and the other terms disappear. If $\gamma_1/2 < \hbar\omega < \gamma_1$, Transitions 1, 2 and 4 meet the law of energy conservation but Transition 3 does not. In this case, Equation (5.6) includes the three terms and the third term is omitted.

Owing to two more bands originated from the inter-layer interaction in bilayer, which considerably enhances two-photon transition probability, Equation (5.6) shows that 2PA in bilayer is significantly different from monolayer with the following characteristics: (i) there is a resonant feature (or singularity) centered at $\hbar\omega = \gamma_1$; (ii) 2PA in monolayer has a ω^{-4} dependence for all photon frequencies, while 2PA in bilayer becomes proportional to ω^{-3} in the off-resonant regions of $\hbar\omega >> \gamma_1$ or $\hbar\omega << \gamma_1/2$; and (iii) in the computation of Equation (5.6), there is a difficulty at $\hbar\omega = \gamma_1$ as it is a singularity. To avoid this problem, a common approach is to introduce a phenomenological term called the line broaden factor, Γ, which is inversely proportional to the dephasing time. As such, the denominator in Equation (5.3) becomes $E_i(\mathbf{k}) - E_1^+(\mathbf{k}) - \hbar\omega - i\Gamma$, and the 2PA coefficient is given by

$$\beta^{bilayer} = 8\beta^{monolayer}\frac{\hbar\omega}{\gamma_1}[4\hbar^2\omega^2\left|\frac{1}{\hbar\omega - i\Gamma}+\frac{1}{\hbar\omega + i\Gamma}+\frac{1}{\gamma_1+\hbar\omega - i\Gamma}+\frac{1}{\gamma_1+\hbar\omega + i\Gamma}\right|^2$$
$$+(2\hbar\omega-\gamma_1)^2\left|\frac{1}{\hbar\omega - i\Gamma}+\frac{1}{\hbar\omega - i\Gamma}+\frac{1}{\hbar\omega+\gamma_1 + i\Gamma}+\frac{1}{\hbar\omega-\gamma_1 - i\Gamma}\right|^2$$
$$+4(\hbar\omega-\gamma_1)^2\left|\frac{1}{\hbar\omega - i\Gamma}+\frac{1}{\hbar\omega + i\Gamma}+\frac{1}{\hbar\omega-\gamma_1 - i\Gamma}+\frac{1}{\hbar\omega-\gamma_1 + i\Gamma}\right|^2$$
$$+(2\hbar\omega-\gamma_1)^2\left|\frac{1}{\hbar\omega - i\Gamma}+\frac{1}{\hbar\omega - i\Gamma}+\frac{1}{\hbar\omega+\gamma_1 + i\Gamma}+\frac{1}{\hbar\omega-\gamma_1 - i\Gamma}\right|^2].$$

(5.7)

By using the dielectric constant ε_ω = 9 (see Ref. 5.34) and Γ = 66 meV or 6.6 meV, Equation (5.4) and Equation (5.7) plotted in Figure 5.8 (b) demonstrate that the 2PA is two orders of magnitude greater in bilayer than in monolayer in the near infrared region (800~1100 nm). It also shows that 2PA is nearly independent of Γ in this spectral region if the values of Γ are between 6 and 66 meV, which correspond to dephasing times between 50 fs and 5 fs, respectively.

5.4 Comparison and discussion

In the experiment, the two-photon absorption is measured in bilayer graphene. As shown in Figure 5.4 (a) and 5.7 (a). Especially, at high intensities (shade area in Figure 5.7 (a)), the two-photon absorption manifests itself as the transmittance decreases. In the measurement, the two-photon absorption coefficient of bilayer graphene increases as the excitation extends to longer wavelength. The two-photon absorption is not detectable in monolayer graphene as shown in Figure 5.4 (b) and 5.7(b), which is consistent with the theoretical prediction that the two-photon absorption coefficient of monolayer graphene is nearly two orders smaller than

bilayer graphene at the wavelengths in the experiment. The measured 2PA coefficients of the bilayer sample are 10 and 20 cm/MW, at 780 and 1100 nm, respectively. They are less than the theoretical predictions (32 cm/MW at 780 nm and 88 cm/MW at 1100 nm, but are within the same order of magnitude. The discrepancy is expected due to the following two reasons. First, our theory considers the γ_1-terms in Equation (5.5) only and ignores other complexities by letting $V = 0$, $\gamma_3 = 0$, which account for band perturbations arising from trigonal warping and electro-hole asymmetry in "skew" interlayer coupling [5.13, 5.14, 5.30]. Second, recent experimental evidence [5.35, 5.36] indicates the co-existence of both AB stacking and decoupled layers by azimuthal rotation in bilayer graphene on the C-face of SiC substrate, consistent with our STM studies, as shown in Figure 2.5(b). This is also attributed to our observation of smaller 2PA coefficients.

The measured 2PA coefficient of bilayer graphene is also compared with other narrow-gap semiconductors. As shown in Table 5.2, the magnitude of 2PA coefficient of bilayer graphene is at least five orders of magnitude greater than that for many narrow-gap semiconductors (such as InSb, InGaAs, etc.) in the infrared region. This implies that bilayer graphene has greater potential in 2PA-based infrared technology.

Table 5.2. Comparison of two-photon absorption coefficient (β).

Material	λ (nm)	β (10^{-9} cm/W)	Method	Reference
Cadmium selenide (CdSe)	1064	30	Nonlinear Transmittance	[5.37]
Gallium arsenide (111) (GaAs)	1064	25	Z-scan	[5.38]
Indium phosphide (bulk InP)	1064	90	Z-scan	[5.39]
SWNTs	780	1,400	Z-scan	[5.40]
Bilayer Graphene	780	10,000	Z-scan	Present study
	1100	20,000		

Within the same order of magnitude, the measured β values are in agreement with 32 and 88 cm/MW predicted by Equation (5.7) for the two wavelengths, respectively. The agreement on the order of magnitude implies that the four parabolic bands should play an essential role in the 2PA process. Interestingly, the 2PA of bilayer graphene reaches a maximum (~0.2 cm/W if Γ = 6.6 meV) at $\hbar\omega = \gamma_1$ (= 0.4 eV, or 3.1 μm), resulting from resonance with half of the bandgap between the E_2 bands. This β value is at least five orders of magnitude greater than that for many narrow-gap semiconductors (such as InSb, InGaAs, etc.) in the infrared region as shown by Table 5.1. It is important to note that unlike 2PA coefficients in the non-resonant region (λ < 2000 nm), resonant β-values are sensitive to the broaden factor, Γ. This factor is related to the time for a dephasing process in which coherence in graphene caused by perturbation decays over time. Such de-coherence could be caused by incoherent processes such as carrier-carrier scattering. From Equation (5.7) or Figure 5.8, the

maximum 2PA coefficient should be ~ 0.002 cm/W if Γ = 66 meV, which are still three orders of magnitude larger than the above-said narrow-gap semiconductors.

The quantum perturbation theory on two-photon absorption (2PA) is derived for monolayer and bilayer graphene which is Bernal-Stacked. The theory shows that 2PA is significantly greater in bilayer graphene than monolayer graphene in the visible and infrared spectrum (up to 3 μm) with a resonant 2PA coefficient of up to ~0.2 cm/W located at half of the bandgap energy, γ_1= 0.4 eV. In the visible and THz region, 2PA exhibits a light frequency dependence of ω^{-3} in bilayer graphene, while it is proportional to ω^{-4} for monolayer graphene at all photon energies. Within the same order of magnitude, the 2PA theory is in agreement with our Z-scan measurements on high-quality epitaxial bilayer graphene deposited on SiC substrate at light wavelength of 780 nm and 1100 nm.

The above-discussed giant 2PA should facilitate many quantum technologies, for example, the coherent control of ballistic photocurrent generated by quantum interference between 1PA and 2PA pathway in bilayer graphene. Besides, the generation of ballistic photocurrent by 1.55-μm photons through 1PA and 3.1-μm photons through 2PA is desirable because 1.55-μm wavelength is close to one of the telecom bands. Furthermore, such giant 2PA is predicted and found in Bernal-stacked bilayer graphene. If bilayer graphene is stacked in other ways whereby the interlayer interaction is insignificant, *i.e.* γ_1 = 0, its 2PA value is expected to be as twice as the $\beta^{\text{monolayer}}$ value, which is two orders of magnitude less than the AB-stacked sample. Hence, the difference in 2PA measurements provides a practically efficient and

explicit way of indentifying the stacking orders of bilayer graphene.

5.5 Conclusion

The 2PA in AB-stacked bilayer graphene is observed with femtosecond time-resolved transient absorption measurements and Z-scans in the near infrared spectral region. It is also found that 2PA in monolayer graphene is insignificant at excitation laser intensity of ~100 GW/cm^2 or less. These experimental findings can be explained quantitatively by a 2PA theory derived from quantum perturbation theory, within one order of magnitude. By comparison with many narrow-band-gap semiconductors, the 2PA coefficient of bilayer graphene is at least several orders of magnitude greater, thereby implying that bilayer graphene has tremendous potential in 2PA-based infrared technology.

References

[5.1] K. S. Novoselov, A. K. Geim, S. V. Morozov *et al.*, "Two-dimensional gas of massless Dirac fermions in graphene," Nature, **438,** 197-200 (2005).

[5.2] Y. B. Zhang, Y. W. Tan, H. L. Stormer *et al.*, "Experimental observation of the quantum Hall effect and Berry's phase in graphene," Nature, **438,** 201-204 (2005).

[5.3] C. Berger, Z. M. Song, X. B. Li *et al.*, "Electronic confinement and coherence in patterned epitaxial graphene," Science, **312,** 1191-1196 (2006).

[5.4] D. Sun, C. Divin, J. Rioux *et al.*, "Coherent Control of Ballistic Photocurrents in Multilayer Epitaxial Graphene Using Quantum Interference," Nano Lett., **10,** 1293-1296 (2010).

[5.5] R. W. Newson, J. M. Menard, C. Sames *et al.*, "Coherently controlled ballistic charge currents injected in single-walled carbon nanotubes and graphite," Nano Lett., **8,** 1586-1589 (2008).

[5.6] K. S. Novoselov, A. K. Geim, S. V. Morozov *et al.*, "Electric field effect in atomically thin carbon films," Science, **306,** 666-669 (2004).

[5.7] A. Mattausch, and O. Pankratov, "Ab initio study of graphene on SiC," Phys. Rev. Lett., **99,** 076802 (2007).

[5.8] F. Rana, "Graphene terahertz plasmon oscillators," IEEE T Nanotechnol., **7,** 91-99 (2008).

[5.9] J. M. Dawlaty, S. Shivaraman, J. Strait *et al.*, "Measurement of the optical absorption spectra of epitaxial graphene from terahertz to visible," Appl.

Phys. Lett., **93,** 131905 (2008).

[5.10] E. J. Nicol, and J. P. Carbotte, "Optical conductivity of bilayer graphene with and without an asymmetry gap," Phys. Rev. B, **77,** 155409 (2008).

[5.11] T. Ohta, A. Bostwick, T. Seyller *et al.*, "Controlling the electronic structure of bilayer graphene," Science**, 313**, 951-954 (2006).

[5.12] E. V. Castro, K. S. Novoselov, S. V. Morozov *et al.*, "Biased bilayer graphene: Semiconductor with a gap tunable by the electric field effect," Phys. Rev. Lett., **99,** 216802 (2007).

[5.13] E. McCann, "Asymmetry gap in the electronic band structure of bilayer graphene," Phys. Rev. B, **74,** 161403 (2006).

[5.14] E. McCann, and V. I. Fal'ko, "Landau-level degeneracy and quantum hall effect in a graphite bilayer," Phys. Rev. Lett., **96,** 086805 (2006).

[5.15] J. Nilsson, A. H. C. Neto, F. Guinea *et al.*, "Electronic properties of graphene multilayers," Phys. Rev. Lett., **97,** 266801 (2006).

[5.16] Y. B. Zhang, T. T. Tang, C. Girit *et al.*, "Direct observation of a widely tunable bandgap in bilayer graphene," Nature, **459,** 820-823 (2009).

[5.17] M. Sheikbahae, A. A. Said, T. H. Wei *et al.*, "Sensitive measurement of optical nonlinearities using a single beam," IEEE J. Quantum Electron., **26,** 760-769 (1990).

[5.18] J. M. Dawlaty, S. Shivaraman, M. Chandrashekhar *et al.*, "Measurement of ultrafast carrier dynamics in epitaxial graphene," Appl. Phys. Lett., **92,** 042116 (2008).

[5.19] M. Breusing, C. Ropers, and T. Elsaesser, "Ultrafast carrier dynamics in graphite," Phys. Rev. Lett., **102,** 086809 (2009).

[5.20] J. Z. Shang, Z. Q. Luo, *et al.*, "Femtosecond UV-pump/visible-probe measurements of carrier dynamics in stacked graphene films," Appl. Phys. Lett., **97,** 163103 (2010).

[5.21] L. Huang, G. V. Hartland, *et al.*, "Ultrafast Transient Absorption Microscopy Studies of Carrier Dynamics in Epitaxial Graphene," Nano Lett., **10,** 1308-1313 (2010).

[5.22] J. Shang, T. Yu, *et al.*, "Ultrafast Electron−Optical Phonon Scattering and Quasiparticle Lifetime in CVD-Grown Graphene," ACS Nano, **5,** 3278-3283 (2011).

[5.23] M. Breusing, S. Kuehn, *et al.*, "Ultrafast nonequilibrium carrier dynamics in a single graphene layer," Phys. Rev. B, **83,** 153410 (2011).

[5.24] P. J. Hale, S. M. Hornett, *et al.*, "Hot phonon decay in supported and suspended exfoliated graphene," Phys. Rev. B, **83,** 121404 (2011).

[5.25] D. Sun, Z. K. Wu, C. Divin *et al.*, "Ultrafast relaxation of excited dirac fermions in epitaxial graphene using optical differential transmission spectroscopy," Phys. Rev. Lett., **101,** 157402 (2008).

[5.26] J. Shang, T. Yu, *et al.*, "Femtosecond energy relaxation in suspended graphene: phonon-assisted spreading of quasiparticle distribution," Appl. Phys. B: Lasers and Optics, 107, 131-136 (2012).

[5.27] B. J. Schultz, C. J. Patridge, *et al.*, "Imaging local electronic corrugations and

doped regions in graphene," Nature Commun. **2,** 372 (2011).

[5.28] R. W. Newson, J. Dean, B. Schmidt *et al.*, "Ultrafast carrier kinetics in exfoliated graphene and thin graphite films," Opt. Express, **17,** 2326-2333 (2009).

[5.29] P. A. George, J. Strait, J. Dawlaty *et al.*, "Ultrafast optical-pump Terahertz-probe spectroscopy of the carrier relaxation and recombination dynamics in epitaxial graphene," Nano Lett., **8,** 4248-4251 (2008).

[5.30] A. H. Castro Neto, F. Guinea, N. M. R. Peres *et al.*, "The electronic properties of graphene," Rev. Mod. Phys., **81,** 109-162 (2009).

[5.31] R. Saito, G. Dresselhaus, M. S. Dresselhaus, Physical properties of carbon nanotubes; Imperial College Press: London, 1998.

[5.32] V. Nathan, A. H. Guenther, and S. S. Mitra, "Review of multiphoton absorption in crystalline solids," J. Opt. Soc. Am. B: Opt. Phys., **2,** 294-316 (1985).

[5.33] J. Xia, B. Zhu, Semiconductor superlattice physics; Science and Technology Press: Shanghai, 1995.

[5.34] X. F. Wang, Y. P. Chen, and D. D. Nolte, "Strong anomalous optical dispersion of graphene: complex refractive index measured by Picometrology," Opt. Express, **16,** 22105-22112 (2008).

[5.35] D. A. Siegel, C. G. Hwang, A. V. Fedorov *et al.*, "Quasifreestanding multilayer graphene films on the carbon face of SiC," Phys. Rev. B, **81,** 241417 (2010).

[5.36] M. Orlita, C. Faugeras, J. Borysiuk *et al.*, "Magneto-optics of bilayer inclusions in multilayered epitaxial graphene on the carbon face of SiC," Phys. Rev. B, **83,** 125302 (2011).

[5.37] M. D. Dvorak, B. L. Justus, D. K. Gaskill *et al.*, "Nonlinear absorption and refraction of quantum confined InP nanocrystals grown in porous glass," Appl. Phys. Lett., **66,** 804-806 (1995).

[5.38] M. Sheik-bahaei, P. Mukherjee, and H. S. Kwok, "Two-photon and three-photon absorption coefficients of InSb," J. Opt. Soc. Am. B, **3,** 379-385 (1986).

[5.39] J. H. Bechtel, and W. L. Smith, "Two-photon absorption in semiconductors with picosecond laser pulses," Phys. Rev. B, **13,** 3515-3522 (1976).

[5.40] N. Kamaraju, S. Kumar, A. K. Sood *et al.*, "Large nonlinear absorption and refraction coefficients of carbon nanotubes estimated from femtosecond z-scan measurements," Appl. Phys. Lett., **91,** 251103 (2007).

Chapter 6 Conclusion

The unique optical properties of graphene attract enormous interest. The nonlinear optical properties of graphene have been studied intensely due to its ultrafast and large magnitude nonlinear optical response. Graphene has also been demonstrated to be an excellent saturable absorber in mode-locking to generate ultrashort laser pulses, due to its high modulation depth, low saturation intensity and ultrafast optical nonlinearity.

To gain a full understanding of saturable absorption and two-photon absorption in graphene, we employ both Z-scan and frequency-degenerate transient absorption (or pump-probe) measurements, which are described in Chapters 3. In Chapter 4, we report our systematical investigation to the saturable absorption in epitaxial graphene by carrying out Z-scan experiments on the monolayer, bilayer and 6-layer epitaxial graphene at 780 nm with 1 kHz, 400 fs laser pulses. It is found that as the number of graphene layer is increased up to 6, the nonlinear signal increases linearly, which indicates that the nonlinear signal can be enhanced by increasing the stacking of graphene layers. Furthermore, we systematically study the spectral dependence of saturable absorption of graphene by extending from 780 nm to the spectral range of 900 nm to 1100 nm with femtosecond laser pulses on epitaxial graphene. It has been demonstrated that the saturation intensity is sensitively dependent on the operating wavelength. As the operating wavelength is increased from 900 nm to 1100 nm, the saturation intensity reduces from ~5 GW/cm^2 to 1.5 GW/cm^2.

Two-photon absorption is another important nonlinear optical absorption property of graphene. It has been demonstrated that ballistic electric currents can be generated and controlled in epitaxial graphene via quantum interference between photocurrents generated by one-photon and two-photon interband transitions [6.1]. In Chapter 5, we present our observation of two-photon absorption properties of bilayer graphene. Firstly, we carry out pump-probe and Z-scan experiments on the monolayer and bilayer epitaxial graphene with femtosecond laser pulses at 780 nm. The two-photon absorption of bilayer graphene has been measured to be 10 cm/MW at 780 nm. The femtosecond Z-scans recorded at 1100 nm reveal that the two-photon absorption coefficient is 20 cm/MW.

In Chapter 5, we also introduce a two-photon absorption theory derived from quantum perturbation theory. The two-photon absorption theory discloses that the magnitude of the two-photon absorption coefficient of bilayer graphene is in agreement with our experimental measurement within one order of magnitude; and is at least 5 orders greater than that of many narrow-gap semiconductors (such as InSb, InGaAs, etc.) in the infrared region. On the other hand, the two-photon absorption of monolayer graphene is too small to be measurable consistent with our experiment. The two-photon absorption theory reveals that the two-photon absorption coefficient of monolayer graphene monotonously increases with the optical wavelength in a quadratic relation. For Bernal-stacked bilayer graphene, the two-photon absorption spectrum shows a strong resonant peak at 0.4 eV and decreases monotonously with the third order of optical wavelength on the blue side of the resonant peak in the

spectrum. The two-photon absorption coefficient of bilayer graphene at 780 nm is calculated to be 30 cm/MW, which is around 100 times bigger than the value of single layer graphene at the same wavelength. The strong resonance of the two-photon absorption of bilayer graphene, which is centered at 0.4 eV (or 3000 nm), can be attributed to the sub-band opening caused by the interlayer interaction of the Bernal-stacked bilayer graphene.

The giant two-photon absorption (2PA) should facilitate many quantum techniques, for example, the coherent control of ballistic photocurrent generated by quantum interference between one-photon absorption (1PA) and 2PA pathway in bilayer graphene. The generation of ballistic photocurrent by 1.55 μm photons through 1PA and 3.1 μm photons through 2PA is desirable because 1.55 μm wavelength is close to one of the telecom bands. Furthermore, by consideration of considerable difference in the two-photon absorption between non-Bernal-stacked and Bernal-stacked bilayer graphene, one may suggest that two-photon absorption measurements offer a practical way to determine if bilayer graphene is Bernal-stacked or not.

For future work, it is suggested that one should extend the above investigation to graphene that is doped with physical or chemical method [6.2-6.4], or reduced to limited size where quantum confinement affects the electronic band structure [6.5-6.8]. Nonlinear optical absorption of doped or quantum-confined graphene could provide more rich physics and desirable materials properties for electro-optical applications. As the Fermi level shifts due to the doping effect, the two-photon absorption of the

doped graphene could show more rich features in the spectrum, especially in the lower energy region. This could supply a way of modulating the two-photon absorption properties by doping the graphene samples. Besides, the electrical and magnetic properties of tri-layer graphene have attracted much attention due to the unique band structure attributed to the interlayer interactions [6.9-6.15]. The two-photon absorption properties of tri-layer graphene are anticipated to have more interesting features than bilayer graphene and should be a candidate in the future research.

References

[6.1] D. Sun, C. Divin, J. Rioux *et al.*, "Coherent control of ballistic photocurrents in multilayer epitaxial graphene using quantum interference," Nano Lett., **10,** 1293-1296 (2010).

[6.2] F. Wang, Y. Zhang, C. Tian *et al.*, "Gate-variable optical transitions in graphene," Science, **320,** 206-209 (2008).

[6.3] D. Waldmann, J. Jobst, F. Speck *et al.*, "Bottom-gated epitaxial graphene," Nature Mater., **10,** 357-360 (2011).

[6.4] B. D. Guo, Q. A. Liu, E. D. Chen *et al.*, "Controllable n-doping of graphene," Nano Lett., **10,** 4975-4980 (2010).

[6.5] M. Sprinkle, M. Ruan, Y. Hu et al., "Scalable templated growth of graphene nanoribbons on SiC," Nature Nanotech., 5, 727-731 (2010).

[6.6] J. M. Cai, P. Ruffieux, R. Jaafar *et al.*, "Atomically precise bottom-up fabrication of graphene nanoribbons," Nature, **466,** 470-473 (2010).

[6.7] D. V. Kosynkin, A. L. Higginbotham, A. Sinitskii *et al.*, "Longitudinal unzipping of carbon nanotubes to form graphene nanoribbons," Nature, **458,** 872-876 (2009).

[6.8] M. Y. Han, B. Özyilmaz, Y. Zhang *et al.*, "Energy Band-Gap Engineering of Graphene Nanoribbons," Phys. Rev. Lett., **98,** 206805 (2007).

[6.9] Y. Liu, S. Goolaup, C. Murapaka *et al.*, "Effect of Magnetic Field on the Electronic Transport in Trilayer Graphene," ACS Nano, **4,** 7087-7092 (2010).

[6.10] M. F. Craciun, S. Russo, M. Yamamoto *et al.*, "Trilayer graphene is a

semimetal with a gate-tunable band overlap," Nature Nanotech., **4,** 383-388 (2009).

[6.11] C. J. Shih, A. Vijayaraghavan, R. Krishnan *et al.*, "Bi- and trilayer graphene solutions," Nature Nanotech., **6,** 439-445 (2011).

[6.12] W. Bao, L. Jing, J. Velasco *et al.*, "Stacking-dependent band gap and quantum transport in trilayer graphene," Nature Phys., **7,** 948-952 (2011).

[6.13] C. H. Lui, Z. Li, K. F. Mak *et al.*, "Observation of an electrically tunable band gap in trilayer graphene," Nature Phys., **7,** 944-947 (2011).

[6.14] T. Taychatanapat, K. Watanabe, T. Taniguchi *et al.*, "Quantum Hall effect and Landau-level crossing of Dirac fermions in trilayer graphene," Nature Phys., **7,** 621-625 (2011).

[6.15] M. Freitag, "Graphene: Trilayers unravelled," Nature Phys., **7,** 596-597 (2011).